Amorphous Silicon Based Large Area Detector for Protein Crystallography

by

Afrin Sultana

A thesis
presented to the University of Waterloo
in fulfillment of the
thesis requirement for the degree of
Doctor of Philosophy
in
Electrical and Computer Engineering

Waterloo, Ontario, Canada, 2009

I hereby declare that I am the sole author of this thesis. This is a true copy of the thesis, including any required final revisions, as accepted by my examiners.

I understand that my thesis may be made electronically available to the public.

Afrin Sultana

Abstract

Proteins are commonly found molecules in biological systems: our fingernails, hair, skin, blood, muscle, and eyes are all made of protein. Many diseases simply arise because a protein is not folded properly. Therefore, knowledge of protein structure is considered a prerequisite to understanding protein function and, by extension, a cornerstone for drug design and for the development of therapeutic agents. Protein crystallography is a tool that allows structural biologists to discern protein structures to the highest degree of detail possible in three dimensions. The recording of x-ray diffraction data from the protein crystal is a central part of protein crystallography. As such, an important challenge in protein crystallography research is to design x-ray detectors to accurately determine the structures of proteins. This research presents the design and evaluation of a solid-state large area flat panel detector for protein crystallography based on an amorphous selenium (a-Se) x-ray sensitive photoconductor operating in avalanche mode integrated with an amorphous silicon (a-Si:H) charge storage and readout pixel. The advantages of the proposed detector over the existing imaging plate (IP) and charge coupled device (CCD) detectors are large area, high dynamic range coupled to single x-ray detection capability, fast readout, high spatial resolution, and inexpensive manufacturing process.

The requirement of high dynamic range is crucial for protein crystallography since both weak and strong diffraction spots need to be imaged. The main disadvantage of a-Si:H thin film transistor (TFT) array is its high electronic noise which prohibits quantum noise limited operation for the weak diffraction spots. To overcome the problem, the x-ray to charge conversion gain of a-Se is increased by using its internal avalanche multiplication gain. Since the detector can be made approximately the same size as the diffraction pattern, it eliminates the need for image demagnification. The readout time of the detector is usually within the ms range, so it is appropriate for crystallographic application. The optimal detector parameters (such as, detector size, pixel size, thickness of a-Se layer), and operating parameters (such as, electric field across the a-Se layer) are determined based on the requirements for protein crystallography. A complete model of detective quantum efficiency (DQE) of the detector is developed to predict and optimize the performance of the detector. The performance of the detector is evaluated in terms of readout time (< 1 s), dynamic range ($\sim 10^5$), and sensitivity (~ 1 x-ray photon), thus

validating the detector's efficacy for protein crystallography.

The design of an in-house a-Si:H TFT pixel array for integration with an avalanche a-Se layer is detailed. Results obtained using single pixel are promising and highlight the feasibility of a-Si:H pixels coupled with avalanche a-Se layer for protein crystallography application.

Acknowledgements

I would like to express my sincere gratitude to my supervisors, Professor K. S. Karim and Professor J. A. Rowlands, for their insightful guidance, encouragement, and support during the course of this research.

I would like to thank the members of my Ph.D. committee, Professor Ajoy Opal, Professor Donna Strickland, Professor Ian Cunningham, and Professor Jim Barby (in alphabetical order of first name) for their valuable comments that greatly helped to improve the quality of this thesis.

I also like to thank Professor Arokia Nathan for his guidance in the early days of my Ph.D. studies. I am grateful to Dr. Alla Reznik from Sunnybrook Health Sciences Center, Toronto for many valuable discussions. Many thanks go to my colleagues, Dr. Kai Wang, Matthew Wronski, Nader Safavian, and Mohammad Hadi Izadi for their helpful discussions.

I am deeply indebted to my beloved husband Jahin for his unfailing support, encouragement, and especially his patience. I am grateful to my loving daughter Simra who has brought happiness and fun in my stressful days.

Last but surely not least, I am grateful to my mother Shirin Sultana and my father Mallick Ashraf Ali, and my loving sisters for their endless love and care throughout my Ph.D. program.

Dedication

To my beloved parents.

Contents

List of Tables

List of Figures

Glossary

ADC	Analog to digital converter
AMFPI	Active matrix flat panel imager
a-Si:H	Hydrogenated amorphous silicon
a-SiN_xH	Hydrogenated amorphous silicon nitride
a-Se	Amorphous selenium
CA	Cellulose acetate
CCD	Charge coupled device
DQE	Detective quantum efficiency
EHP	Electron hole pair
FP	Flat panel
HARP	High field avalanche rushing photoconductor
IIC	Impact ionization coefficient
IP	Image plate
ITO	Indium tin oxide
LDC	Liquid crystal display
LED	Light emitting diode
MAD	Multiwavelength anomalous diffraction
MTF	Modulation transfer function
NPS	Noise power spectrum
PHD	Pulse height distribution
PKA	Probability of K_x-fluorescence absorption
PKG	Probability of K_x-fluorescence generation
PK	Probability of K_x reabsorption per K_x x-ray

PKR Probability of K_x reabsorption

PPS Passive pixel sensor

SNR Signal to noise ratio

TFT Thin film transistor

TOF Time of flight

Chapter 1

Introduction

This chapter first describes the importance of protein crystallography to medical science. Then it discusses the basic requirements of an x-ray detector for this application. The pros and cons of current x-ray detectors for protein crystallography are discussed outlining the motivation behind this research which is to design and evaluate a novel large area active matrix flat panel x-ray detector that can meet the requirements for this application.

In medicine, most drugs have been discovered either by identifying the active ingredient in traditional remedies or by serendipitous discovery. Recently, a new drug design approach called, "rational drug design" has been introduced that commences a new branch in medical science known as "molecular medicine" [1]. Rational drug design is based on the understanding of how diseases can be controlled at the molecular level within proteins and other biological macromolecules. In this approach, the drug targets specific entities based on the knowledge of three-dimensional (3D) molecular structures of the protein, or other biologically active molecules. So today's scientists are interested in understanding the role of proteins in diseases and developing novel compounds to modify the functions of disease-causing proteins. The function of a protein is encoded by its 3D structure. Protein crystallography is used as the major biophysical approach to investigate protein structure and function. A world class protein crystallography facility together with a high throughput protein expression facility for protein structure determination can be used to examine proteins of prime importance to human health. The recent advances

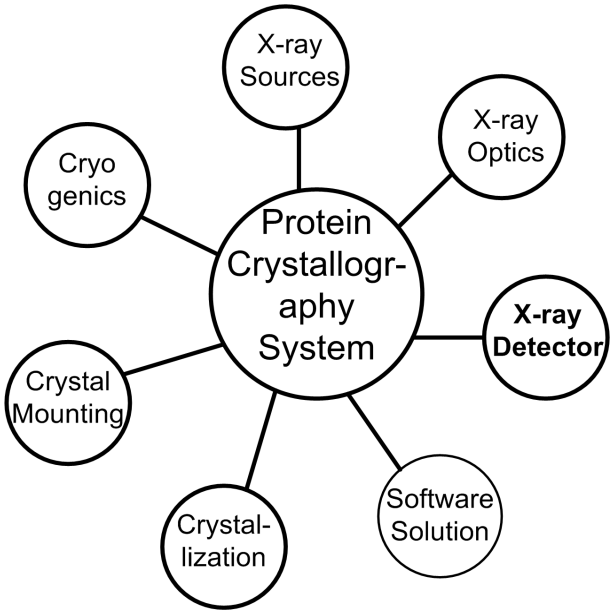

Figure 1.1: Critical components of a protein crystallography system.

in molecular medicine have led to an increase in the demand for structural information about proteins and, at the same time, an increase in the throughput of protein structure determination [2].

1.1 Protein Crystallography

In order to visualize structures at the atomic scale it is necessary to work with electromagnetic radiation with wavelengths of the order of atomic bond distances (approximately 1 $\mathring{A}$) [1]. X-rays have such suitable wavelengths and as such x-ray diffraction is used to determine atomic structures. However, there are no lenses available to bend and focus the scattered x-rays. Instead atomic structures are reconstructed using diffraction theory from the intensities of the diffracted waves which can be measured experimentally.

Protein crystallography resolves the atomic arrangement of protein by measuring the intensity of its x-ray diffraction pattern [3]. The critical constituents of a protein crystallography system include: setup for protein crystallization, robotics for crystal mounting, x-ray generators, x-ray optics, cryo-cooling systems, x-ray detectors, diffraction data acquisition system, and structure solution software (see Figure 1.1).

In a typical crystallography experiment, the protein crystal is put inside a thin-walled

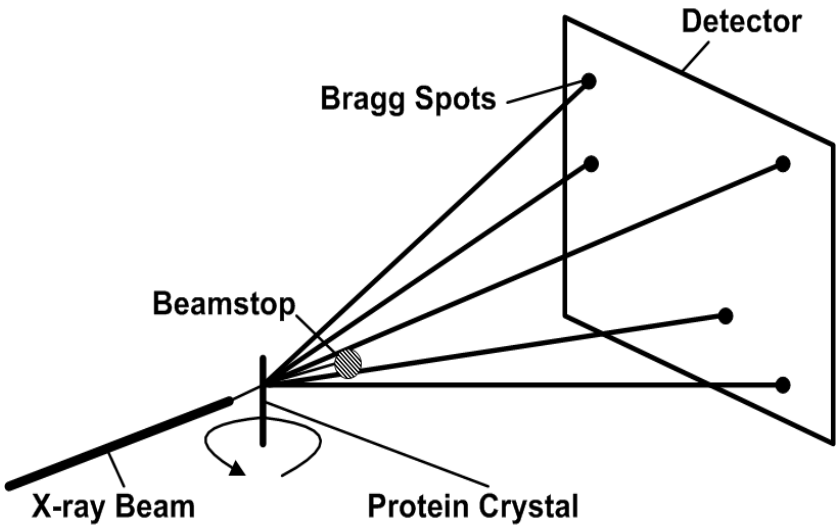

Figure 1.2: Setup for a typical protein crystallography experiment.

capillary. A monochromatic x-ray beam of 6 to 20 keV (i.e. wavelength, $\lambda = 2.1$ to 0.6 $\mathring{A}$ which is comparable to the protein crystal's inter-atomic distances) is incident on the protein sample, diffracted by the atoms of protein crystal, and the diffraction patterns are recorded by a two dimensional x-ray sensitive area detector, as shown in Figure 1.2. The direction of the diffracted x-ray beam is defined by the crystal lattice, and the intensity of the diffracted beam is determined by the atomic arrangement within the unit cell of the crystal. The intensity of the diffracted beam is maximized when it satisfies Bragg's law. The protein crystal is rotated around an axis perpendicular to the x-ray beam so that every atomic plane can be exposed to x-rays. In order to solve the 3D structure of protein, several hundred diffraction patterns are recorded where each pattern contains several thousand diffraction maxima, commonly known as Bragg peaks [4].

The x-ray area detector captures two dimensional diffraction images where each image contains a number of lines each containing some number of picture elements (pixels). At each pixel the relative brightness is measured and recorded. Figure 1.3 shows a representation of a single Bragg peak. If the detector is connected to a computer, this information can be immediately processed and analyzed.

The primary interest for protein crystallography experiment is the accurate measurement of the position and intensity of the Bragg peaks. As such, the most important challenge in protein crystallography research is to design appropriate detectors to accu-

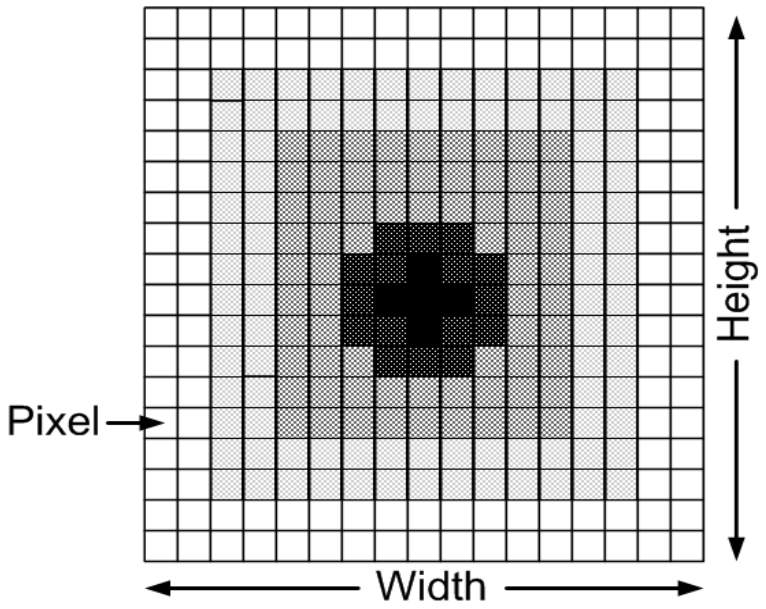

Figure 1.3: Image of a diffraction pattern containing a Bragg peak.

rately capture the diffraction pattern.

1.2 Requirements of a Protein Crystallography Detector

The design of the detector is dictated by several key requirements for protein crystallography. Its critical design parameters are imaging area, dynamic range, readout time, sensitivity, and spatial resolution [4], [5].

1.2.1 Area of the Detector

The imaging area of an ideal detector is the area required to collect all of the diffraction data to a specified resolution [5]. However, generally the first 100 orders of diffraction data contain useful information about the structure of protein crystal, and therefore collecting those data with a large area (say, 20 cm $\times$ 20 cm) detector is sufficient to determine protein structure [6]. The same field of view can be achieved by placing a smaller detector closer to the crystal. The drawback of the latter approach is that it accumulates more background x-ray scattering noise. Background x-ray scattering noise is generated by the x-rays scattered by the noncrystalline portion of the protein crystal.

The background noise can be minimized by having a large crystal-to-detector distances since x-rays in Bragg peaks emerge collimated from the crystal, while the background scatter drops with the square of the crystal-to-detector distance [6].

1.2.2 Dynamic Range

The probability density of x-ray diffraction spot intensity of protein crystal follows a Gaussian function [7]. Hence most of the diffraction spots are weak ($\sim$ ten x-ray photons per pixel) and very few diffraction spots are strong ($\sim \ 1.2 \times 10^5$ x-ray photons per pixel). Strong diffraction spots or Bragg peaks contain the majority of the information regarding the molecular structure of the crystal, and the detector should have adequate charge storage capacity to accurately measure the peak spots without pixel saturation [6]. On the other hand, if the electronic noise level of the detector is high, the weak diffraction spots may not be able to overcome the noise, and hence can not be detected. So high dynamic range detector is crucial for protein crystallography applications since both weak and strong Bragg peaks need to be imaged.

1.2.3 Sensitivity

Protein crystals diffract x-rays weakly, typically less than 0.1% of the incident x-ray beam scatters from the crystal. So the intensity of diffracted x-ray is low, and it takes long time to build a detectable signal, resulting in time consuming experiments [8]. On the other hand, protein crystals degrade when exposed to x-rays that leads to gradual degradation of the resolution of the diffraction pattern [9]. Radiation damage is sometimes so serious that after only a few hours of exposure at room temperature, the x-ray diffraction pattern dies away [10]. X-ray photons cause the formation of radicals, which leads to subsequent chemical reactions that gradually destroy the crystalline order. Reducing the radiation dose absorbed by the protein is an effective way to mitigate protein damage. Therefore, a sensitive detector is required that can efficiently and quickly detect small diffraction signal generated from low dose x-ray. Ideally, the detector should be sensitive enough to detect each absorbed x-ray photon.

1.2.4 Image Charge Integration and Readout Time

The image charge integration time requirement of the detector largely depends on the type of x-ray source used for the experiment. The x-ray sources used are of two general kinds: rotating anode and synchrotron sources. Rotating anode sources are usually operated at 8 keV, and used in home laboratories. Synchrotron sources are usually operated at 12 keV, and shared by many research groups in national laboratories.

For a rotating anode x-ray source, x-rays are less intense and the signal on the detector builds up slowly. So, the integration time of the detector should be long enough (one or two minutes) to permit the detector to record all the data [11]. In contrast, synchrotron sources deliver x-ray beams that are not only much more intense, but also more directionally homogeneous. So a large number of x-rays diffract from the crystal in a short time interval, so the integration time of the detector can be shorter (one or two seconds) [11], [12].

Readout time is the time required by the detector to pass the charge integrated on the detector to the external circuitry. For both sources, the readout time of the detector should be in the range of seconds to minimize the total x-ray exposure time as well as radiation damage to protein.

1.2.5 Spatial Resolution

For accurate analysis of the intensity distribution of diffraction spots, the pixel size of the detector should be such that a few pixels (3 to 5) can hold each Bragg peak. On the other hand, to clearly resolve two adjacent diffraction spots, there should be about five pixels between them [5], [6].

For example, if 12 keV x-rays (wavelength about 1 $\mathring{A}$) are used to illuminate a protein crystal with unit cell dimension of 20 nm and the crystal-to-detector distance is set to 20 cm, the typical size of a Bragg peak would be 100-300 μm, calling for pixel sizes in the order of 50-150 μm [4].

Table 1.1 lists the considerations to design a detector for protein structure determination [4], [5].

Table 1.1: Design considerations for a protein crystallography x-ray detector

Parameter	Values
Detector area	Larger than 20 cm $\times$ 20 cm
Dynamic range	Greater than 10^4
Readout time	$\sim$ 1 s
Pixel size	50-150 μm
X-ray wavelength	1.54 $\mathring{A}$ (rotating anode) or 1 $\mathring{A}$ (synchrotron)
X-ray Energy	8 keV (rotating anode) or 12 keV (synchrotron)
Object size	1.8 $\mathring{A}$ (Inter-atomic distance of protein)

1.3 State of the Art X-ray Detectors

Rapid and accurate data collection of protein crystallographic experiments has become a priority for proper understanding of protein structure. To meet that need, two competitive technologies have emerged: image plate (IP) based large area x-ray detectors and charge coupled device (CCD) based x-ray detectors [13], [14].

1.3.1 Image Plate X-ray Detector

Image plates (IP) are photon integrating x-ray detectors comprised of specifically designed photo-stimulated phosphors that trap and store x-ray energy. Energy from incident x-ray photons is stored and stable on the plate until it is readout by scanning with a red laser beam. As a result of the red light illumination during scanning, a blue light is emitted from the plate which is measured by a photomultiplier. The quantity of the blue light is proportional to the number of x-ray photons to which that particular position of the plate has been exposed. The readout of the plate uses up most of the stored image, and any remaining image is erased by a bright white light [11].

The advantages of IPs includes high spatial resolution, large imaging area (30 cm $\times$ 30 cm), high dynamic range (nearly six orders of magnitude), and very low background noise. The main disadvantage of IP is slow readout. The readout of IP is sequential

and thus the time to read each plate becomes proportional to its area. As a result, the detector area and readout time must be traded off against the other. Generally, a few minutes are required to readout the image from IP and the plate has to be mechanically exchanged from one exposure to another for the readout. Recent advancement in IP technology introduces multi-plate IP system that offers simultaneous expose, erase and readout operation, thus minimizing "dead time" between exposures [14].

1.3.2 Charge Coupled Device (CCD) Based X-ray Detector

Charge coupled device (CCD) based x-ray detectors are also photon integrating detectors with readout time in the range of ms. CCDs use a phosphor screen to convert incident x-rays into visible light photons, where the number of light photons produced is proportional to the incident x-ray intensity at that point. Light from the phosphor travels through the taper and is imaged onto a CCD sensor thermally stabilized by thermoelectric cooler. A schematic diagram of a CCD based x-ray detector is shown in Figure 1.4.

CCD sensors have small area (5 mm $\times$ 5 mm) and they have to be coupled to demagnifying fiber optic tapers to image a large area. Fiber optic tapers transmit only a small fraction of the input signal from the phosphor screen to the CCD since its light collection efficiency is only $\frac{1}{(1+m^2)}$ where m is the demagnification ratio, and degrades the overall sensitivity of the detector system [11], [15]. An alternative way to increase the size of the imaging area is to manufacture many modules and place them together in an array. Since a large area is necessary for protein crystallography, most commercial CCD detectors are modular, with either 2 $\times$ 2 or 3 $\times$ 3 tiling of square modules. CCDs need to be cooled to assure low noise operation [4]. The cooling system along with fiber optic taper makes CCD detectors complicated and expensive [16].

1.3.3 Active Matrix Flat Panel X-ray Detector

Active matrix flat panel imagers (AMFPIs) based on amorphous silicon (a-Si:H) thin film transistor (TFT) arrays is an well established technology for liquid crystal displays (LCDs), and is the most promising technology for large area digital x-ray imaging due to its compact size, rapid readout, and superior performance compared to screen films

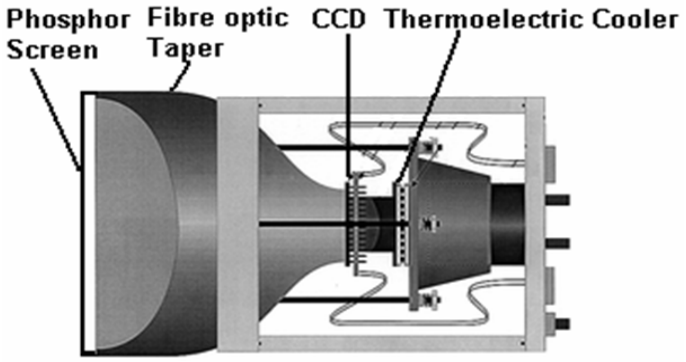

Figure 1.4: Schematic diagram of CCD based x-ray detector.

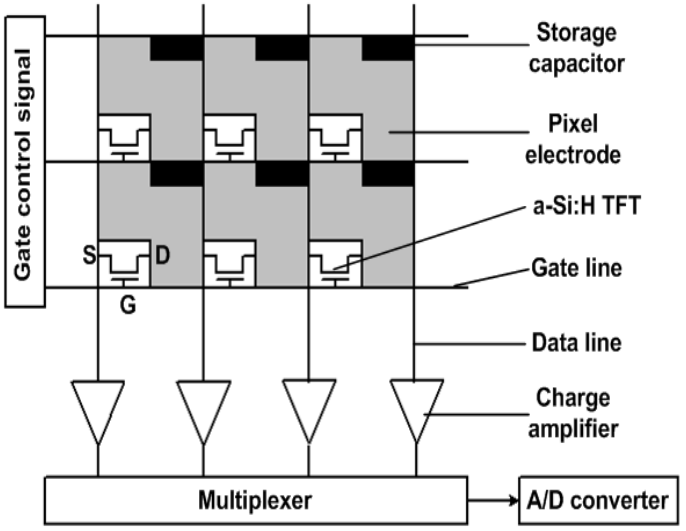

Figure 1.5: Schematic diagram of the active matrix readout array.

[17], [18], [19], [20]. Recently, the application of AMFPIs has been proposed in the field of protein crystallography [6], [21], [22].

AMFPIs contain a two-dimensional array of pixels where each pixel contains a pixel electrode to collect the x-ray generated charge, a storage capacitor for holding the charge before the readout, and an a-Si:H TFT for the charge readout (See Figure 1.5). For each TFT, the gate (G) is connected to gate signal generator, the drain (D) is connected to the storage capacitor through the pixel electrode, and the source (S) is connected to the data line. The TFTs are turned OFF during the charge integration period permitting the storage of charge on the pixel capacitor. During readout, the TFTs are turned ON and transfer the charge from the storage capacitor to the data line. To provide a parallel

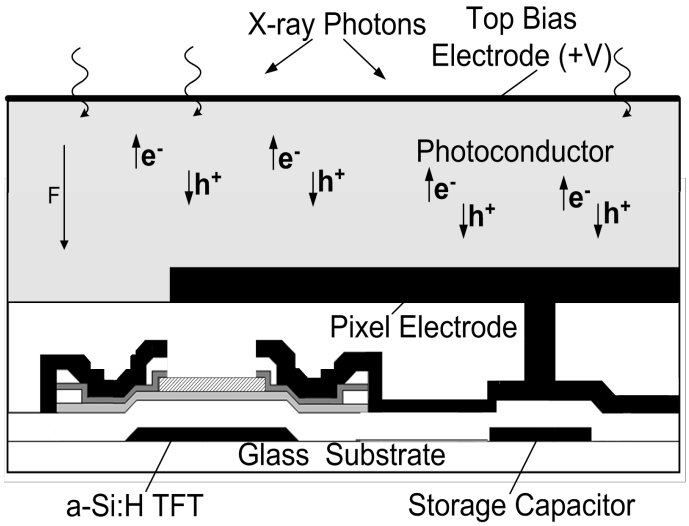

Figure 1.6: Direct x-ray detection method.

readout, the TFTs in the same column share a common data line, whereas the TFTs in the same row share a common gate line. The data lines are connected to the external charge amplifiers to amplify the signal that is then transferred to analog-to-digital converter (ADC) by a parallel-to-serial multiplexer.

Based on the x-ray detection method, AMFPIs are divided into two categories: direct detection and indirect detection [17]. Figure 1.6 illustrates the direct detection scheme where a uniform x-ray sensitive photoconductor layer (such as amorphous Selenium) is deposited on top of a-Si:H TFT arrays. Incident x-rays are absorbed in a-Se, and directly converted to electrical charges, which are then collected by an electric field that is applied across the photoconductor layer. The collected charges are stored in the storage capacitor and readout by the arrays of a-Si:H TFTs.

In the indirect detection scheme, a phosphor layer (such as structured cesium iodide, CsI) is used to convert incident x-rays into optical photons. The visible light emitted from the phosphor layer is absorbed and converted to charge by either a photodetector layer (such as a-Se) over the TFT array or a photodiode (such a-Si:H p-i-n diode) integrated at each pixel of the TFT array (see Figure 1.7).

The direct x-ray detection method is advantageous since it has higher resolution, simpler TFT array structure, and it can be manufactured in standard facility for LCD systems.

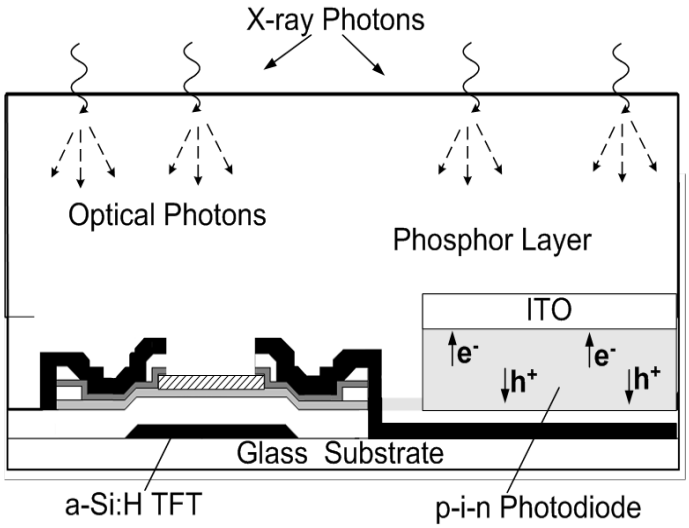

Figure 1.7: Indirect x-ray detection method.

1.3.4 Comparison of the Performance of Current Detectors

Table 1.2 shows a comparison of some protein crystallography detectors available to date in the market place [13], [14]:

The drawbacks of CCD detectors are small area, low dynamic range, complex cooling system and high cost. The disadvantage of IP is slow readout. The flat panel detectors available in the market use regular a-Se layer to directly convert x-ray photons into electrons, but they cannot detect single x-ray photon. So there is a need for a detector that would cover a large area, discriminate individual x-ray photons, be operationally stable over the entire x-ray range and last, but not least, be cost-effective compared to other present detectors in this area.

1.4 Research Motivation

The need for an improved detector for protein crystallography motivated our research on a new detector concept using a-Si:H AMFPIs as the charge readout system and high gain avalanche a-Se photoconductor as the charge conversion system. We proposed to use a-Si:H AMFPI for protein crystallography due to its large area x-ray imaging capability, improved image quality, and computerized data handling/storage ability. a-Si:H flat panel detectors, which are not limited by size, can add two significant advantages: more of the

Table 1.2: Performance comparison of current protein crystallography detectors.

Parameter	MAR 555	Rigaku Saturn A200	Rayonix MX 325 Mosaic	MAR 345	Rigaku R-AXIS HTC
Detector type	Flat Panel Detector	CCD	CCD	Image Plate	IP 3 plate system
Active area (mm)	430 × 350	203 ×203 Demagnification 4:1	325 ×325 Demagnification 4:1	345 diameter	300 × 300
Pixel size (μm)	140	CCD 24	CCD 40	150 or 100	200, 100 or 50
Sensitivity	1 x-ray photon per ADC-unit at 8 keV	1 x-ray photon	DQE up to 0.8	1 X-ray photon per ADC-unit at 8 keV	1 X-ray photon per ADC-unit at 8 keV
Dynamic range	18 bit	7100:1	16 bit	128000:1	500000:1
Readout time (s)	2	2.5	1	150 × 150: 68, 100 × 100: 96	20

diffraction pattern can be imaged, and the crystal-to-detector distance can be increased resulting in low background x-ray scattering noise. Moreover, since the detector can be made approximately the same size as the diffraction pattern, it eliminates the need for image demagnification. The readout time of AMFPIs is usually in the range of 33 ms to 1 s, so it is appropriate for crystallographic application. Direct x-ray detection scheme is chosen for the proposed detector to have better spatial resolution and higher sensitivity. Moreover, a-Se has high x-ray absorption coefficient for the functional x-ray energy range of protein crystallography.

The main disadvantage of a-Si:H AMFPI is its high electronic noise which is reported to be on the order of 1000-3000 electrons per pixel [23], [24]. In protein crystallography experiment, the number of incident x-ray per pixel is very few for weak diffraction spots, and the electronic noise of a-Si:H array may exceed the quantum noise of the detector

for weak spots. In this work, to make the detector quantum noise limited even for the weak diffraction spots, we proposed a strategy to increase the photoconductor x-ray to charge conversion gain by using its internal avalanche multiplication gain. We intended to use avalanche a-Se as the photoconductor since it exhibits strong and stable avalanche multiplication gain (up to 1000) at practical electric fields [25]. Although avalanche a-Se technology is mature for optical imaging and has been used commercially in high definition television, and referred to as HARP (high field avalanche rushing photoconductor) [26], its application in x-ray imaging is novel.

1.5 Thesis Organization

Chapter 2 describes the proposed a-Si:H based detector and analyzes its feasibility for protein crystallography. Chapter 3 describes the effect of K-fluorescence reabsorption of a-Se on the performance of the proposed detector. Chapter 4 describes the integration technique of HARP with thin film technology and presents experimental results of single pixel operation as a proof of concept. Chapter 5 presents experimental results of the metastability of a-Si:H TFT under bipolar pulse bias stress. This chapter also presents a linear system model of the detector in order to characterize its performance in terms of detective quantum efficiency (DQE). Finally, Chapter 6 summarizes the contributions of this research and draws the conclusion.

Chapter 2

Feasibility Analysis of an a-Si:H Based Active Matrix Imager for Protein Crystallography

In this chapter, we describe the concept of a large area active matrix flat panel imager for protein crystallography, and establish a systematic approach to find the optimal design and operating parameters of the detector. The detector utilizes avalanche a-Se as the x-ray conversion layer and a-Si:H flat panel as the readout system. The performance of the detector is evaluated in terms of readout time (<1 s), dynamic range ($\sim 10^5$), and sensitivity ($\sim$ 1 x-ray photon), thus validating the detector's efficacy for protein crystallography.

Active matrix flat panel imagers (AMFPI) have been widely used for diagnostic medical imaging such as radiography, fluoroscopy, and tomography because of their large area readout capability. We proposed to use a-Si:H based AMFPIs for protein crystallography using a-Se as the photoconductor. X-rays diffracted from a protein crystal are incident on a uniform layer of photoconductor, and the photoconductor directly converts x-rays into electron-hole pairs (ehps). The generated ehps are first stored in the pixel storage capacitor and then electronically read by a two-dimensional array.

2.1 Design Approach

The requirements for a protein crystallography detector have been discussed in chapter 1. Based on these requirements, we selected appropriate photoconductor material and readout technology for the detector that not only meets the design requirements, but also has many favorable attributes.

2.1.1 Selection of Photoconductor

The performance of any direct conversion x-ray detector depend largely on the selection and design of the photoconductor. In order to have good image quality the photoconductor must have several important properties:

i) The photoconductor should have high x-ray absorption efficiency so that most of the incident x-rays should be absorbed within a practical photoconductor thickness.

ii) It should have high x-ray to charge conversion efficiency. This means the amount of x-ray energy required to create a single ehp must be as low as possible.

iii) It should have low dark current to minimize dark current noise of the detector. Low dark current implies that the photoconductor should have a wide band gap ($\sim$ 2 eV) to limit the thermal generation of charge carriers in the bulk [27].

iv) The photoconductor should have good bulk charge transport properties to allow the generated charge to reach the pixel electrodes before the charges are lost in traps.

v) It should have poor surface conductivity to prevent the lateral conduction of the image charge once it has reached the pixels to avoid cross-talk.

vi) It should be stable under the conditions of use, and over the lifetime of the detector system.

vii) It should be able to be uniformly deposited over a large area ($\sim$ 30 $\times$ 30 cm^2 or larger) using a deposition technology and temperature that is compatible with the readout technology.

It is difficult to grow crystalline photoconductors over a large area. So they cannot be used for large area imaging [28]. Therefore, only amorphous or polycrystalline photoconductors are suitable for use in large area x-ray detectors. Polycrystalline lead iodide (poly-PbI_2), polycrystalline lead oxide (poly-PbO_2), polycrystalline mercury iodide (poly-HgI_2), polycrystalline cadmium zinc telluride (poly-CZT), amorphous selenium (a-Se), and amorphous silicon (a-Si:H) are good candidates for the application. Although, polycrystalline materials have high x-ray to charge conversion efficiency, their charge transport is limited by the grain boundaries. Another disadvantage of polycrystalline photoconductor is its higher dark current compared to amorphous photoconductor.

Between two amorphous semiconductors, a-Se has the greater potential because it has a much higher x-ray absorption coefficient than a-Si:H due to its larger atomic number. However, pure a-Se is thermally unstable and crystallized over time. Alloying pure a-Se with As (0.2-0.5%) and doped with Cl (10-40 ppm Cl) greatly improves the stability of the composite film and helps to prevent crystallization [29]. Stabilized a-Se can be deposited over a large area as thick films (100-500 μm) on suitable substrate by conventional vacuum deposition technique at substrate temperature below 70 °C. The low substrate temperature does not cause any damage to the readout electronics on the substrate. Furthermore, the dark current in a-Se is low (0.3 pA/mm^2) because of its larger band gap ($E_g \approx 2.2$ eV) and small concentration of deep localized states in the mobility gap [28], [30]. Due to all these attributes, a-Se has been successfully employed in medical imaging systems, and we selected it as the photoconductor for protein crystallography application.

2.1.2 Avalanche Amorphous Selenium

One key requirement for protein crystallography is that the detector must be able to detect each incident x-ray photon. A scientist named Albert Rose working on early television systems showed that to reliably identify an object, the SNR needed to be greater than 5 [31], [32]. This requirement is known as *Rose's criterion*. So the signal per pixel from one x-ray photon should be at least 5 times greater than the noise per pixel of the detector. Since the x-ray energy range for protein crystallography is low, to make the detector sensitive to each incident photon, an increase in x-ray sensitivity of a-Se is required. The amount of energy required to create a single ehp is expressed as $W_{\pm}$. The dependence of

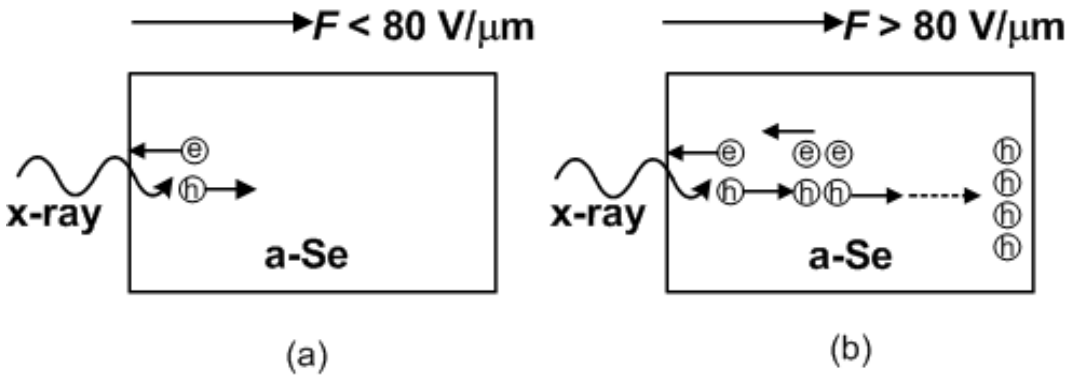

Figure 2.1: (a) a-Se layer under non-avalanche field and (b) a-Se layer under avalanche field where more ehps are produced by impact ionization.

$W_{\pm}$ on electric field, F, is expressed as:

$$W_{\pm} = W_{\pm}^{\circ} + \frac{B}{F} \tag{2.1}$$

for $W_{\pm}^{\circ} = 6$ eV, $B = 4.4 \times 10^6$ eV V/cm, and $F = 10$ V/μm, $W_{\pm}$ becomes 50 eV [33]. So 20 ehps can be generated from a 1 keV x-ray photon. The x-ray to charge conversion gain, g, is expressed as 20 ehp/keV. The x-ray sensitivity or ehp generation efficiency of a-Se can be increased by applying higher electric field (F>80 V/μm) to cause avalanche multiplication of generated ehps, and this approach is adopted in our detector [25].

When an x-ray photon is fully absorbed in a biased a-Se layer, a large quantity of ehp are generated. This initial process of charge generation is followed by a process called geminate recombination, that is, charge carriers of the opposite sign recombine, and no longer contribute to the signal. The number of ehp that survive recombination depends on the applied electric field. Increasing the electric field helps to reduce recombination, and the charges drifts towards the pixel electrodes. For electric fields below the avalanche multiplication threshold (F<80 V/μm), the charge collected is equal to the number of ehp created by x-ray photon, resulting in a gain of unity. Above the avalanche multiplication threshold (F>80 V/μm), the drifting holes gain enough kinetic energy to create additional ehps along their paths by impact ionization (see Figure 2.1). This results in an exponential increase in the number of ehps with traversed distance, that is, in avalanche multiplication [34], [35].

Avalanche multiplication in a-Se was first reported by Juska and Arlauskas [34]. They carried out time of flight (TOF) transient photoconductivity experiments on a series of a-Se films of different thickness at very high fields (F >50 V/μm) and observed clear avalanche multiplication of photogenerated carriers. In contrast to crystalline semiconductors, the temperature dependence of the impact ionization rates in a-Se is positive. Avalanche phenomenon in a-Se has some advantages [26]:

i) In a-Se the impact ionization rate of the hole is much larger than that of the electron due to larger hole drift mobility (roughly a factor of $\sim$ 30 larger than the electron drift mobility). This mitigates the avalanche multiplication noise.

ii) The electric field in the a-Se layer is almost uniform over the thickness, and avalanche multiplication occurs throughout the a-Se layer. This simplifies the structure and fabrication process of a-Se avalanche devices.

iii) It is found in literature that avalanche multiplication occurs uniformly over an area of 5 cm^2 and it is expected to have multiplication uniformity over a large area ($\sim$ 20 cm^2) which is essential for digital x-ray imaging systems [26].

Avalanche multiplication factor or avalanche gain (g_{av}) is determined by the thickness of the a-Se layer and impact ionization rates. The multiplication factor is calculated using the following expression [36]:

$$g_{av} = \frac{(\gamma_p - \gamma_e)\exp\{(\gamma_p - \gamma_e)d_{Se}\}}{\gamma_p - \gamma_e \exp\{(\gamma_p - \gamma_e)d_{Se}\}} \tag{2.2}$$

where d_{Se} is the thickness of the a-Se layer and γ_e and γ_p are electron and hole impact ionization coefficient (IIC), respectively. In a-Se the value of γ_p is much greater than γ_e since the drift mobility of holes (0.18 cm^2/Vs) is much higher than that of electrons (0.003 cm^2/Vs). Under the assumption that the contribution of electrons to avalanche gain is negligible, (2.2) can be simplified to:

$$g_{av} = \exp(\gamma_p d_{Se}) \tag{2.3}$$

The field dependence of the hole IIC is given by [36]:

$$\gamma_p(F) = \gamma_{p_1} \exp(-\frac{\gamma_{p_2}}{F}). \tag{2.4}$$

According to (2.3) and (2.4), a larger avalanche gain can be obtained either by using a thicker a-Se layer or by increasing electric field.

Avalanche multiplication is caused by carrier ionization events which occur with statistically distributed probability. Since avalanche multiplication is a random process, it is intrinsically noisy. Therefore, g_{av} fluctuates from the mean value, resulting in generation of gain fluctuation noise on the signal. Previous investigations on optical sensors with avalanche multiplication have shown that increasing g_{av} increases noise and degrades the SNR of the system [37]. However, x-ray photons carry more energy than optical photons, and consequently an x-ray photon is converted into many ehps while an optical photon is converted into only a single ehp. So each x-ray photon can be represented by thousands of ehps and each independently undergoes avalanche multiplication, rather than just one for the optical case [38]. If the x-ray to ehp conversion gain is greater than 10, the gain fluctuation noise of avalanche gain can be neglected for a direct detection system [39]. For an indirect detection scheme, if the product of the phosphor layer conversion gain, the coupling efficiency, and the optical efficiency of the a-Se layer is greater than 10, avalanche gain fluctuation noise can be neglected.

The avalanche gain of x-ray generated ehps is dependent on the location where the x-ray was absorbed [39]. If an x-ray is absorbed at the top of the a-Se layer, the holes generated by this x-ray will traverse the entire thickness of the a-Se layer and experience the largest avalanche gain. The holes generated by other x-rays absorbed deeper in the detector will traverse a shorter distance, and hence their gain will be much less. It results in depth dependent gain fluctuation noise.

The variance associated with the avalanche gain can be determined from the pulse height distribution (PHD) of avalanche gain. The pulse height distribution is the number of events detected as a function of avalanche gain for absorption of a single x-ray in a-Se. The noise associated with avalanche gain can be expressed by avalanche gain swank factor, A_M, which is defined in terms of the moments of PHD and is given by [39]:

$$A_M = \frac{\alpha(\alpha + 2\gamma_p)(\exp(\gamma_p d_{Se}) - \exp(-\alpha d_{Se}))^2}{(\alpha + \gamma_p)^2 \eta(\exp(2\gamma_p d_{Se}) - \exp(-\alpha d_{Se}))}. \tag{2.5}$$

where α is the linear attenuation coefficient, η is the quantum efficiency, and other parameters are already defined in (2.2). One way to eliminate depth dependent gain fluctuation

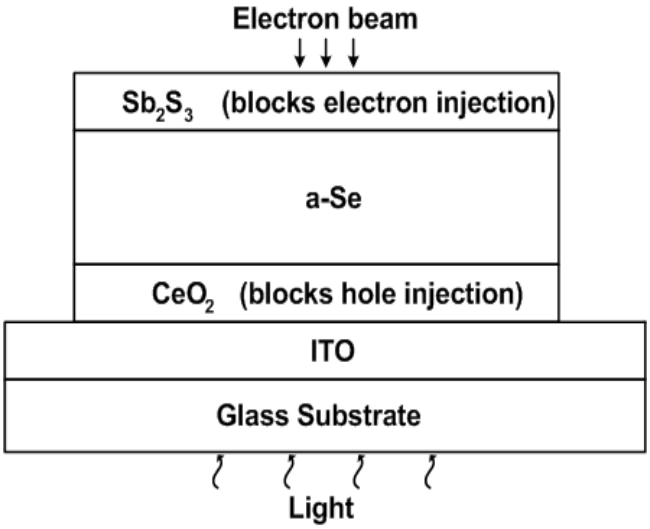

Figure 2.2: a-Se layer used in HARP camera.

noise is to use lower energy x-rays because the linear attenuation coefficient is large at low energy. So the depth of x-ray absorption will be shallow reducing the fluctuation in the depth of absorption. The x-ray energy range for protein crystallography is low, so the x rays will be absorbed at the top. This is advantageous because the path length of all holes will be identical giving rise to a stable avalanche gain and minimizing the depth dependence.

The first practical avalanche a-Se for optical application known as HARP utilizes a blocking structure, where the a-Se layer is confined between two specially designed blocking contacts (CeO_2 and Sb_2S_3) which prevent charge injection from contacts while providing for the exit of generated and multiplied carriers to the external circuit [35], [26]. Figure 2.2 shows the simplified diagram of avalanche a-Se which utilizes HARP layer. Due to the higher hole mobility, light has to enter from the positive bias electrode to maximize avalanche gain. HARP contains a transparent indium tin oxide (ITO) electrode which is biased positively during imaging. A layer of a-Se is sandwiched between a thin layer ($\sim$ 20 nm) of CeO_2 on the front side and a submicron thin layer of Sb_2S_3 on the back. The CeO_2 blocks injection of holes from the positively biased ITO, and the Sb_2S_3 prevents electron injection, and dark current is kept at a low value of < 0.1 nA/mm^2. The thickness of intrinsic a-Se layer is from 0.5 to 35 μm depending on the desired avalanche gain. Currently a-Se HARP layers are employed in electron-beam scanned Harpicon TV

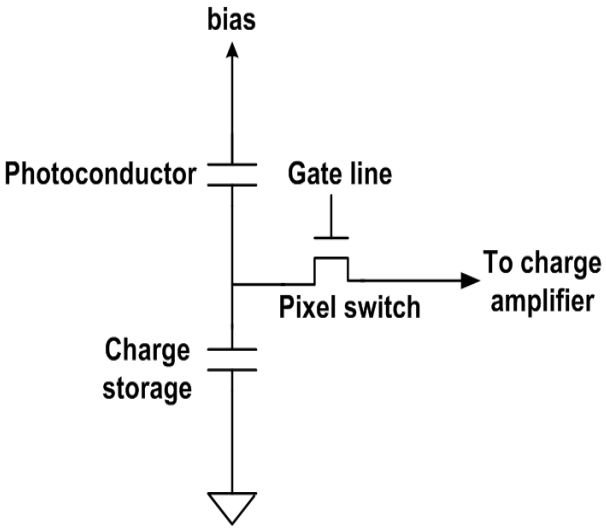

Figure 2.3: The general design of a pixel.

camera tubes. Avalanche a-Se with blocking structure is a potential candidate for low energy x-ray applications, and as such we decided to use them as the photoconductor for our detector.

2.1.3 Choice of Readout Technology

Under the photoconductor layer, the protein crystallography detector requires a large area two dimensional charge storage and readout pixel array (as shown in Figure 1.5 of Chapter 1). The general architecture of the pixel is shown in Figure 2.3. After exposure, a pixel storage capacitor holds the charge until readout, and a pixel switch controls the readout. The simplest concept is to use a thin film transistor (TFT) as a switch to transfer the charge. The required performance of the TFT are summarized as in Table 2.1 [15], [40].

Hydrogenated amorphous silicon (a-Si:H) technology satisfies the requirements of large area, low dark current along with low temperature deposition (< 300 °C), standard integrated circuit lithography processes, high spatial uniformity, low capital equipment cost and such has become a widely used material in large area applications. It took decades of research to get device-quality amorphous silicon since its inception. A direct result of this has been the a-Si field effect transistor commonly known as a thin film transistor (TFT), which will be used as a switch for our detector.

Table 2.1: Performance requirements of a TFT of the readout array.

Parameter	Values
OFF resistance	$> 10^{14}$ Ω
Leakage current	$\sim$ 10 fA
ON resistance	$< 10^{6}$ Ω
Noise (thermal and flicker)	$<$ 1000 electrons

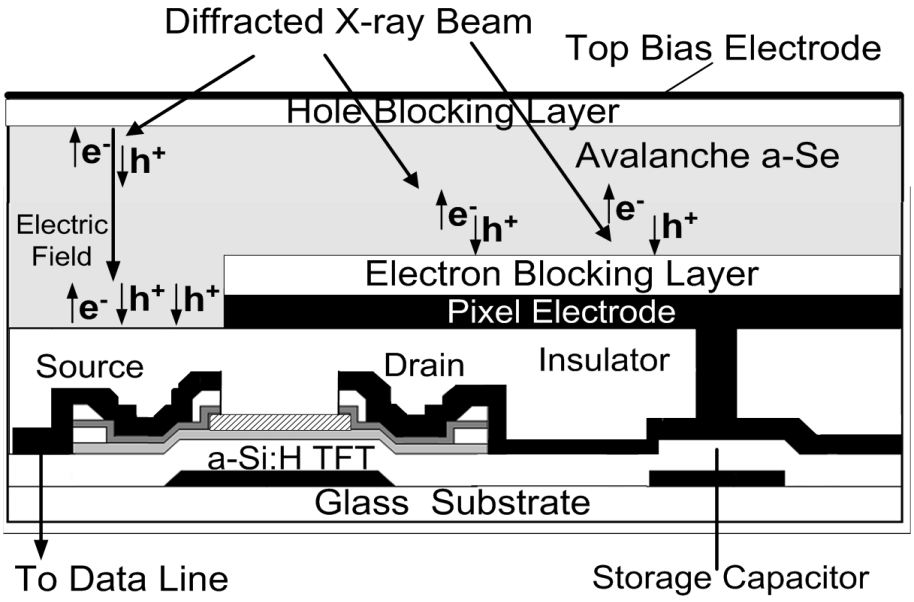

Figure 2.4: Cross section of a single pixel of the detector using direct detection scheme.

a-Si:H TFTs have several useful features, including high off resistance ($\sim 10^{12}$ Ω), low on resistance ($\sim 10^{6}$ Ω), low leakage current ($\sim$ 0.1 pA), and linear switching characteristics. A major drawback of a-Si:H TFT is the metastable shift in its threshold voltage over time. Creation of defect states in the a-Si:H band gap under prolonged gate bias (carrier accumulation) and charge trapping in the gate nitride are responsible for such behavior [41], [42]. Metastability complicates the application of a-Si:H TFTs as analog devices.

2.2 System Design of the Detector

X-ray are incident on the detector, absorbed in a-Se layer and converted into ehps. Figure 2.4 shows the schematic cross-section of a single pixel of the detector. Each pixel consists of a pixel electrode to collect the charge generated by a-Se, a storage capacitor for holding the charge before the readout, and an a-Si:H TFT for the charge readout. The top electrode is common to all the pixels, and is biased to a high positive potential to establish an electric field across the a-Se photoconductor layer. The electrons drift to the top electrode and become neutralized whereas the holes drift to the bottom surface of the a-Se layer and are collected by the pixel electrode preserving the position information of charge generation. The application of an electric field in excess of the avalanche multiplication threshold ($\sim$ 80 V/μm) initiates hole impact ionization and generates secondary ehps resulting in internal multiplication gain [24]. The structure of the avalanche a-Se layer is designed based on HARP structure discussed in Section 2.1.2 and it can withstand the high electric field required for avalanche without breakdown, and with little charge injection from both top and pixel electrodes. As a result, the dark current of avalanche a-Se does not exceed 0.1 nA/mm^2 even at the highest electric field needed for an avalanche gain of 1000. The lower the gain, the lower is the dark current. For example, at the electric field required for the gain of 10 the dark current is $<$ 0.004 nA/mm^2, thus warranting low noise and high dynamic range [25], [43].

An alternative approach is to use avalanche gain with indirect detection scheme. The structure of the detector is shown Figure 2.5. Incident x-rays are absorbed in phosphor layer and optical photons are generated. Optical photons are absorbed in HARP layer and generate ehps near the top surface of the layer. Under a sufficiently high electric field holes move towards the bottom surface, and undergo avalanche multiplication. The holes are collected by the pixel electrodes which is read out with a two-dimensional array of a-Si:H TFTs.

2.2.1 Area of the Detector

If the incident x-ray beam is at the center of the detector area and is normal to the detector (see Figure 1.2), then the length of an ideal square detector, S_D, can be calculated by

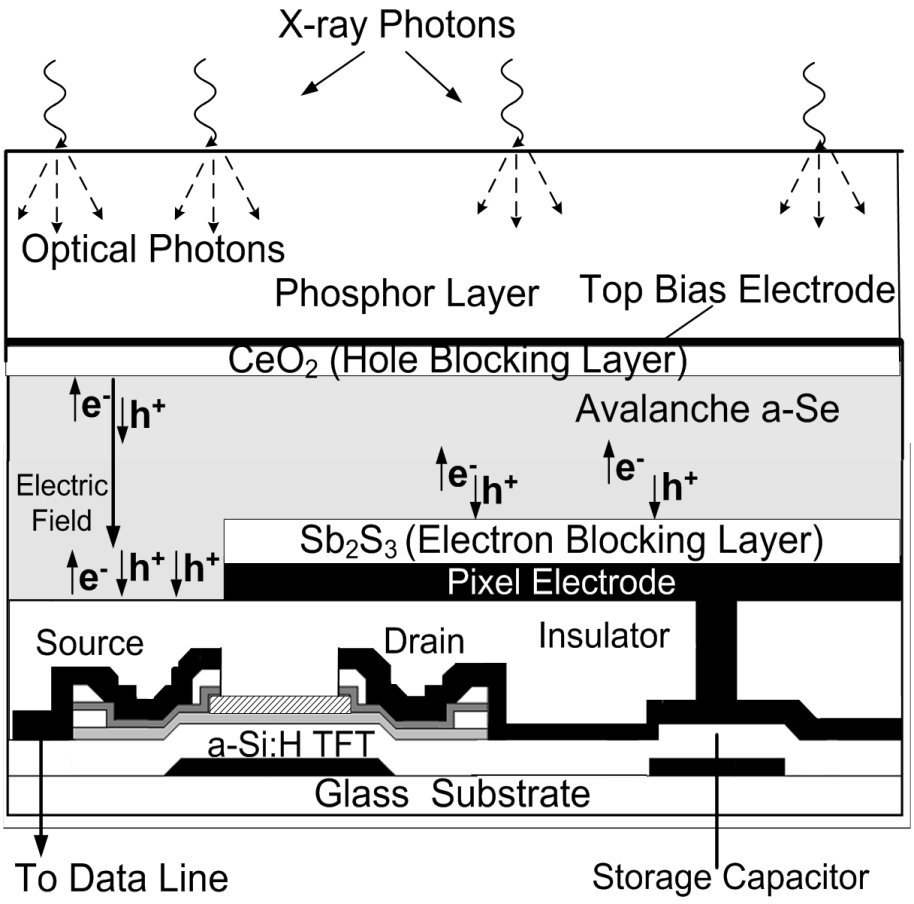

Figure 2.5: Cross section of a single pixel of the detector using indirect detection scheme.

[44]:

$$S_D = 2d_x \tan(2\sin^{-1}(\frac{\lambda}{2P})) \tag{2.6}$$

where P is the resolution, d_x is the crystal-to-detector distance, and λ is the x-ray wavelength. Using the values of P and λ from Table 1.1 and commonly used crystal to detector distance, d_x of 122 mm and 197 mm, we get from (2.6) S_D of 30 cm and 25 cm for ideal detectors for home laboratory and synchrotron respectively [5].

a-Si:H FP detectors can be uniformly and inexpensively fabricated over an area comparable to that required by a crystallographic detector. In fact, a-Si:H FP detector of similar sizes are already in the market for digital imaging applications.

2.2.2 Size of the Pixel

The minimum distance between Bragg spots can be determined by [44]:

$$x_B = \frac{d_x \lambda}{a_\circ} \tag{2.7}$$

where $a_\circ$ is the unit cell length of protein crystal. Protein crystals have a unit cell length between 50 $\mathring{A}$ to 500 $\mathring{A}$. Putting $a_\circ$ of 200 $\mathring{A}$, and d_x of 122 mm and 197 mm, we get x_B = 940 μm, and 985 μm for home laboratory, and synchrotron respectively [5]. To meet both the requirements that several pixels would hold a Bragg peak of 300 μm, and five or more pixels would fit between successive Bragg spots, the pixel size can be between 100 μm to 200 μm. With such a pixel size, indirect detection scheme will have similar spatial resolution as direct detection.

2.2.3 Size of Pixel Capacitor

The maximum charge storage capacity of a pixel is the product of the pixel capacitor, C_P and the voltage across this capacitor, V_P [23]. For a switch based pixel structure, V_P is initially zero and increases in proportion to the charge that accumulates in the capacitor. On the other hand, V_P is the voltage at the drain of the a-Si:H TFT. The maximum acceptable voltage at the drain of TFT for proper switching operation is reported to be $<$ 50 V [45], although high drain voltage would cause immense degradation of TFT characteristics in terms of threshold voltage and sub threshold slope. The impact of having high TFT drain voltage can be mitigated by proper biasing of TFT gate voltages, as is typical in display applications [46], [18]. Usually, a reasonable voltage at TFT drain is 15 V.

The maximum charge storage capacity determines the maximum signal that the detector can hold without pixel saturation. Since dynamic range is defined as the ratio of maximum to minimum signal, the size of C_P can be calculated from dynamic range requirements. The minimum signal for protein crystallography is one x-ray photon of 8 keV energy. The x-ray to charge conversion gain is 20 ehp/keV for regular a-Se. So the minimum signal is only 160 electrons per pixel whereas the electronic noise of the detector is 1000-3000 electrons per pixel for a-Si:H arrays [23], [24]. So it is evident that regular a-Se based detector cannot perform single photon detection. Avalanche a-Se can

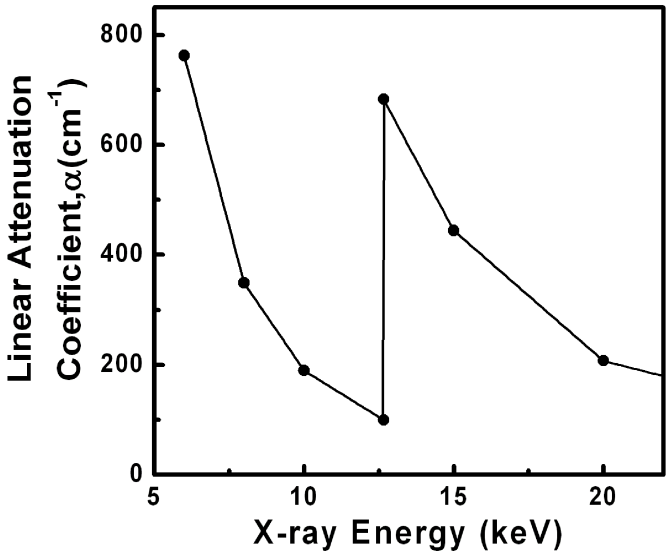

Figure 2.6: Variation of linear attenuation coefficient,$\alpha(E)$, of a-Se in the x-ray energy range for protein crystallography.

amplify the signal such that it can overcome the noise of the detector, making the detector sensitive to each incident x-ray photon.

According to *Rose's criterion*, the minimum signal should be 5 times the noise of the detector. If electronic noise per pixel is 1000 electrons, the minimum signal per pixel should be 5000 electrons. Considering a dynamic range of 10^5, the maximum signal per pixel becomes 5×10^8 electrons.

$$Maximum\ Signal = C_P \times V_P \tag{2.8}$$

$$C_P = \frac{5 \times 10^8 \times 1.6 \times 10^{-19}}{15} = 5.3\ pF \tag{2.9}$$

Therefore, the C_P of 5 pF will give a dynamic range of $\sim 10^5$.

2.2.4 Thickness of a-Se Layer

For direct detection scheme, the thickness of a-Se layer, d_{Se}, must be such that most of the incident x-rays are absorbed. The fraction of incident x-ray that are absorbed in the a-Se layer depends on its x-ray quantum efficiency (QE), $\eta(E)$, which is calculated as

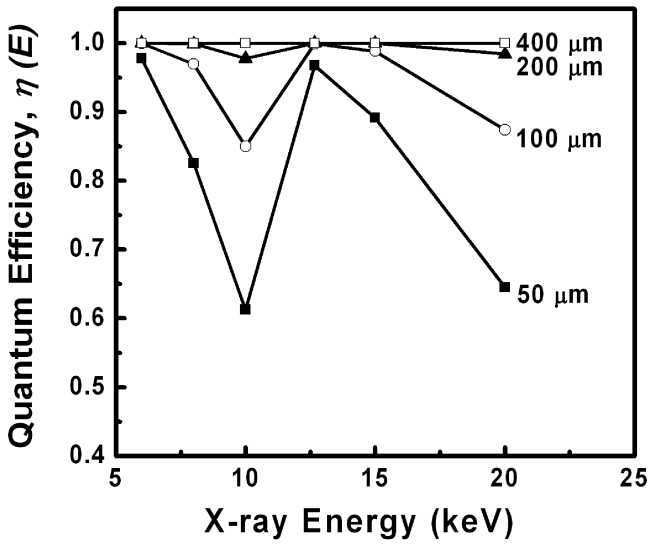

Figure 2.7: Variation of quantum efficiency, $\eta(E)$, of a-Se in the x-ray energy range for protein crystallography for different thickness of a-Se.

follows:

$$\eta(E) = 1 - \exp(-\alpha(E)d_{Se}) \tag{2.10}$$

here, $\alpha(E)$ is the photoelectric x-ray linear attenuation coefficient of a-Se which is a strong function of x-ray energy [28], [47]. The variation of $\alpha(E)$ and $\eta(E)$ of a-Se within the useful x-ray energy range is shown in Figure 2.6 and 2.7. There is an abrupt jump in the linear attenuation coefficient and quantum efficiency of a-Se at the photon energy of 12.66 keV (K-edge energy of a-Se) because of the onset of photoelectric interaction of x-rays with K-shell electrons.

As can be seen from Figure 2.7, for 100 μm thick a-Se, QE is 0.96 and unity for 8 keV (rotating anode source), and 12 keV (synchrotron source) respectively. To reach QE of unity for 8 keV the thickness of a-Se layer has to be 200 μm. However, the higher the thickness, the more bias voltage is required to establish high electric field across a-Se layer, which sometimes becomes technologically unfeasible. Therefore 100 μm is considered to be the optimal thickness of a-Se layer for direct detection scheme.

For indirect detection scheme, phosphor layer absorbs the incident x-rays and converts them to optical photons. a-Se layer is used to generate ehps from optical photons. Therefore, only 15 μm thick a-Se layer is sufficient to generate necessary avalanche gain

for single photon detection system. The advantage of this approach is that HARP structure can be directly used as the avalanche layer. Therefore no challenge is associated with developing or biasing a thicker (100 μm) a-Se layer.

2.2.5 Avalanche Gain and Operating Condition

To meet the sensitivity requirement, the detector should be quantum noise limited for the lowest possible signal which is one 8 keV x-ray photon per pixel. X-ray quantum noise, N_{qn}, is described by the Poisson probability distribution function, and it is square root of N for N x-rays. In practical state-of-the-art AMFPIs electronic noise of $\sim$ 1000 electrons per pixel are reported [23], [24]. Now,

$$Signal = Energy\ of\ x-ray \times Conversion\ Gain \times Avalanche\ Gain \tag{2.11}$$

For 8 keV X-ray with conversion gain of 59 ehp/keV and avalanche gain of 10, the signal becomes 4800 electrons. The referred values of conversion gain and avalanche gain are realistic for a-Se and already reported in literatures [24]. For 1 x-ray photon signal, the quantum noise is equal to the signal (4800 electrons per pixel), which is greater than the electronic noise (1000 electrons per pixel), making the detector quantum noise limited. A higher value of avalanche gain is not preferred as it will generate more ehps from each x-ray photon. The detector then can store less number of x-rays. So the x-ray storage capacity of the detector will be reduced.

Avalanche gain of a-Se, g_{av}, depends exponentially on a-Se thickness by [25]:

$$g_{av} = \exp(\gamma_p d_{Se}) \tag{2.12}$$

Here, γ_p is the field dependent IIC for holes. Figure 2.8 shows that γ_p in a-Se is strongly dependent on electric field, and is independent of the thickness of a-Se [35]. Avalanche gain is programmable by choosing the a-Se layer thickness and adjusting the applied bias voltage. For avalanche gain of 10, from (2.12) we get γ_p to be 0.023/μm for 100 μm thick a-Se layer. Figure 2.8 suggests that electric field of 83.5 V/μm is necessary to get γ_p of 0.023/μm. So for direct detection scheme, the top electrode of the detector should be biased to 8.35 KV (which is technologically feasible) to generate 83.5 V/μm electric field across 100 μm thick a-Se layer.

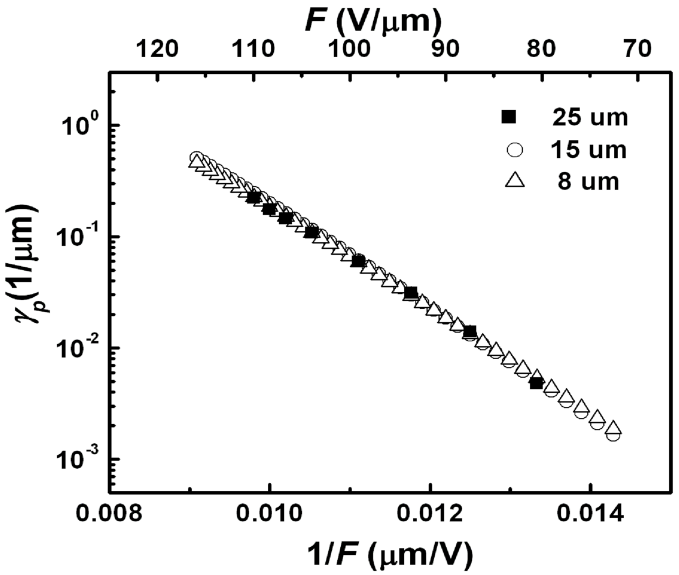

Figure 2.8: Field dependence of hole impact ionization coefficient for different a-Se layer thicknesses.

Using the similar approach, from (2.12) we calculated γ_p to be 0.15/μm for 15 μm thick a-Se layer. Figure 2.8 suggests that electric field of 97.3 V/μm is necessary to get γ_p of 0.15/μm. The lower the thickness of a-Se, the higher field will be required to produce the same gain. So for indirect detection scheme, the top electrode of the detector should be biased to 1.5 KV to generate 97.3 V/μm electric field across 15 μm thick a-Se layer. Applying 1.5 KV bias is technologically very convenient as existing flat panel mammography detectors use 5 KV for bias purpose.

Table 2.2 shows the optimal design parameters and operating conditions for the a-Si:H FP protein crystallography detector using both direct and indirect detection scheme.

2.3 Feasibility Analysis of the Detector

The performance of the detector is analyzed in terms of readout time, quantum noise limited operation, maximum signal capacity, and spatial resolution.

Table 2.2: Parameters and operating conditions for a-Si:H FP crystallography detector.

Parameter	Direct detection	Indirect detection
Pixel size	between 100 μm to 200 μm	between 100 μm to 200 μm
a-Se thickness	100 μm	15 μm
Pixel capacitor	5 pF	5 pF
Conversion gain in a-Se	59 ehp/keV[24]	NA
Avalanche gain in a-Se	10	10
Dark current in a-Se	0.004 nA/mm^2	0.004 nA/mm^2
Field across a-Se	83.5 V/μm	97.3 V/μm
System temperature	300K	300K

2.3.1 Readout Time

During readout, the charge stored in the storage capacitor is discharged to the data line through the a-Si:H TFT with a RC time constant (τ). Here, τ is the product of the pixel capacitance, C_P ($\sim$ 5 pF), and the ON resistance of the switching TFT, R_{ON} (typical value is $\sim$ 1.5 MΩ). For complete discharge of the stored charge on each pixel, it is necessary to wait for several time constants, say, 3 to 5 time constants Thus, the minimum time required to read the entire array,

$$T_{Read} = Number\ of\ rows \times 5 \times R_{ON} \times C_P \tag{2.13}$$

Let us consider a 25 cm $\times$ 25 cm detector with pixel size of 150 μm $\times$ 150 μm. So the number of rows will be 1667 (i.e. a 1667 $\times$ 1667 array). From (2.13):

$$T_{Read} = 1667 \times 5 \times 1.5 \times 10^6 \times 5 \times 10^{-12} = 0.06\ s. \tag{2.14}$$

Therefore, T_{Read} becomes only 60 ms. The short readout time is very beneficial for very large macromolecule complexes (e.g. Ribosome) whose crystals suffer rapid degradation in the x-ray beam.

2.3.2 Quantum Noise Limited Operation

For quantum noise limited operation the noise added by the detector should not exceed the x-ray quantum noise. The lowest possible x-ray quantum noise per pixel is equal to the number of electrons generated from a single x-ray photon of the lowest x-ray energy (8 keV).

$$N_{qn} = Energy\ of\ x-ray \times Conversion\ Gain \times Avalanche\ Gain \tag{2.15}$$

using conversion gain of 59 ehp/keV and avalanche gain of 10, we get quantum noise per pixel is 4800 electrons.

The noise per pixel of the detector comes from electronic noise of a-Se and a-Si:H pixel.

A. Electronic Noise of a-Se

The electronic noise of a-Se is due to the dark current shot noise which is caused by the thermal excitation in the bulk a-Se, and the charge injection from the bias electrodes. The dark current shot noise, N_{nd}, is determined by the dark current density of a-Se at each pixel and the time between successive readouts, and is given by [19],

$$N_{nd} = \sqrt{\frac{J_d \times A \times T_F}{e}} \tag{2.16}$$

where J_d is the dark current density of a-Se (0.004 nA/mm^2), A is the area of the pixel (150 μm^2), T_F is time between successive readout (60 ms), and e is the charge of an electron (1.6×10^{-19}). Using (2.16), we get the dark current shot noise per pixel is 183 electrons.

B. a-Si:H TFT Thermal Noise

When the TFT is on, thermal noise is generated by thermal agitation of electrons in the channel resistance, and is given by [48],

$$N_{nth} = \frac{1}{e}\sqrt{2kTC_P} \tag{2.17}$$

where k is the Boltzmann's constant (1.38×10^{-23}), T is the system temperature on the absolute scale (300), and C_P is the pixel capacitance (5 pF). Using (2.17), we get thermal noise per pixel is 1271 electrons.

Moreover, there are preamplifier noise ($\sim$ 1000 electron), data line thermal noise ($\sim$ 580 electron), and ADC (analog-to-digital converter) digitization noise ($\sim$ 480 electrons for 16-bit resolution ADC) [19], [48]. Since all the noise sources are independent, total noise is obtained by adding them in quadrature. Total electronic noise per pixel is 1700 electrons. So, quantum noise per pixel is more than two times the electronic noise per pixel of the detector, confirming quantum noise limited operation.

2.3.3 Maximum Signal Capacity

The maximum signal storage capacity of the detector is 5×10^8 electrons per pixel. This signal can be translated to number of x-ray photons by dividing it with conversion gain (59), avalanche gain (10), and the x-ray energy (E). For rotating anode source with 8 keV x-ray, the maximum number of x-ray that the detector can store becomes 6.25×10^4. Moreover, for home source the exposure time is 1 min. Since the detector has the ability to do readout in ms range, several readouts are possible within one exposure period, and the outputs can be added using software. Using the similar approach for synchrotron source (x-ray energy is 12 keV), it is found that 4.2×10^4 x-rays can be stored in the detector. Here the exposure time is small; as such multiple readout within one exposure is not possible.

2.3.4 Spatial Resolution

The Fourier transform is used to express spatially varying signals (i.e., images) in medical systems in terms of spatial frequencies (cycles per millimeter (cy/mm)) [49], [50]. The effect of image-blurring mechanisms in a-Se is represented both as two dimensional convolution integrals with a point-spread function (PSF) in the spatial domain and as multiplicative transfer functions in the spatial-frequency (Fourier) domain. Sinusoidal image patterns are transferred with only a scalar change in amplitude, and these factors are expressed as a spatial frequency-dependent modulation transfer function (MTF). By definition, the MTF is normalized to unity at zero spatial frequency.

The MTF of a-Se for the x-ray energy range of protein crystallography is extremely high and MTF is independent of the thickness of a-Se layer [51]. Thus, the spatial resolution of the detector will be determined by the pixel size of the readout array. Our proposed detector with pixel size of ~ 150 μm should provide adequate spatial resolution to accurately identify each diffraction spot.

2.3.5 Dynamic Range

The designed detector can have dynamic range higher than 10^5 by designing the TFT arrays with larger charge storage capacity, however, peripheral readout electronics (such as A/D converter) can be a limiting factor. One potential solution is to use the detector with variable avalanche and x-ray to charge conversion gain so that the number of charges generated from each x-ray photon can be varied. The avalanche and conversion gain can be controlled by adjusting the electric field across the selenium layer. However, dynamic bias change across Se layer is challenging as Se takes a while to stabilize. The best solution may be to have two detectors with two separate mode of operation: with and without avalanche gain. The high gain mode will generate more charge from each x-ray, so it will help to collect the details of the diffraction pattern, especially from the weak diffraction data. On the other hand, lower gain mode will produce less charge from each x-ray, and it will help to read the strong diffraction data. Finally, a combination of two sets of data can help to get a better diffraction pattern. Here, the only concern is the increase in readout time. However, our detector is able to read fast, and will still be able to meet the readout time requirement for crystallographic application.

2.4 Summary

We proposed a detector based on measured and known properties of a-Si:H TFT and a-Se photoconductor to meet the specific requirements for protein crystallography. The study shows that the proposed detector meets the area and readout speed requirements, and also provides wide dynamic range and high sensitivity. Thus, the proposed detector is expected to ease the study of protein structure, and underpin the development of new drugs.

Chapter 3

K-fluorescence Reabsorption in Selenium

In this chapter, the elementary theory of protein structure reconstruction using x-ray diffraction is discussed. Then multiwavelength anomalous diffraction (MAD) method for calculation the phase of protein structure is described. Physics of K-fluorescence is explained and the probability of K-fluorescence reabsorption of a-Se within the useful x-ray energy range of protein crystallography is calculated. Finally, possible consequences of K-fluorescence reabsorption of a-Se on the performance of a protein crystallography detector where a-Se is used both as an anomalous scatterer and a photoconductor is elucidated.

Protein Crystallography is a popular experimental technique based on x-ray diffraction to determine three dimensional (3D) atomic structure of proteins. An x-ray beam, incident on protein crystal is diffracted in numerous directions, and the direction and intensities of the diffracted beams are defined by the arrangement of the atoms in the unit cell of protein crystal [10].

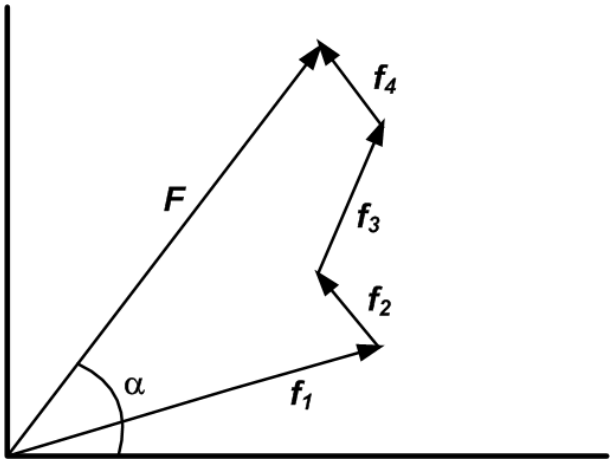

Figure 3.1: X-ray scattering by a unit cell of four atoms.

3.1 Protein Structure Reconstruction Using Diffraction

X-ray interacts with a crystal by its fluctuating electromagnetic wave which accelerates electrons inside the crystal. The accelerated electrons emit electromagnetic waves of the same frequency as the incident wave [10]. The wave scattered by the crystal can be described as a summation of enormous number of waves, each scattered by one electron of the crystal. Therefore, the result of a crystallographic experiment is not a map of the atoms, but a map of the distribution of the electrons in the atom, that is, an electron density map. Nevertheless, since the electrons are localized around the nuclei, the electron density map provides a reliable picture of the arrangement of the atoms.

Figure 3.1 shows how the phase and amplitude of the overall scattered wave arise from the individual scattered waves known as atomic scattering factors, f_j, in the unit cell at a position r_j of the crystal. The overall scattered wave is represented by a vector and is termed as the structure factor, F, because it depends on the arrangement (structure) of the atoms in the unit cell.

$$F(S) = \sum_{j=1}^{n} f_j exp(i2\pi r_j.S). \tag{3.1}$$

where S is the vector difference between the incident wave and the scattered wave. The vector S is called the scattering vector and is used to describe the position in diffraction space. Instead of summing all of the atomic scattering factors, $F(S)$ can be calculated by

integrating the electron density, ρ(r), over the unit cell:

$$F(S) = \int_{cell} \rho(r) exp(i2\pi r.S) dv. \tag{3.2}$$

If x, y, z are coordinates of the unit cell, and V is the volume of the unit cell, then:

$$dv = V\ dx.dy.dz \tag{3.3}$$

Again, the unit cell has dimensions of a, b and c in x, y and z directions respectively. So,

$$r.S = (ax + by + cz).S = a.S\ x + b.S\ y + c.S\ z = hx + ky + lz. \tag{3.4}$$

The conditions for scattering by a crystal are known as the Laue conditions and given as:

$$a.S = h,\ b.S = k,\ c.S = l. \tag{3.5}$$

Therefore, $F(S)$ is now written as:

$$F(h\ k\ l) = V \int_{x=0}^{1} \int_{y=0}^{1} \int_{z=0}^{1} \rho(xyz) exp(i2\pi(hx + ky + lz)) dx.dy.dz \tag{3.6}$$

In protein crystallography, the goal is to calculate the electron density $\rho(xyz)$ at each position, x, y, z in the unit cell. $\rho(xyz)$ is the Fourier Transform of $F(h\ k\ l)$; therefore $\rho(xyz)$ can be written as a function of $F(h\ k\ l)$ [10]. Also, since the diffraction occurs only in a discrete direction, the integration is replaced by the following summation:

$$\rho(xyz) = \frac{1}{V} \sum_{hkl} F(h\ k\ l) \exp(-i2\pi(hx + ky + lz)). \tag{3.7}$$

Now, $F(h\ k\ l)$ is a vector and can be expressed as:

$$F = |F| exp(i\phi). \tag{3.8}$$

Now, (3.7) can be written as:

$$\rho(xyz) = \frac{1}{V} \sum_{hkl} |F(h\ k\ l)| \exp[-i2\pi(hx + ky + lz) + i\phi(h\ k\ l)]. \tag{3.9}$$

Equation (3.9) shows the relation between the electron density and atomic structure factor, where $|F(h\ k\ l)|$ is the amplitude and $\phi(h\ k\ l)$ is the phase angle of the structure factor. From experimental measurements, the intensity of the diffraction pattern, $I(h\ k\ l)$,

is obtained, and the amplitude of the structure factor is determined by the following equation:

$$I(h\ k\ l) = C|F(h\ k\ l)|^2, \tag{3.10}$$

where C is a proportionality factor that depends on various experimental factors.

Although the magnitude $|F(h\ k\ l)|$ can be retrieved from the measured intensity of the diffraction pattern, no phase information, $\phi(h\ k\ l)$, can be extracted from diffraction experiments. If the phases were known, a picture of the molecule could simply be computed. But the phase information is lost in the experiment. As such, the principal challenge in determining protein structures from diffraction patterns lies in calculating the phases of the atomic structure factors.

The key methods of phase calculation are: isomorphous replacement, Multiwavelength anomalous diffraction (MAD), and molecular replacement [1].

i) In the isomorphous replacement method diffraction pattern is first measured using crystals of the target protein. These crystals are then soaked in a heavy atom (atom with high atomic number) solution to attach heavy atoms to the protein molecules in the crystal and diffraction patterns are measured from these crystals as well. From the difference between diffraction patterns of the target and heavy atom derivative, heavy atom positions in the unit cell are located using Patterson map. A Patterson map is a vector map where peaks represent vectors between heavy atoms. Protein phases are readily estimated once the heavy atom positions have been located.

   Heavy atoms have enough electrons around them so they cause a measurable change in the diffraction pattern of the native protein. In practice usually platinum, uranium, lead, gold and the lanthanides are used as heavy atom. The term "isomorphous" refers to the fact that ideally the only difference between the diffraction patterns of the native and heavy atom-soaked crystals should be due the heavy atoms. Thus the heavy atoms should bind to the protein in an isomorphous fashion so that they do not disturb any atoms of the protein. The "replacement" is a misnomer and a better description would be "addition".

ii) In MAD experiments all the necessary data can be collected from a single protein crystal measured at several wavelengths around the K-edge of a heavy atom bound to

protein. Since the intensities of the diffraction patterns differ it is possible to locate the positions of the anomalous scatters in the unit cell and derive phases from the information using the same techniques used in the heavy atom method. Selenium (Se) is often used as the heavy atom since its K-edge is located at a wavelength of 0.9795 $\mathring{A}$, which is readily accessible on most synchrotron x-ray sources [52].

iii) The prerequisite of molecular replacement method is, the target protein should possess a similar structure (approximately more than 25% sequence identity) to one protein for which the structure is already known. The correct orientation and position of the molecules of the target protein can be determined by placing the probe molecule in the unit cell and calculating its theoretical diffraction pattern. The probe molecule is then moved until the theoretical and experimental patterns match.

Among all the methods, multi-wavelength anomalous dispersion (MAD) has a growing utility in phase calculation due to the improvements in computing capabilities and specialized software [1]. In Chapter 2, we developed the concept of a novel x-ray detector for protein crystallography which employ an a-Se direct detection layer for x-ray to charge conversion and an a-Si:H flat panel TFT array for image readout. Designing such a high performance direct detection imager requires a complete understanding of the physics of x-ray interactions with a-Se. We are concerned about the performance of a-Se based direct detection imager if it has to absorb x-rays of K- edge energy of Se in order to incorporate MAD phasing. This specific issue will be addressed here.

3.2 Multiwavelength Anomalous Diffraction (MAD) Method

When x-rays are incident on a free electron, the scattered beam diffracts exactly by 180° in phase from the incident beam. Electrons inside atoms are not free as they are bound to the nucleus. The electrons of the heavy atoms are even more attached to the nucleus since they have higher nuclear charges. For bound electrons, the incident x-ray beam does not diffract exactly by 180°. Such a scattering from an inner shell electron is known as anomalous scattering (see Figure 3.2).

If the x-ray absorption coefficient of an atom is plotted as a function of the x-ray wavelength, a sharp change will be found in the otherwise smooth curve. The change in

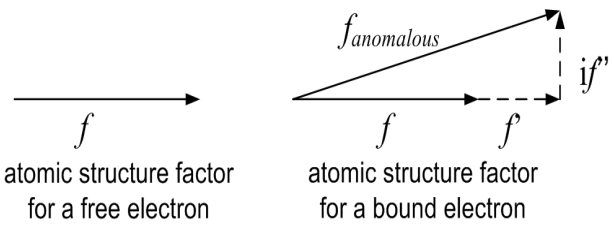

Figure 3.2: X-ray scattering of a free and a bound electron.

the curve is called an absorption edge and it is caused by absorption of the x-ray photon. At this wavelength an electron is ejected from the inner shell (say, K-shell) to a state in the continuous energy region. The largest change in the anomalous scattering factor occurs at the absorption edge since the value of atomic scattering factor is directly related to the atomic x-ray absorption coefficient. The effect of anomalous scattering is described mathematically by two correction terms which are added to atomic scattering factor, f, and is given by [10]:

$$f_{anomalous} = f + f' + if'' \tag{3.11}$$

Here f' is the real and f'' is the imaginary part of the correction term. Their values are related to the atomic x-ray absorption coefficient which depends on the wavelength of the incident x-ray [10]. The dependence of f'' on the x-ray energy can be determined experimentally by measuring the x-ray fluorescence emitted from the atom as a result of absorption of the incident x-rays. The value of f' can be calculated from f'' based on a theoretical approximation [53].

MAD utilizes the wavelength dependence phenomenon of the atomic scattering factor. The atomic scattering factor of a heavy atom bound to the protein is measured at a number of different x-ray energies near the absorption edge. The anomalous scattering factors of the heavy atom are significantly different from one another near the absorption edge. Since the intensities of the diffraction pattern differ, it is possible to locate the positions of the anomalous scatterers in the unit cell and derive the phases from the information using specialized software.

Using MAD for phase calculation is convenient since the majority of heavy atoms which bind to proteins (such as copper, iron, sulfur) have absorption edges in the energy range typically used for protein diffraction work, i.e., 6-20 keV. Moreover, protein structures contain large number of light atoms (hydrogen, carbon) for which the anoma-

lous scattering contribution is negligible. So the anomalous scattering contribution from heavy atoms becomes significant, and their positions can be located easily. The great advantage of the method is that the measurements can be done on one crystal, so no need to worry about changes in protein crystal structure. On the other hand, for isomorphous replacement or molecular replacement method crystal structure may change; first diffraction pattern is taken from target the protein crystal, then a molecule is added and another diffraction pattern is taken. Addition of a molecule sometimes can cause unwanted modification of protein crystal structure and destroy the phase information of the crystal structure.

3.3 Importance of Se as a Scatterer in MAD

MAD phasing is an excellent way to calculate the phase of a protein if it has a heavy atom (such as Fe (atomic number 26), Zn (30), or Cu (29)) attached to it that can act as an anomalous scatterer [10]. If no intrinsic anomalous scatterer is present, a scatterer can be introduced by soaking the protein in a heavy atom solution such as Se (34), Hg (80) or Pt (78). However, the absorption edges for Hg (K-edge at 78 keV) or Pt (K-edge at 82 keV) is beyond the working x-ray range of protein crystallography. Therefore, Se plays a major role as anomalous scatterer in the MAD method. The advantages of using Se as a heavy atom are:

i) The K-edge of Se is located at 12.67 keV, which is within the functional x-ray energy range,

ii) Replacement of Sulfur (16) by Se can be done biologically by incorporation of selenomethionine (SeMet) instead of methionine,

iii) SeMet protein has larger anomalous scattering signal (3.8 e) from selenium than the signal (1.14 e) from sulfur [52], [10].

The real (f') and imaginary (f'') parts of the anomalous scattering factor of Se as a function of x-ray energy are plotted in Figure 3.3. As shown in the Figure, the imaginary part (f'') of the scattering factor has a step at the K-edge ($\lambda_1 = 0.9793$ $\mathring{A}$), and the real part (f') has a dip at λ_2. The other two wavelengths for data collection are λ_3

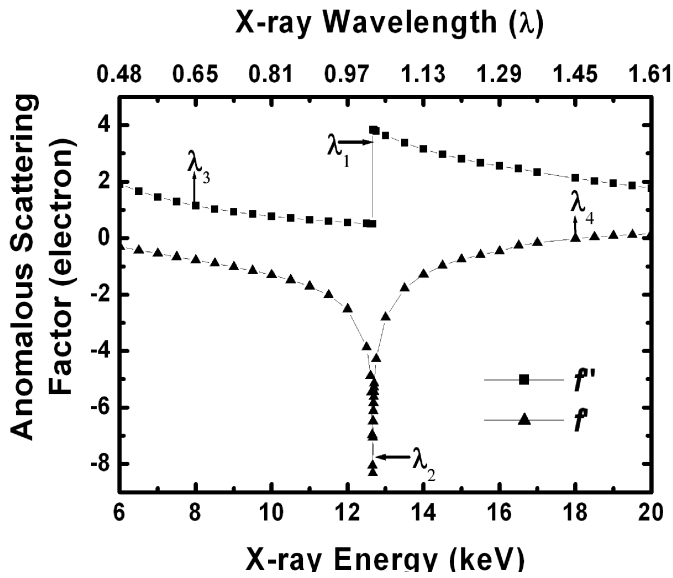

Figure 3.3: Variation of the real and imaginary parts of the anomalous scattering factor of Se plotted as a function of x-ray energy.

and λ_4, which are remote from the absorption edge. As the scattering factors of Se differ significantly at these wavelengths, the intensities of the diffraction beams also vary. Using this information it is possible to locate the positions of the heavy atom in the unit cell and hence derive the phases of atomic scattering factors [52], [10].

3.4 Interaction of X-ray with Se as a Photoconductor

The range of x-ray energies for protein crystallography is from 6 keV to 20 keV. These x-rays interact with Se by three different mechanisms: photoelectric effect, Rayleigh scattering and Compton scattering. The incident x-rays can be completely absorbed in Se (photoelectric effect) or scattered (Rayleigh or Compton scattering).

3.4.1 Photoelectric Effect

Here the total energy of the incident x-ray is transferred to an atomic electron known as the primary photoelectron. The primary photoelectron will use part of this energy to overcome the binding energy of the atom, and the remaining becomes the kinetic energy of the photoelectron. The atom becomes ionized. The energetic primary photoelectron

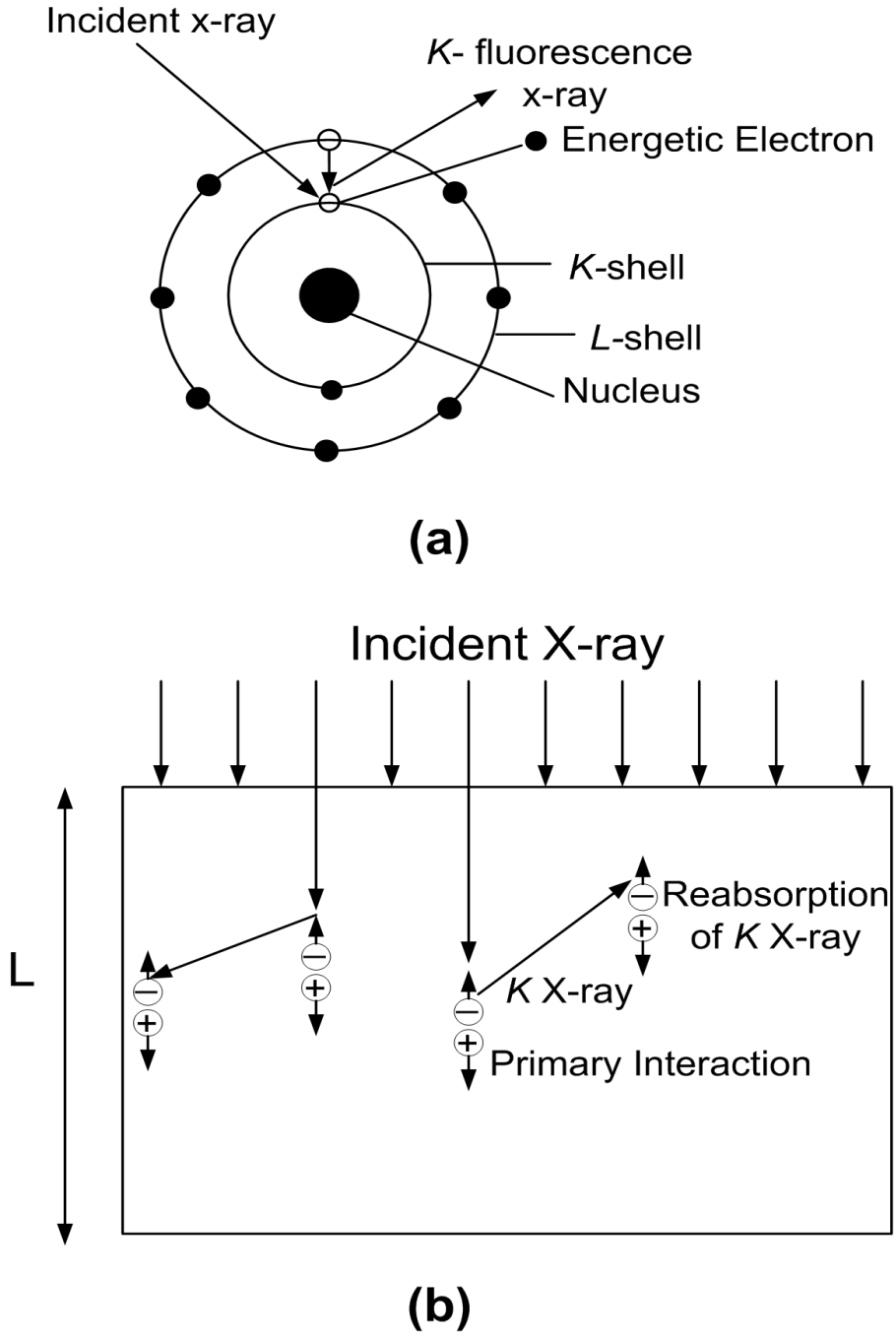

Figure 3.4: (a) Photoelectric effect showing the primary photoelectron and K-fluorescence x-ray (microscopic view), (b) Generation and reabsorption of K-fluorescence x-ray (macroscopic view.

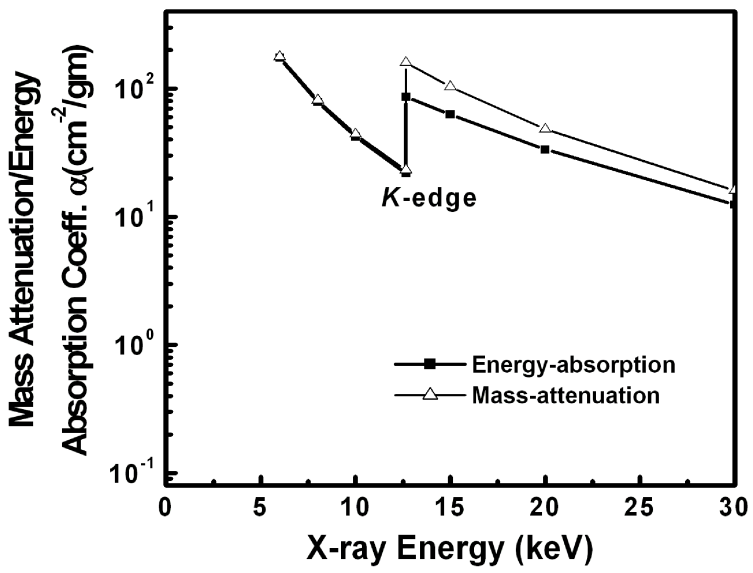

Figure 3.5: Variation of energy absorption and attenuation coefficient of Se with x-ray energy.

traverses some distance until it loses all its kinetic energy through collisions, releasing other electrons in the process. Due to the energy transfer of photoelectron to the Se bulk by ionization, a large number of free electrons and holes are generated which can be collected to form an image [54]. In addition, when this primary photoelectron is released, a vacancy is created in the corresponding atomic shell. When an outer shell electron jumps to the vacancy, it generates a characteristic x-ray with energy equal to the difference between the binding energy of the two shells as shown in Figure 3.4 (a). Alternately a series of non-radiative transitions involving Auger electrons can take place, resulting in the complete local deposition of energy.

If a vacancy in the K-shell is filled by an electron from the L-shell, the characteristic x-ray is called K_α fluorescence and if filled by a M-shell electron, K_β fluorescence. The fluorescence x-ray photon can either escape from or be reabsorbed in the Se layer (see Figure 3.4 (b)). If reabsorption occurs, electron and holes are released at some lateral distance from the primary interaction site.

The photoelectric effect is the dominant interaction mechanism in Se for x-rays in the range of 6 to 20 keV. Without considering the secondary x-ray photon absorption of photoelectric process, the average energy absorbed in Se by x-ray interaction is described

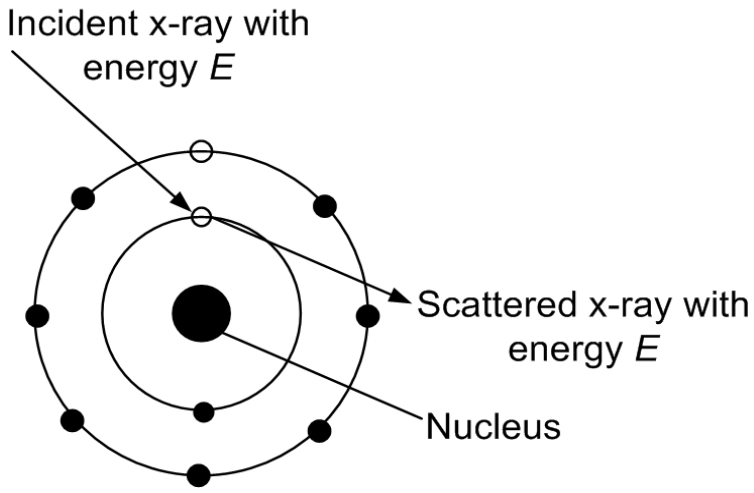

Figure 3.6: In Rayleigh scattering x-ray interacts with an electron and is scattered with same energy.

by energy absorption coefficient (α_{en}) and the total attenuation coefficient (α). α_{en} and α of Se as a function of x-ray energy is shown in Figure 3.5 [55]. There is an abrupt jump in the attenuation and energy absorption coefficients of Se at 12.66 keV because of the onset of photoelectric interaction of x-rays with K-shell electrons.

3.4.2 Rayleigh Scattering

Rayleigh scattering involves the elastic (coherent) scattering of x-rays by atomic electrons. The energy of the scattered x-ray is identical to that of the incident x-ray since no energy is transferred from x-ray to Se. However, the scattered x-ray experiences a change in its trajectory relative to that of the incident x-ray (see Figure 3.6), and this has a deleterious effect in x-ray imaging, where the detection of scattered x-rays is undesirable.

3.4.3 Compton Scattering

Compton scattering involves the inelastic (incoherent) scattering of an x-ray photon by an atomic electron. Here the incident x-ray gives part of its energy to the electron generating an energetic electron and an ionized atom. The scattered photon has lower energy than the incident x-ray (see Figure 3.7). Thus some energy is transferred to Se in Compton scattering event. Compton scattering typically occurs when the energy of the

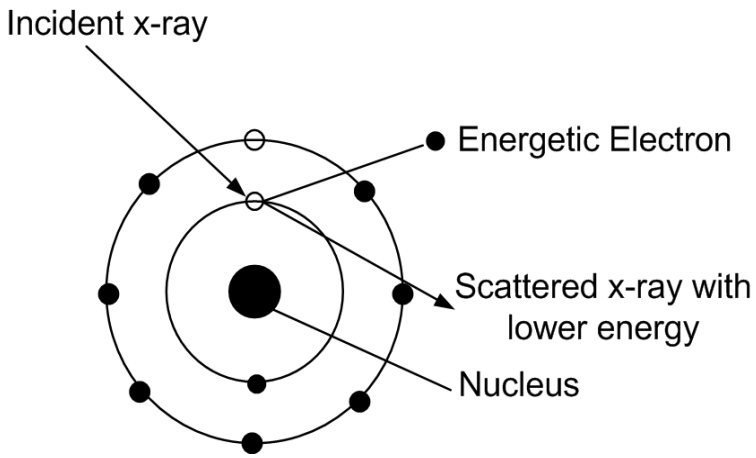

Figure 3.7: In Compton scattering x-ray interacts with an electron and is scattered with a lower energy.

x-ray photon is much greater than the binding energy of the atomic electron of Se. For low x-ray energy range, as in protein crystallography, compton scattering has a negligible contribution.

3.5 Calculation of the Probability of *K*-fluorescence Reabsorption

For MAD phasing the incident x-ray energy is almost equal to the *K*-edge energy of Se. Therefore, there is a possibility of generation and reabsorption of *K*-fluorescence at or above the *K*-edge of Se. The reabsorption of a fraction of the generated *K*-fluorescence is a random process which leads to fluctuations in conversion gain and hence addition of image noise [56], [54].

Here the probability of *K*-fluorescence reabsorption close to the *K*-edge of Se is calculated. The calculation presented here is based on the method described in [57], and using the following assumptions:

i) X-ray photons are incident normally on Se layer,

ii) Energy deposition in Se is due to photoelectric effect only,

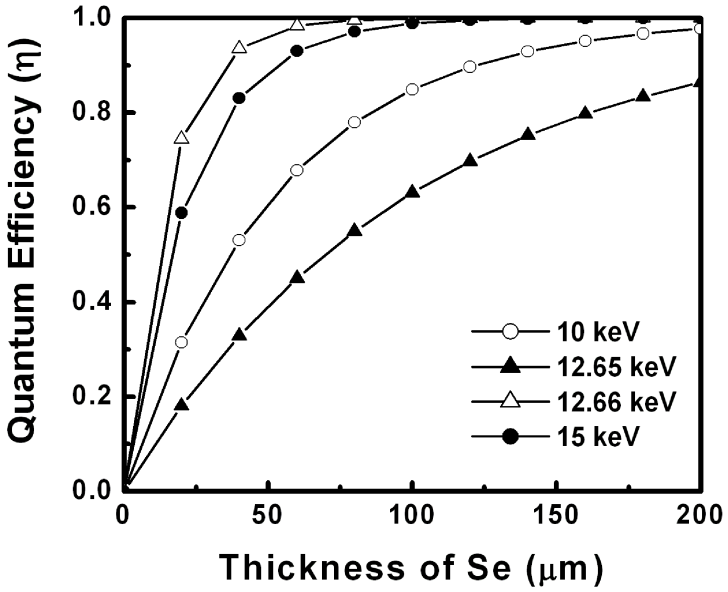

Figure 3.8: Variation of quantum efficiency of Se as a function of its thickness for different x-ray energy.

iii) Energy deposition due to secondary processes of photoelectric effect are neglected except for the reabsorption of the K-fluorescence,

iv) K-fluorescence photons are emitted isotropically, and

v) If the K-fluorescence x-ray interacts in the material, it is assumed to be completely absorbed.

3.5.1 X-ray Absorption in Se

The fraction of incident x-ray photons that are absorbed in Se is called the quantum efficiency (η) of the imager which is determined by α and the thickness (L) of Se:

$$\eta = 1 - \exp(-\alpha L) \tag{3.12}$$

The variation of η with thickness of Se for different x-ray energies is plotted in Figure 3.8. The figure shows that η increases with Se thickness, and there is large variation in x-ray absorption at the K-edge energy. For example, for 100 μm thickness of Se, there is $\sim$36 % change in absorption between 12.65 keV and 12.66 keV x-ray energy.

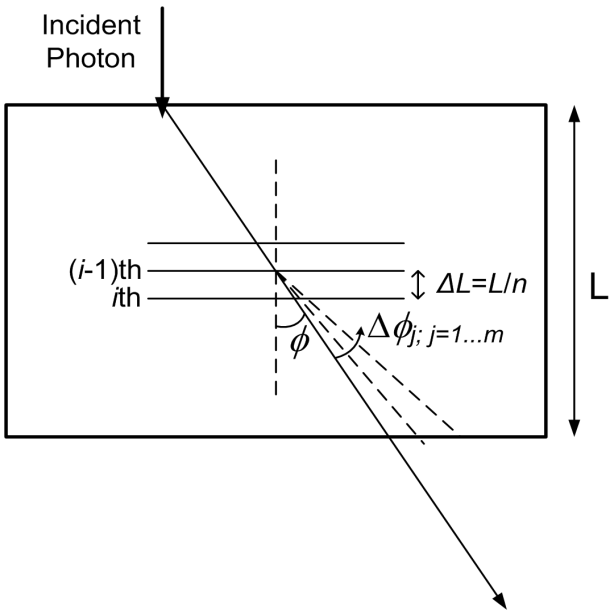

Figure 3.9: Cross section of Se of thickness L showing the geometry of x-ray interaction.

3.5.2 *K*- fluorescence Per Incident X-ray Photon

In order to calculate the probability of K-fluorescence generation and its subsequent reabsorption, we consider an L μm thick Se sample comprised of n layers (Figure 3.9). The probability of producing a K_x fluorescence x-ray (where x can be either α or β) at the i-th layer for an incident photon of energy E is given by [57]:

$$PKG_{ix} = f_{ph} f_K \omega_K I_x (\exp[-\alpha(i-1)\Delta L] - \exp[-\alpha i \Delta L]) \tag{3.13}$$

here,

$$f_{ph} = \frac{\alpha_{pe}}{\alpha} \tag{3.14}$$

f_{ph} is the fraction of total attenuation that contributes to photoelectric interaction, and it is almost unity for the 6-20 keV x-ray energy range. f_K is the K-shell contribution to the photoelectric effect (0.864), ω_K is the K-fluorescence yield (0.596), and I_x is the relative frequency of K_α (0.862) and K_β (0.138) [58]. Summation of PKG_{ix} over the n layers yields the total probability of K_x fluorescence generation.

$$PKG_x = \sum_{i=1}^{n} PKG_{ix}. \tag{3.15}$$

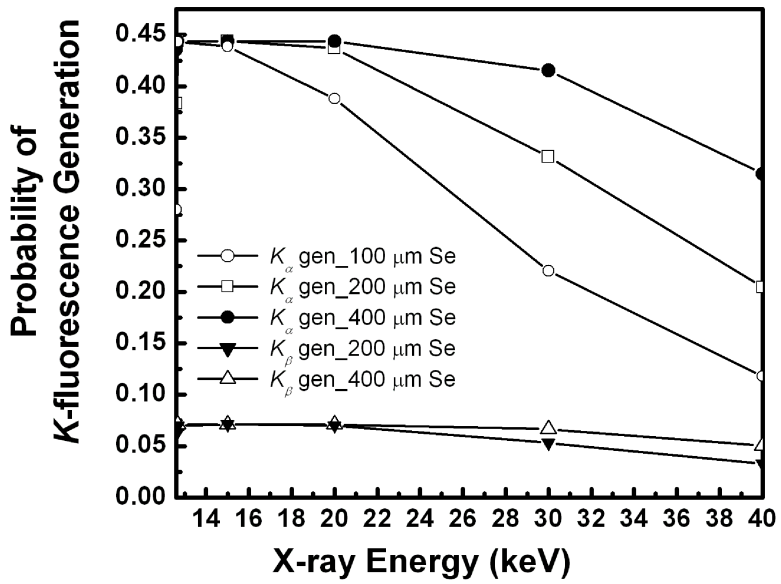

Figure 3.10: Probability of K_x-fluorescence generation calculated using (3.15) for different thickness of Se as a function of incident x-ray energy.

Figure 3.10 shows the probability of producing a K_x fluorescence x-ray for different thickness of Se layers. The figure shows that the probability of producing a fluorescence x-ray increases with Se thickness.

3.5.3 Reabsorption of *K*-fluorescence X-ray

A fraction of the generated K-fluorescence escapes from the Se layer and the remainder is absorbed in the layer. The absorption probability for a K_x photon originating from the i-th layer is PKA_{ix}. The K_x photon has energy below that of K-edge. K_α has energy of 11.21 keV and K_β has energy of 12.5 keV. Here α_x is the attenuation coefficient at the energy E_x of the K_x photon, and it is 148.823 cm^{-1} and 103.092 cm^{-1} for K_α and K_β x-ray respectively. The solid angle 4π subtended at the center of the layer is divided into $2m$ solid angle elements (see Figure 3.9). The j-th solid angle element, $\Delta\phi_j$, is obtained from integration of the solid angle between (j-1) and j-th polar angles.

$$\Delta\phi_j = 2\pi[\cos(j-1)\Delta\phi - \cos(j)\Delta\phi],\ j = 1, 2, ...2m. \tag{3.16}$$

Using assumptions (iv) and (v) mentioned in Section 3.5, the absorption probability

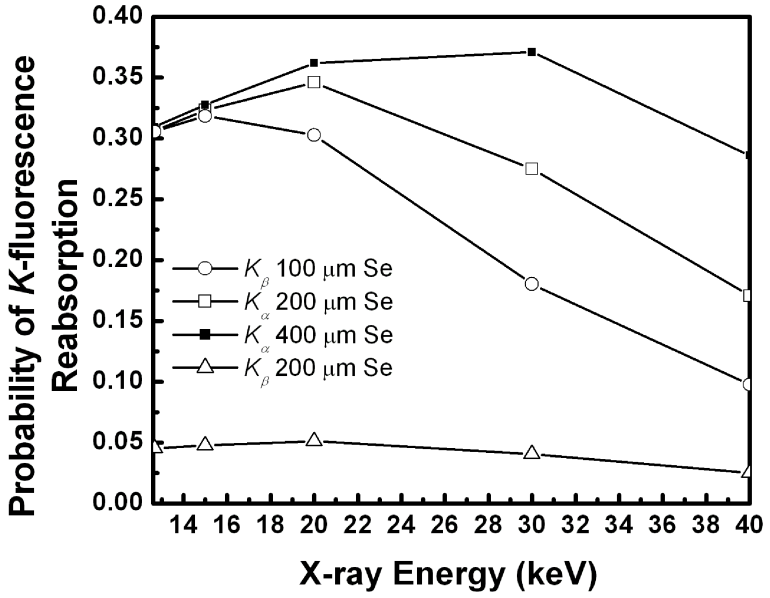

Figure 3.11: Probability of K_x-fluorescence reabsorption calculated using (3.19) for different thickness of Se as a function of incident x-ray energy.

can be calculated as:

$$PKA_{ijx} = \frac{\Delta\phi_j}{4\pi}[1 - \exp(-\alpha_{Ex}\frac{(n - i + \frac{1}{2})\Delta L}{|\cos(j - \frac{1}{2}\Delta\phi)|})],\ j = 1, 2, ...m. \tag{3.17}$$

$$PKA_{ijx} = \frac{\Delta\phi_j}{4\pi}[1 - \exp(-\alpha_{Ex}\frac{(i - \frac{1}{2})\Delta L}{|\cos(j - \frac{1}{2}\Delta\phi)|})],\ j = m + 1, ...2m. \tag{3.18}$$

It should be mentioned that all PKA_{ix} are dependent on the attenuation coefficient of the K_x photon, and independent of the angle and energy of incident photon. Now, the total probability of K_x reabsorption for an incident x-ray of energy E is given by,

$$PKR_x = \sum_{i=1}^{n} PKG_{ix}PKA_{ix}. \tag{3.19}$$

The probability of K_x reabsorption per K_x x-ray emitted or the fraction of K-fluorescence reabsorbed, is given by,

$$PK_x = \frac{PKR_x}{PKG_x} \tag{3.20}$$

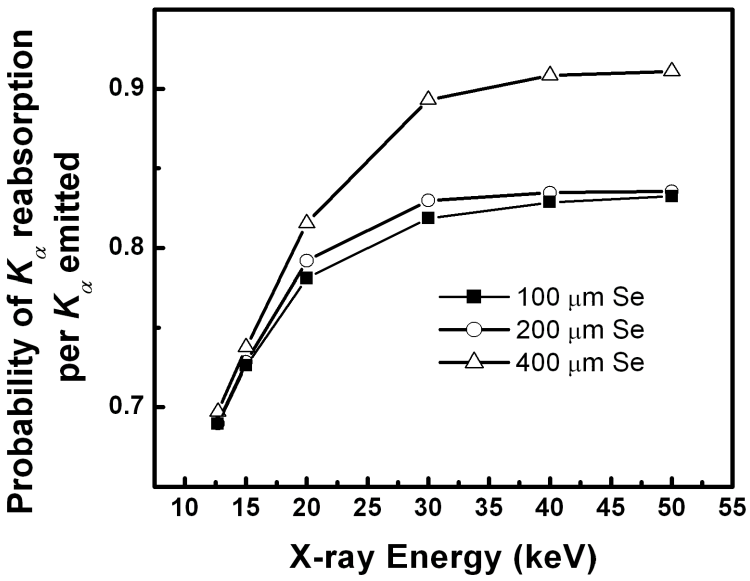

Figure 3.12: Probability of K_x-fluorescence reabsorption per K_x x-ray emitted calculated using (3.20) for different thickness of Se as a function of incident x-ray energy.

The variation of PKR_x and PK_x as a function of incident x-ray energy is plotted in Figure 3.11, and Figure 3.12. Figure 3.11 shows that the total probability of K_β reabsorption is less than that for K_α for all incident x-ray energies. This is due to the higher energy and hence lower reabsorption of K_β photons compared to K_α photons. Figure 3.12 shows that the probability of reabsorption is lowest just above the K-edge energy, and then increases with x-ray energy. This can be explained as higher energy x-rays interact deeper in the detector, and reabsorption probability increases. Thickness dependence in the reabsorption probability is seen in Fig. 3.12 which can be attributed to fact that, for thicker Se layer, chance of K-fluorescence escape from the exit side of Se layer becomes lower, while the likelihood of incident photons interaction and K-fluorescence reabsorption in the first few Se layers remains constant.

3.6 Impact on Use of Se for Direct Detection Protein Crystallography

The x-ray energy usually used for protein crystallography is between 6 to 20 keV. When the incident x-ray energy is below the K-edge, there will not be any generation and

reabsorption of K-fluorescence. Depending on the quantum efficiency of the imager, incident x-rays will be absorbed in Se and converted to charge locally without any image blurring. Since no K-fluorescence will be produced, the noise associated with the imager will be quantum noise and a noise associated with x-ray to charge conversion stage, which is described by the Swank factor of the conversion gain.

However, when the incident energy is at or above K-edge, as in the case for MAD, the performance of the imager will degrade since reabsorption of K-fluorescence introduces a secondary noise source from the inherent variation of secondary conversion process. At the same time, there will be stochastic blurring due to the reabsorption of K-fluorescence at a remote location. Generally, the effect on noise of variation of conversion gain is expressed by the Swank factor. Due to the presence of secondary noise, the Swank factor of conversion gain will decrease. The Swank factor can be calculated from the pulse height distribution (PHD), which is generated by assuming that the conversion gain of the system is Poisson distributed about the mean number of secondary electrons [59].

Previous investigations showed that K-fluorescence reabsorption affects both the modulation transfer function (MTF) and noise power spectrum (NPS) of the a-Se based imager, and can potentially decrease the detective quantum efficiency (DQE) by up to 50% at the K-edge [54]. So operating an imager near its K-edge energy should in general be avoided to maintain the highest DQE and spatial resolution. However in the case of MAD it is essential to operate the imager at the K-edge. One approach to using the a-Si:H detector with direct detection scheme is to use any material other than Se as the scatterer.

Another solution is to use the a-Si:H detector with indirect detection scheme where a phosphor layer (CsI or Gd_2O_2S) will convert x-ray to optical photons. Since the K-edge of phosphor material is far away from Se K-edge, there will be no problem in using Se as the scatterer in MAD method for phase calculation.

3.7 Summary

In this chapter, we discussed Multiwavelength anomalous diffraction (MAD) method for calculating the phase of protein structure. MAD utilizes the wavelength dependence

phenomenon of the atomic scattering factor, and requires x-ray measurement data around the K-edge of Se. We also investigated the phenomenon of K-fluorescence generation and reabsorption in Se. Our calculation shows that K-fluorescence reabsorption probability does not depend significantly on the energy of the incident x-ray, but it does increase with the thickness of Se. The results presented here will be used in Chapter 5 for characterizing the performance of a-Se based imager for protein crystallography.

Chapter 4

Integration of Avalanche a-Se with a-Si:H Thin Film Technology

This chapter presents the details of integration of an avalanche a-Se detector with a-Si:H pixel. A single pixel is integrated with a HARP (high field avalanche rushing photoconductor) and signal readout is done as a proof of concept.

Amorphous silicon technology has made it possible to build large area x-ray detectors with a level of performance far above the classic film screen, with the additional capability of real time operation. a-Si:H TFTs are used as the pixel switching element in these large area flat panel detectors. For a direct detection x-ray imager, spatial resolution depends on the pixel size only. Since good spatial resolution is required for high performance imaging the size of the TFT should be minimized.

4.1 a-Si:H TFT Array for Protein Crystallography Detector

a-Si:H TFT is a field effect transistor with three terminals: gate, source and drain. The applied bias voltage at the gate terminal controls the charge accumulation in the a-Si:H active layer between source and drain terminals. This results in a controlled flow of

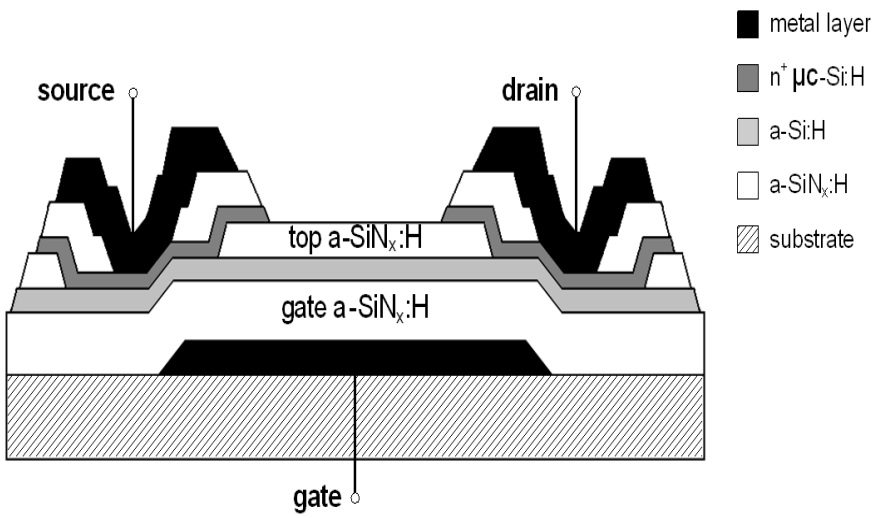

Figure 4.1: Schematic cross-section of an inverted staggered top passivated TFT.

current from drain to source. The summary of a-Si:H TFT device operation is described in Appendix A. The inverted staggered TFT with amorphous silicon nitride (a-SiN$_x$H) gate insulator and a top passivation nitride layer shows the best performance as the defect states at the top interface (between a-Si:H and a-SiN$_x$H) are minimized [60].

4.1.1 Design and Fabrication of a-Si:H TFT Array

For practical design of active matrix arrays and in order to have a high pixel fill factor, the pixel electrode is built above the rest of the active matrix structure (TFTs, capacitors, gate lines and data lines). This method of building pixel electrode is referred to as a mushroom structure, and this method is adopted in our design. Here pixel electrodes occupy most of the pixel area and are separated by a minimum gap (5 μm for the current industry design rules). With this design, fill factor can be higher than 95% for the detector for protein crystallography.

We designed prototype a-Si:H pixels and arrays for integration with avalanche a-Se and proof-of-concept. The pixel area is 175 μm $\times$ 175 μm which consists of a 5 pF storage capacitor and an inverted staggered a-Si:H TFT with an aspect ratio (W/L) of 54 μm/18 μm. To investigate the effect of pixel area on spatial resolution, we designed similar arrays with pixel area 250 μm $\times$ 250 μm, and 500 μm $\times$ 500 μm where the TFT aspect ratio is 83 μm/18 μm, and 200 μm/18 μm respectively. The mask layouts of the

Table 4.1: Thicknesses of different layers in a-Si:H TFT

Layer	Thickness (nm)
Mo gate Metal	120
a-SiN_xH gate dielectric	250
a-Si:H active layer	50
n^+ μc-Si:H	30
Al metalization	500

arrays are shown in Appendix B.

TFT arrays were fabricated in Giga to Nano Electronics Lab, University of Waterloo. The schematic structure of an inverted staggered TFT is shown in Figure 4.1. The TFT is fabricated by the standard lithographic technique using five masks. First the gate metal layer, usually Mo, is deposited on glass wafer and patterned (Mask-1). Then an a-SiN_xH /a-Si:H/a-SiN_xH tri-layer is deposited at a temperature of 260 °C. The top a-SiN_xH layer is patterned (Mask-2) to open source and drain contacts. Next, a thin n^+ μc-Si:H layer is deposited followed by another a-SiN_xH protective layer. The top a-SiN_xH protective layer is then patterned (Mask-3), which enables the following patterning of the n^+ μc-Si:H layer to isolate source and drain. Then the contact vias are opened (Mask-4) in the a-SiN_xH protective layer. Finally metal (Al) is deposited and patterned (Mask-5) to define source and drain of the TFT. The commonly used thicknesses of the layers are summarized in Table 4.1. Details of the fabrication process have been previously reported in literature [61].

The storage capacitor is created between the gate metal and the Al metal using a-SiN_xH as the dielectric layer (Mask-1 and Mask-5). The capacitance of the nitride layer was measured to be 25 nF/cm^2. So to get a capacitor of 1 pF, the required area is 100 μm $\times$ 40 μm. Two additional layers are required to make the a-Si:H TFT array compatible for integration with avalanche a-Se photoconductor. First a thick a-SiN_xH dielectric layer is deposited on top of TFT Al metalization layer. This dielectric layer will work as spacer. Then a via is etched (Mask-6) and a final Al metalization layer is

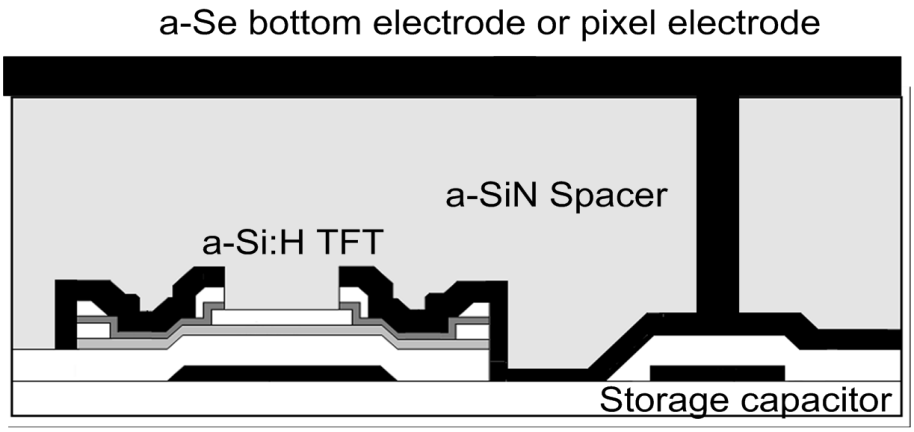

Figure 4.2: Cross-section of a pixel compatible for integration with a-Se.

!

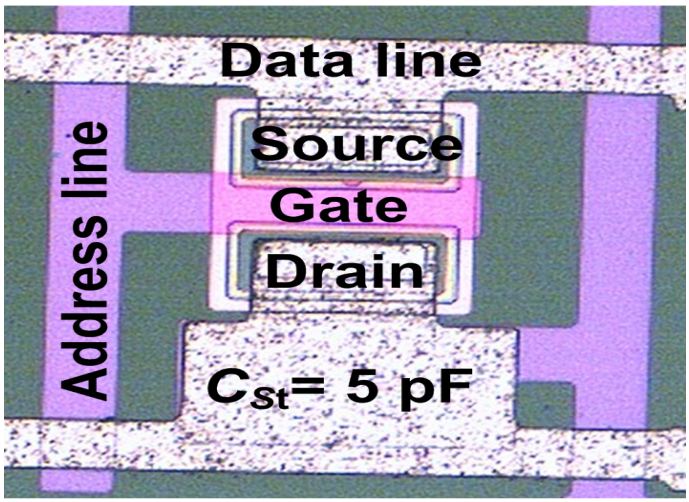

Figure 4.3: Micrograph of the fabricated pixel with 175 μm $\times$ 175 μm area (pixel electrode is not included).

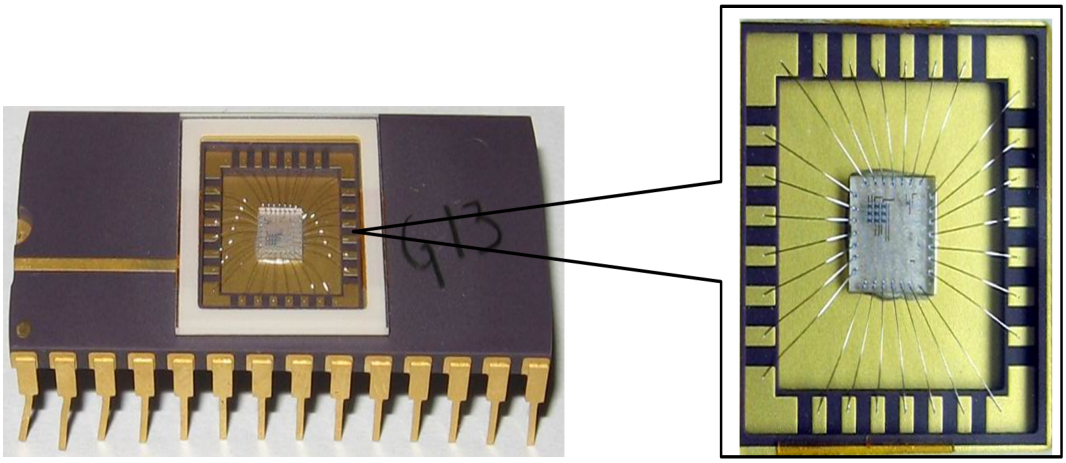

Figure 4.4: Picture of a chip with wire bonded a-Si:H TFT arrays.

deposited and patterned (Mask-7). The top Al layer defines the pixel electrode or the bottom electrode of the a-Se photoconductor. Figure 4.2 shows the cross-section of one pixel and Figure 4.3 shows the micrograph of the fabricated pixel.

4.1.2 Device Characterization of a-Si:H TFT

The fabricated a-Si:H TFT arrays were diced, and wire bonded in a ceramic package as shown in Figure 4.4. Device characteristics of a fabricated a-Si:H TFT with an aspect ratio (W/L) of 54 μm/18 μm were measured using Agilent 4156 Semiconductor Parameter Analyzer. a-Si:H TFTs were annealed at 180 °C for 3 hours and cooled for $\sim$ 10 hours at room temperature before each measurement.

A. Transfer Characteristics

The gate to source voltage, V_{GS}, of the TFT was varied from -5 V to +15 V for two different drain to source voltage, V_{DS}, and the output current, I_{DS}, was measured. Figure 4.5 (a) shows the transfer characteristics (I_{DS} vs V_{GS}) of TFT where ON-OFF ratio is 2.5×10^7 and 5×10^7 for V_{DS} equal to 1 V and 10 V respectively, which is adequate for functioning as an electronic switch.

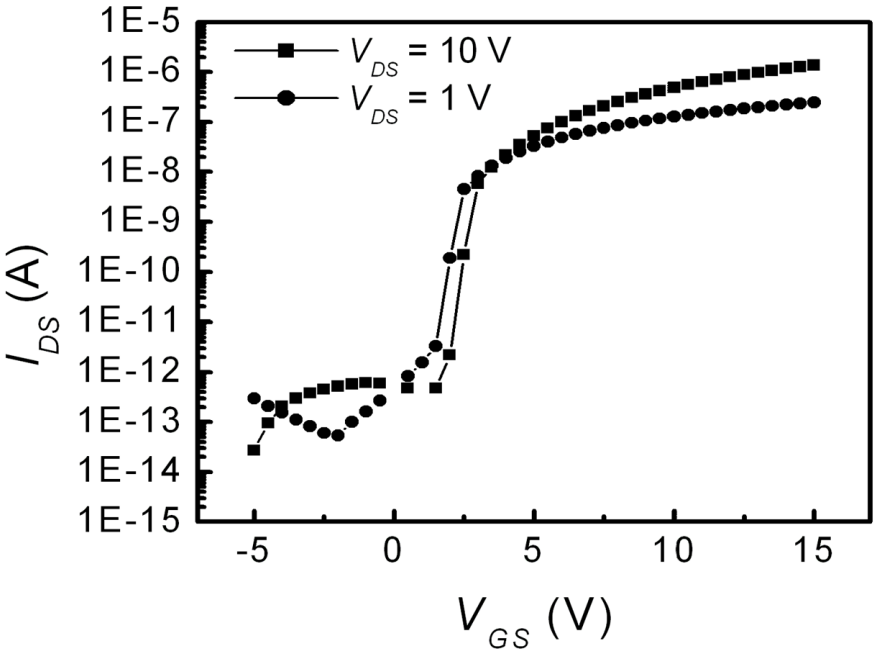

(a)

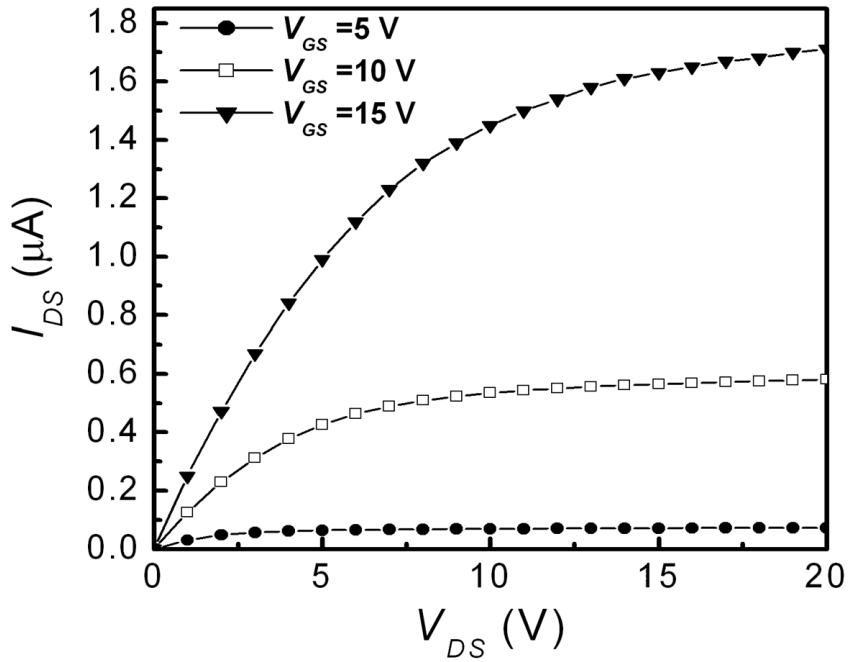

(b)

Figure 4.5: (a) Transfer characteristics (I_{DS}-V_{DS}) of the TFT demonstrating significant difference in I_{DOFF} (at V_{GS}= -5 V) and I_{DON} (at V_{GS}=15 V); (b) Output characteristics of a-Si:H TFT (I_{DS}-V_{DS}) for different gate voltages.

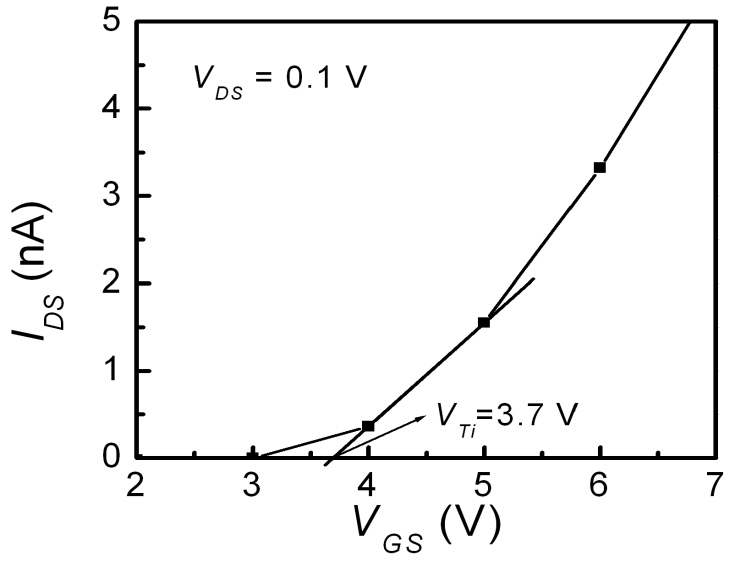

Figure 4.6: V_T extraction from transfer curve of the TFT.

B. Output Charactetistics

V_{DS} of the TFT was varied from 0 V to +20 V for different V_{GS}, and I_{DS} was measured. The output characteristic (I_{DS} vs V_{DS}) of the TFT is shown in Figure 4.5 (b), where the linear behavior of the I - V curve at low V_{DS} voltages indicates a good quality ohmic contact between drain-source and the channel.

C. Threshold Voltage, V_T

The threshold voltage, V_T, of the TFT was determined by linear extrapolation of the transfer curve while operating the TFT in the linear region. From Figure 4.6 we get V_T of 3.7 V. The V_T values for all of the fabricated TFTs were within $\pm$0.1 V from this value.

D. TFT ON Resistance, R_{ON}

We extracted R_{ON} of a-Si:H TFT with an aspect ratio of 54 μm/18 μm. We measured the output characteristics (I_{DS}-V_{DS}) of the TFT and extracted R_{ON} to be 5 MΩ from the slope of the output curve (see Figure 4.7). For the TFT with an aspect ratio of 83 μm/18 μm, R_{ON} was extracted to be 1.5 MΩ. This is because for linear region of

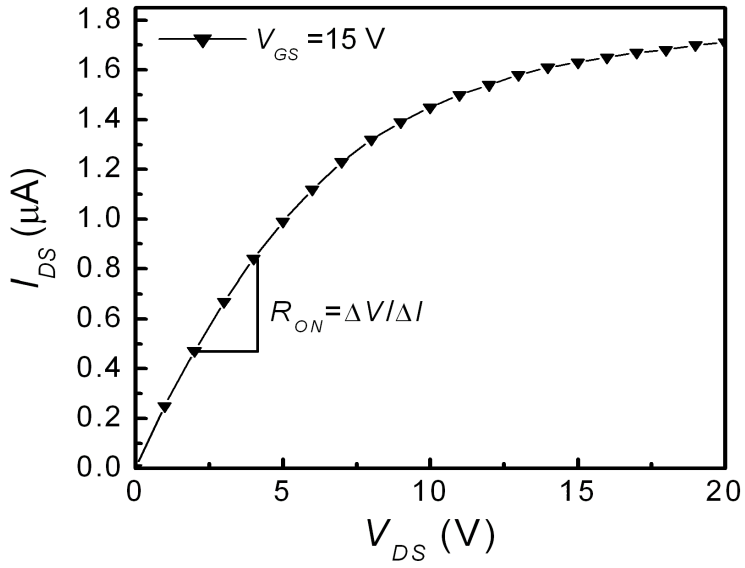

Figure 4.7: R_{ON} extraction from the output curve of the TFT.

TFT operation, R_{ON} can be approximately expressed by:

$$R_{ON} = [\frac{W}{L}\mu_{eff}C_G(V_{GS} - V_T)]^{-1}. \tag{4.1}$$

here , μ_{eff} is the effective carrier mobility, W is the width, L is the length and C_G is the per unit gate capacitance. From (4.1) it is evident that the higher the aspect ratio, the lower the resistance.

4.2 Characteristics of Avalanche a-Se

The use of avalanche a-Se layer to provide high gain for digital x-ray imaging is novel. To date it has been employed in optical imaging as phototargets of HARP TV camera tubes where the surface of a-Se phototarget is scanned by an electron beam. The application of avalanche multiplication in HARP tube provides extremely high sensitivity for optical light permitting the production of high definition images even in very low light conditions. The structure of a-Se HARP targets is carefully engineered to withstand the high field required for avalanche. This is made possible by blocking contacts which permit charge generated in a-Se to reach the electrodes yet prevent injection of charge carriers from the bias electrodes into the a-Se. A layer of CeO_2 prevents injection of positive charge from the anode (ITO), while a Sb_2S_3 blocking contact stops injection of negative charge from

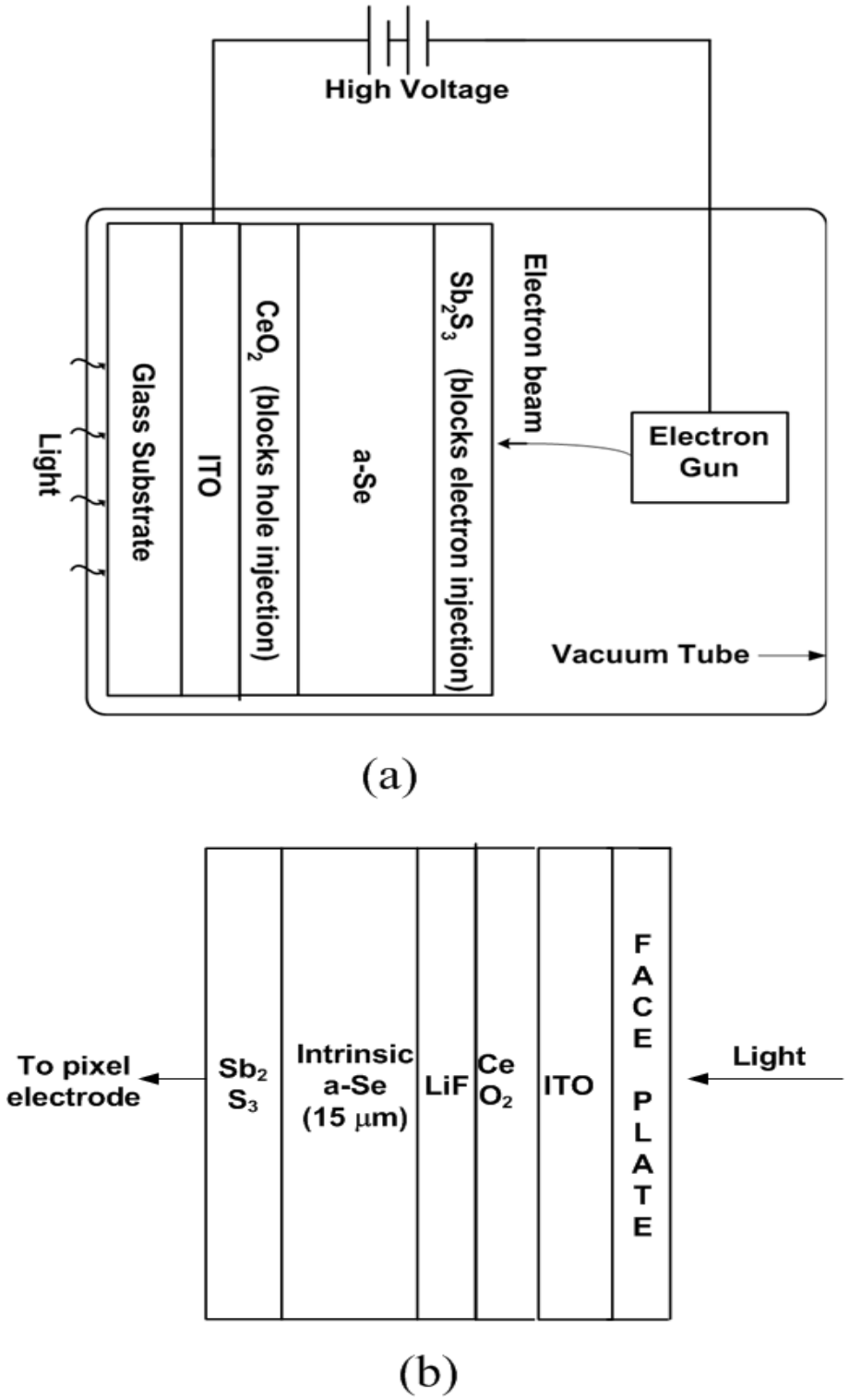

Figure 4.8: (a) Structure of HARP camera whose surface is scanned by electron beam in vacuum; (b) Structure of avalanche a-Se used for our experiment.

the electron beam.

In contrast to the HARP tube design (see Figure 4.8 (a)) which requires vacuum operation for scanning electron beam signal readout, our proposed protein crystallography detector implements a pixellated electrode readout. Here pixel electrodes are used to collect the charge from the avalanche a-Se layer. Al, which is the top metal layer of a-Si:H TFT array, works as the pixel electrode. Since the mobility of holes in a-Se is an order of magnitude higher than that of the electrons, only holes can create new carriers by impact ionization. Hence it is essential for x-ray or optical photons to enter from the positive bias side of the avalanche a-Se structure so that holes can avalanche by impact ionization and be collected by pixel electrodes. So the pixel electrode will work as cathode and the top electrode will work as anode. It is necessary to deposit the electron blocking layer (Sb_2S_3) just on top of the pixel electrode, then deposit a-Se layer, the hole blocking layer (CeO_2, and the top electrode. Thus the sequence of film deposition on top of TFT array is the opposite of the existing HARP film deposition sequence. Reversing the HARP film deposition sequence can change the interface properties of the films, and thus needs to be investigated.

4.2.1 Measurement Results from Avalanche a-Se

For protein crystallography x-ray energy, if a direct detection scheme is used a 100 μm thick a-Se layer is necessary to achieve a reasonable quantum efficiency (shown in Chapter 2). In order to establish avalanche multiplication in such a thick layer of a-Se, application of very high potential ($\sim$ 12 kV) is required which is challenging in our lab setup. Therefore, prototype avalanche a-Se structure of 15 μm thickness is used in our experiment for integration with a-Si:H TFT pixel and proof of concept. The avalanche a-Se layers used in our experiment were supplied by NHK Science and Technical Research Laboratories, Japan Broadcasting Corporation, Japan.

The structure of the a-Se avalanche layer is shown in Figure 4.8 (b). For the first samples, all a-Se layers were made with intrinsic Se (i.e. no As doping), and the samples would recrystallize over time. However, according to NHK engineers, who routinely use intrinsic Se for test samples, there should not be any problem with avalanche phenomenon, and the recrystallization would not happen within at least 2 months. Due to

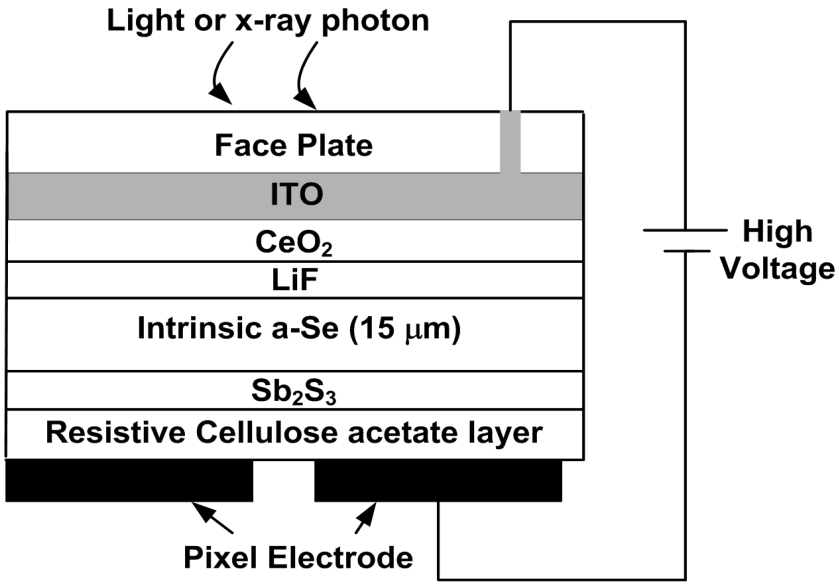

(a)

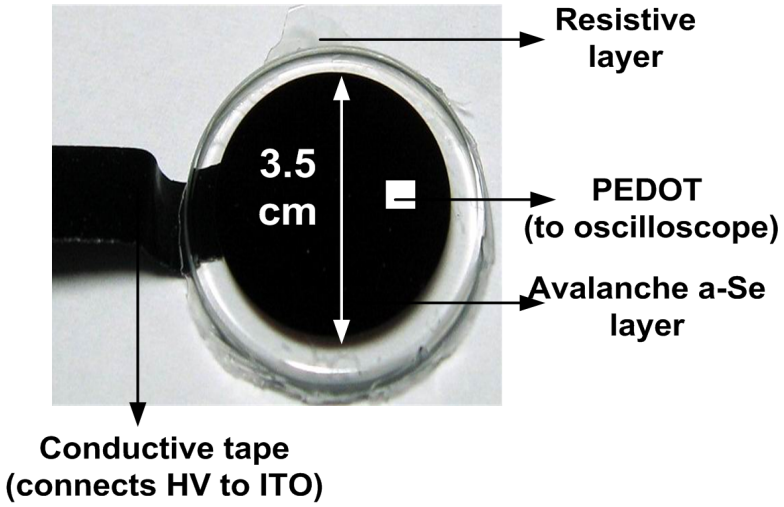

(b)

Figure 4.9: (a) Schematic diagram of avalanche a-Se structure with resistive layer and pixel electrode, (b) Picture of the avalanche a-Se photoconductor used in our experiment.

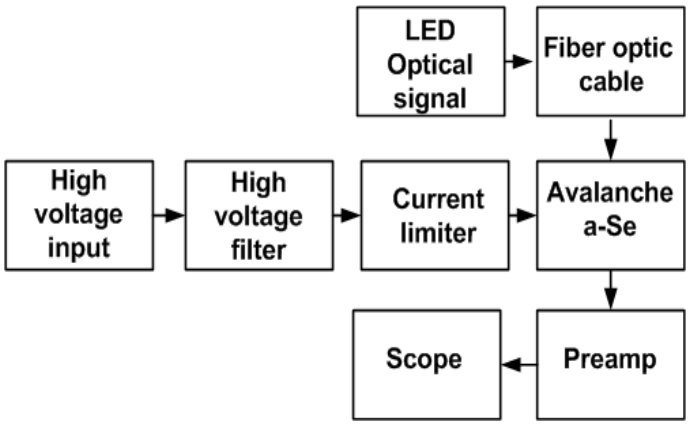

Figure 4.10: Block diagram showing the experimental setup for characterizing avalanche a-Se layer.

recrystallization concern, we performed all our experiments within 60 days of the arrival of the a-Se structures.

It has been found in literature that HARP camera with pixellated structure failed due to improper electrical contact to the device [62]. Our collaborator at Sunnybrook Health Sciences Center Toronto, showed that if pixel electrodes directly deposited on HARP, at avalanche fields they produce Joule heating which crystallizes a-Se layer. Crystalline a-Se layer has lower resistance, and as such dark current increases drastically damaging the device. They overcame this contact problem by introducing a resistive interface layer between a-Se and the pixel electrode. We used the same approach for our experiment and used cellulose acetate as the resistive layer. The resistivity of the layer was measured to be $\sim$ GΩ/cm^2. The thickness of the layer can be designed to have an appropriate resistivity to prevent a-Se breakdown. The other electrode is made from a PEDOT conductive polymer which is "painted" on top of the cellulose acetate resistive layer. It is contacted using a spring-loaded gold-coated pin and this constitutes a single readout path. The PEDOT was painted on $\sim$ 1 mm^2 area. The schematic and picture of the avalanche a-Se structure used in our measurement are shown in Figure 4.9.

The block diagram of the experimental setup for the characterization of the avalanche a-Se photoconductor is shown in Figure 4.10. The avalanche a-Se layer is mounted inside a light-tight box equipped with an optical fiber bundle to bringing the optical signal from the photo-excitation source which is a pulsed blue light emitting diode (LED). High

voltage (HV) is passed through a low pass filter to reduce noise from the power supply, and then through a high resistance to limit the current to a safe value in order to protect the circuit from damage. The ITO layer of avalanche a-Se structure is connected to the high voltage through a conductive tape. The spring-loaded gold-coated pin is connected to the preamplifier which would amplify the output signal before reaching the oscilloscope. We gradually increased the bias voltage across the a-Se layer, and measured the photocurrent using this oscilloscope.

Figure 4.11 (a) shows photocurrent increases gradually with applied electric field due to increase in conversion gain up to $\sim$ 80 V/μm and then avalanche multiplication starts to take place. When electric field is greater than 80 V/μm photocurrent increases dramatically. Figure 4.11 (b) shows that our targeted avalanche gain of 10 can be achieved by applying an electric field of $\sim$ 96 V/μm which matches our calculated value of electric field (97.3 V/μm) for 15 μm thick a-Se layer (see section 2.2.5). The avalanche a-Se structure can sustain the application of high electric field ($F \approx$ 100 V/μm) without breakdown. We measured the dark current for our target which was 30 pA/mm^2 for electric field of 100 V/μm at room temperature. The dark current value is very low and therefore will generate negligible dark current shot noise.

4.3 Development of Parallel Electrode Test Structure

As an initial step of integration of avalanche a-Se with TFT arrays, we mimicked the top metallization layer of TFT by parallel electrode test structure. We designed the electrodes with different thickness and spacings (see Figure 4.12). Cellulose acetate comes in powder form and is soluble in acetone. We prepared 4%, 5% and 9% Cellulose acetate (CA) solution (measured by mass), and applied to the parallel electrode structure. A thin film of CA remains once the acetone evaporates. We measured lateral and transverse resistances for different electrode spacings to check whether the resistive layer causes any unwanted lateral conduction between pixels. We found that lateral leakage current between neighboring pixels is less than 1 pA/pixel under typical operating voltage ensuring no cross talk between pixels.

One critical issue is, as acetone evaporates, it will leave voids or empty spaces behind.

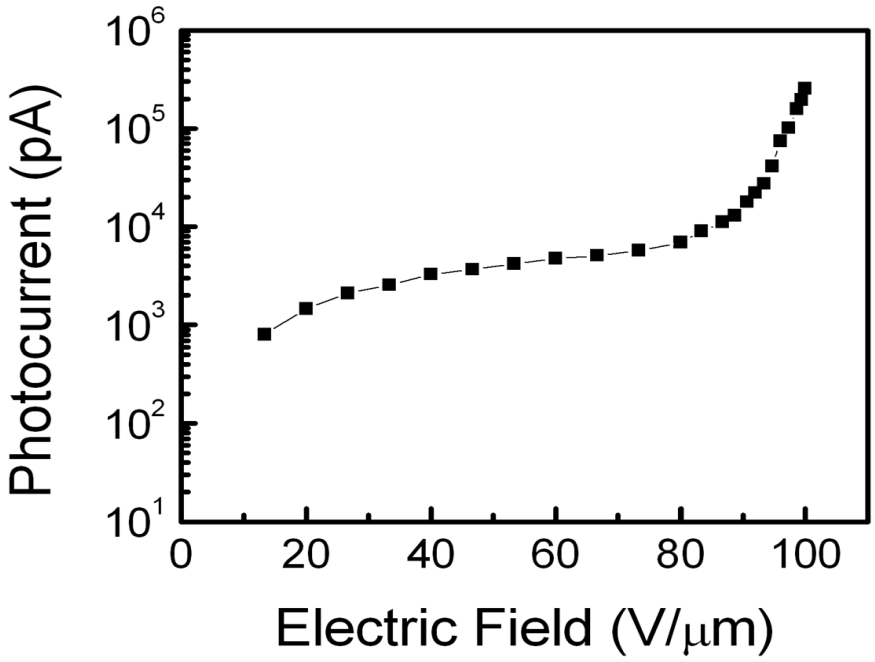

(a)

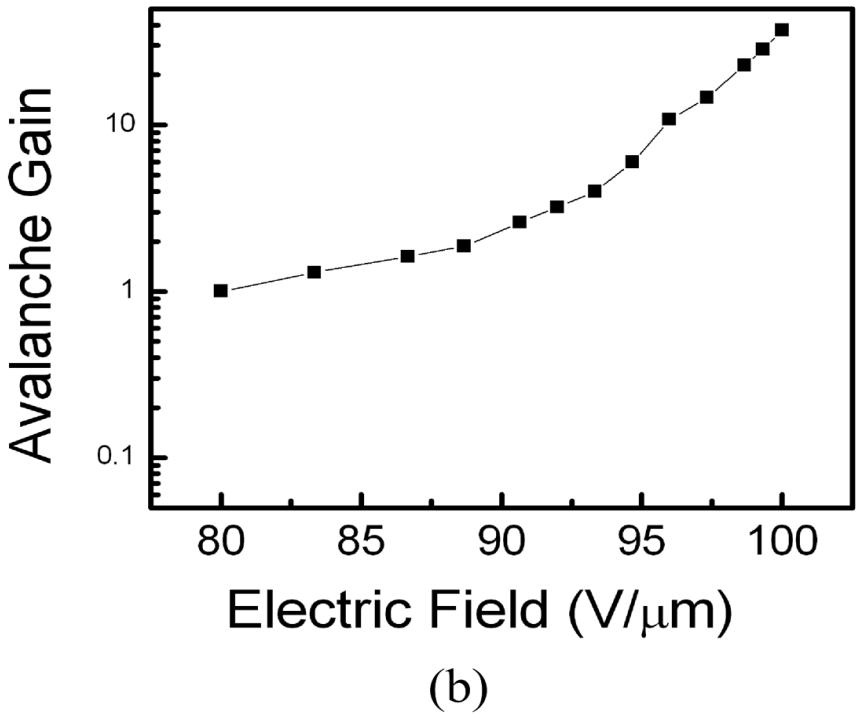

(b)

Figure 4.11: (a) Photocurrent vs applied field, (b) avalanche gain vs applied field for 15 μm thick a-Se layer with PEDOT electrode and 2.5 μm resistive layer.

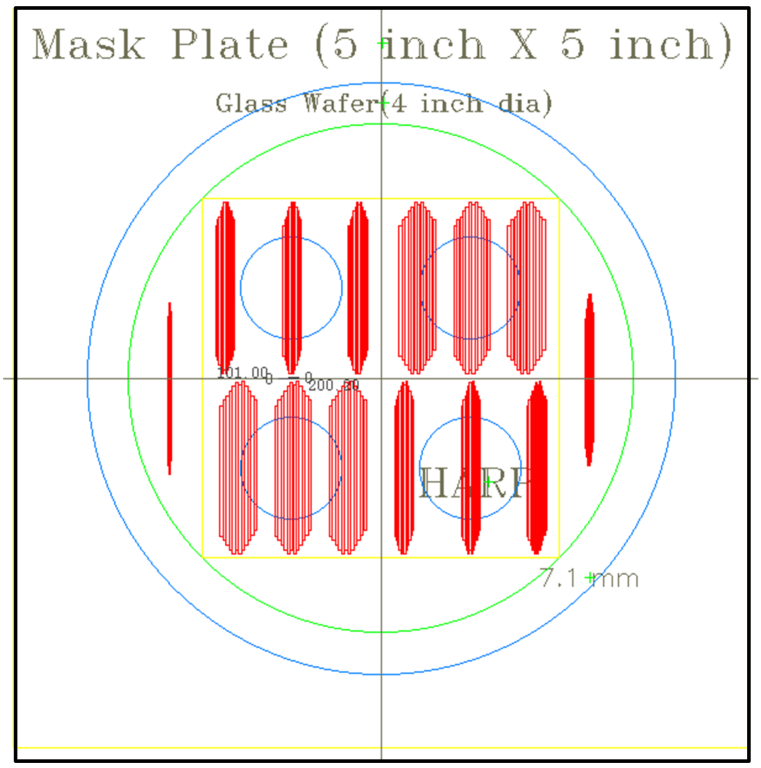

Figure 4.12: Mask layout of the parallel electrode test structure.

This could be a problem for charge transport. In order to get an uniform layer, we need to keep the solution at room temperature and cure slowly. Figure 4.13 (a) shows an image of properly cured CA layer obtained with a microscope.

The CA layer is adhesive, and as such it will bond HARP and a-Si:H TFT array. In order to get CA layer of a certain thickness, we decided to do it in a two step process. First to deposit CA of desired thickness on test structure, and then using an ultra thin layer of CA just for adhesive purposes in a second step. We developed uniform CA layer on test structure. Then we put a thin CA layer on top of it and immediately put the HARP and applied pressure to bond them. We found the CA layer cracked (see Figure 4.13 (d)). Further investigation is required to optimize the CA layer or to find another adhesive material for gluing purpose which does not require any solvent to be removed. In the interim, we carried out experiments to integrate the HARP structure with a single a-Si:H pixel.

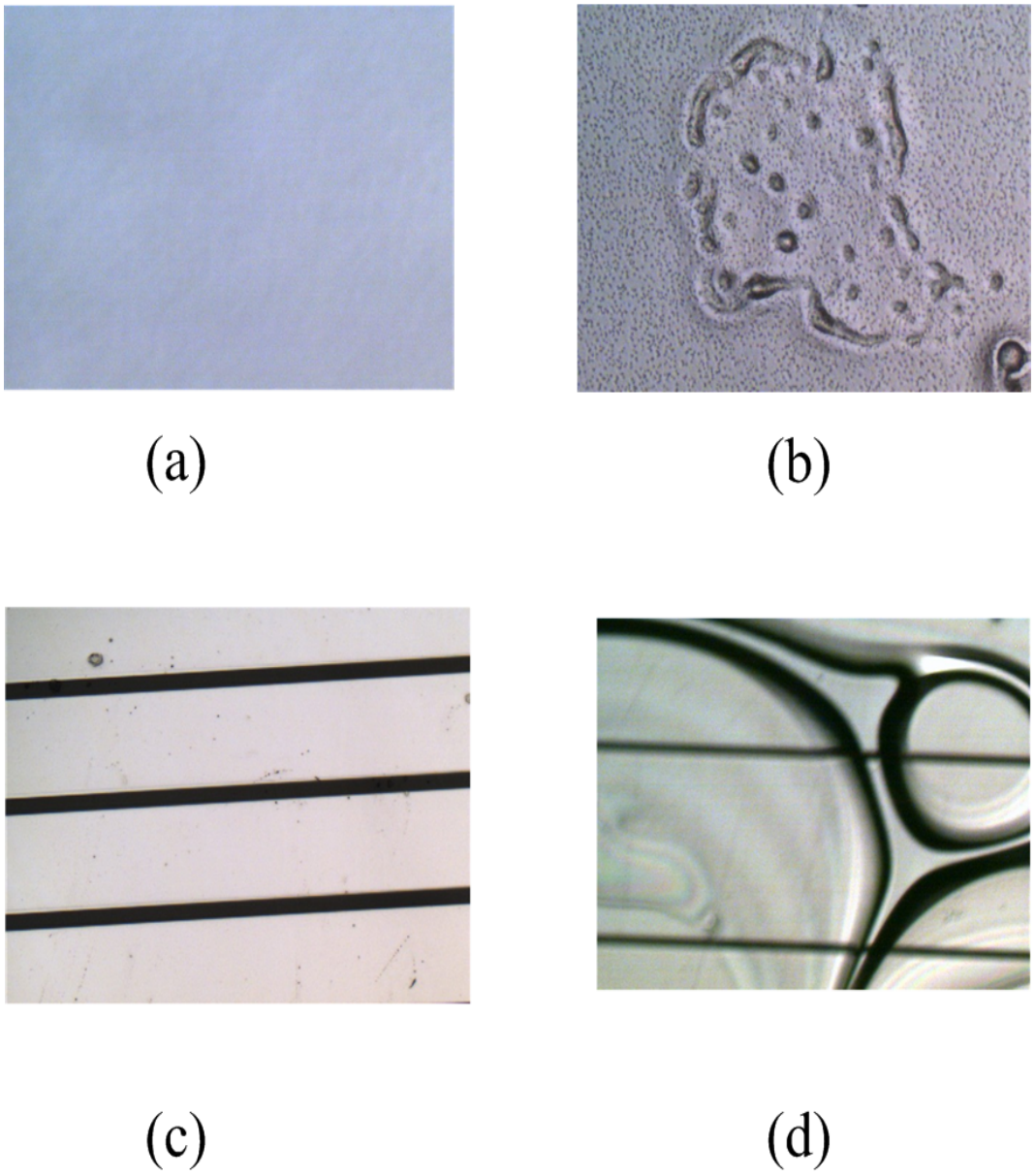

Figure 4.13: (a) Properly cured CA layer, (b) voids in CA layer, (c) CA layer deposited on test structure, (d) cracks in CA layer between test structure and HARP.

4.4 Experimental Results: Single Pixel Readout

We used the same experimental setup described in previous section to integrate the avalanche a-Se with a-Si:H pixel. The pixel has 5 pF storage capacitor and an inverted staggered a-Si:H TFT with with an aspect ratio (W/L) of 54 μm/18 μm. We connected the spring-loaded gold-coated pin of avalanche a-Se structure to the drain of the a-Si:H TFT. We biased the gate of the TFT with a pulse bias and connected the source terminal of the TFT to a preamplifier. The sensitivity of the preamplifier was set to 100 nA/V. The preamplifier was connected to the scope, and we read the output from the scope. Figure 4.14 shows the block diagram and the experimental setup used for single pixel readout. The signal generator was used to provide both gate pulse for the TFT and the driving pulse for the LED. The TFT gate pulse is a 30 Hz bipolar pulse (-5 V to +15 V) with 50% duty cycle.

4.4.1 Measurement of Gain of the Detector

To measure the gain of the detector system, the LED intensity was set to a fixed value, so the input optical signal to the a-Se layer is constant. Only the bias voltage across the avalanche a-Se layer was gradually increased, and the output voltage was measured from the oscilloscope.

Figure 4.15 (a) shows the experimental measurement data. It is clear from the Figure that due to increase in applied bias across the a-Se layer, both increase in conversion gain and avalanche multiplication occurs which causes the amplification of input signal. This increase in input signal is reflected in output voltage and output voltage is amplified from its initial value.

Figure 4.15 (b) shows a snapshot from the oscilloscope during measurement. It is evident from the figure that the TFT transferred the signal to the oscilloscope only when the gate pulse of the TFT is +15 V, that is, the TFT was ON. There is some capacitive coupling between the a-Se and a-Si:H TFT which causes the spikes in output voltage during switching. This is the first time that avalanche a-Se structure was connected to a-Si:H TFT without any breakdown upto 100 V/μm, showing the proof of concept.

Since we performed the experiment with optical signal, we matched the input signal

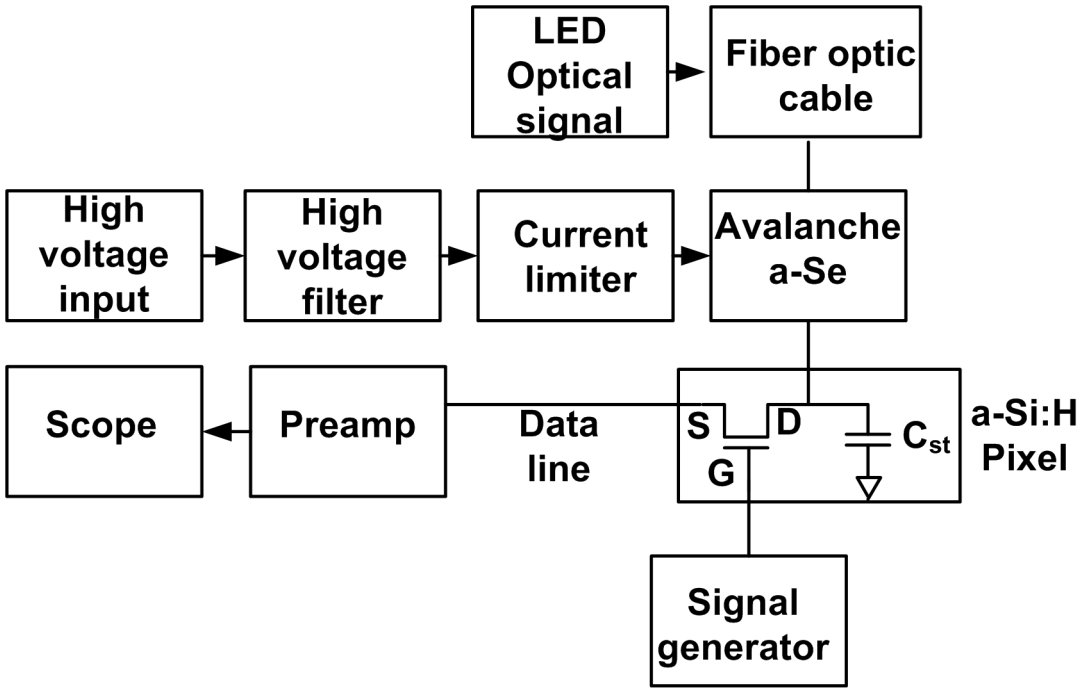

(a)

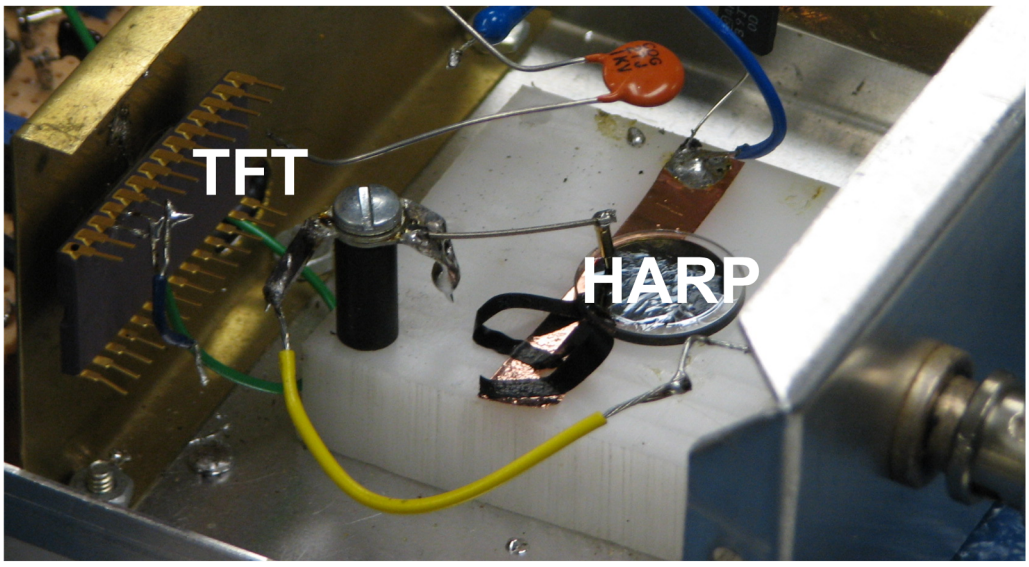

(b)

Figure 4.14: (a) Block diagram showing the experimental setup; (b) picture of the setup used for single pixel readout.

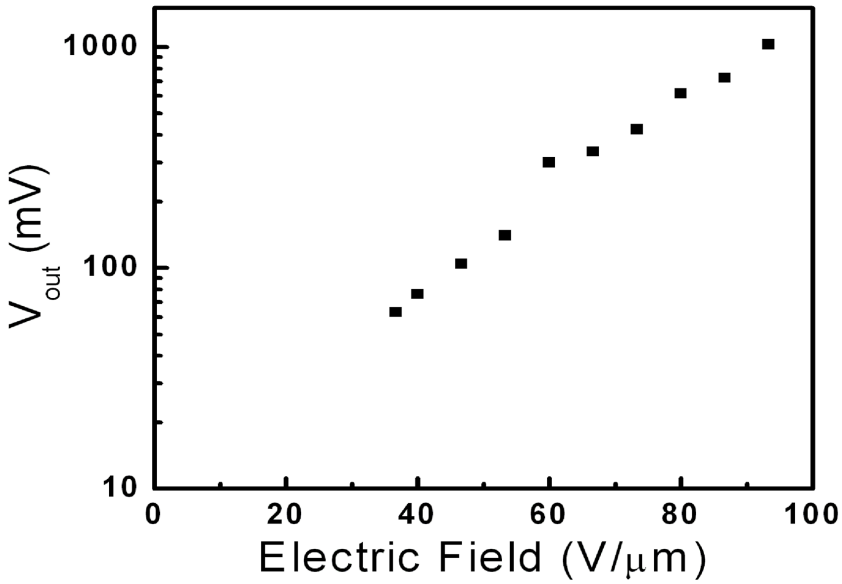

(a)

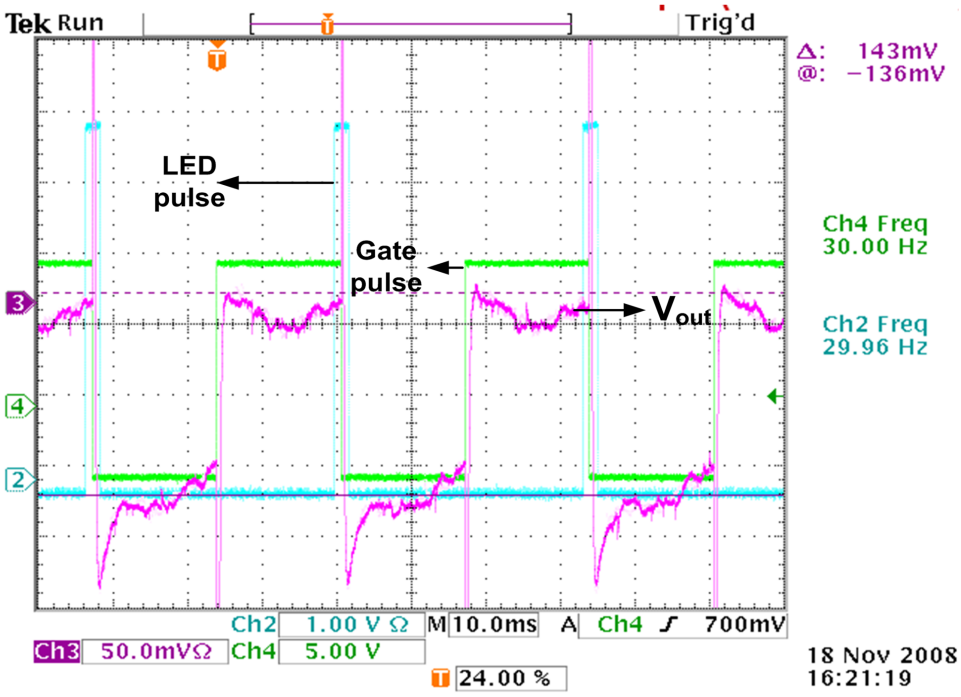

(b)

Figure 4.15: (a) Measured output voltage from single pixel, (b) Snapshot from the scope showing the experimental measurement.

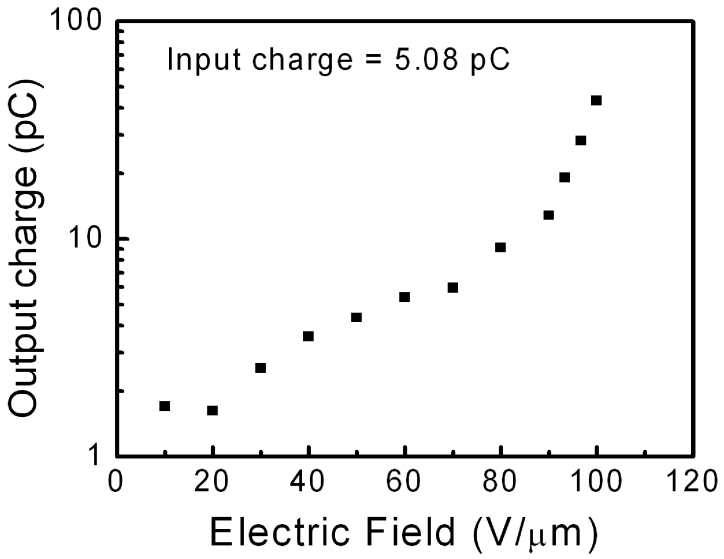

Figure 4.16: Measured output voltage from single pixel at protein crystallography signal level.

to the protein crystallography range to confirm the detector's functionality for the application. The x-ray fluence for protein crystallography home laboratory x-ray source (such as, Rigaku RU-200) is $\sim 2 \times 10^5$ x-rays/mm^2/s at 8 keV. The following method is used to convert optical signal into x-ray photons:

We set the LED intensity to an arbitrary value and biased a-Se layer at 30 V/μm. We measured the photocurrent from a-Se layer (using a ~ 1 mm^2 PEDOT electrode) to be 2.54 nA. The LED pulse duration was 2 ms. Therefore, charge density, Q, (electrons/mm^2) for a single interacting LED pulse is given by:

$$Q = I \times t = 5.08\ pC/mm^2 \tag{4.2}$$

Now, electron density for a single LED pulse:

$$N = Q/e = 3.175 \times 10^7\ electron/mm^2 \tag{4.3}$$

One 8 keV signal generates $\sim$ 240 electrons when a-Se is biased at 30 V/μm (see (2.1)). Therefore, number of 8 keV x-rays/mm^2 can calculated by:

$$\psi = N/240 = 1.3 \times 10^5\ x - rays/mm^2 \tag{4.4}$$

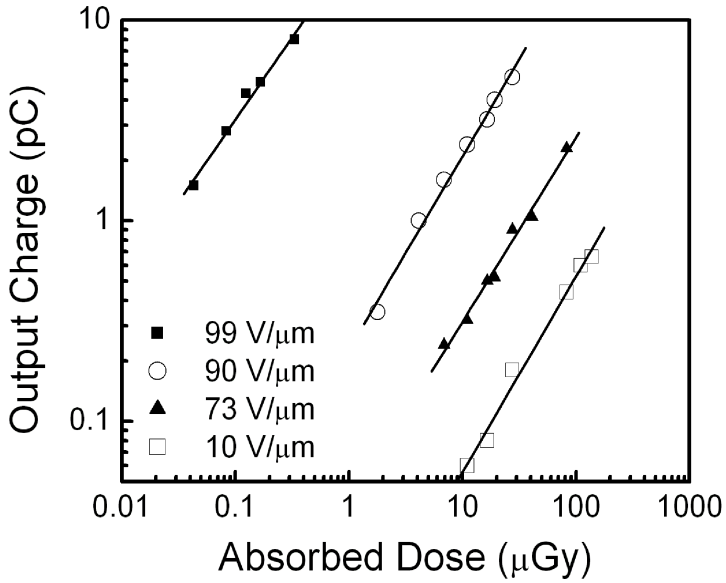

Figure 4.17: Measured output charge vs the input signal showing linear response of the detector.

The LED setting produces an input signal comparable to that generated by rotating a anode x-ray source. We performed another set of measurement at this LED setting. Experimental result (see Figure 4.16) confirmed that the detector can detect signal for protein crystallography range.

4.4.2 Measurement of Linearity of the Detector

To measure the linearity of the detector, the bias voltage across the a-Se layer was set to a fixed value so that the gain of the a-Se layer was constant for one set of measurement. The amplitude of the input LED pulse was varied and corresponding change in output voltage was observed. The LED intensity was measured using a photomultiplier. The output charge versus input signal of the detector is shown in Figure 4.17. The measurement was performed at four different bias voltages. The detector response was linear over the full range.

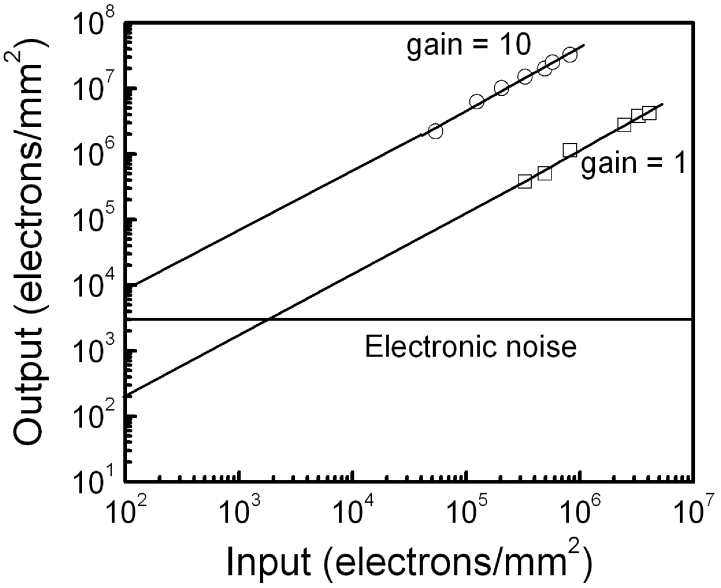

Figure 4.18: Experimental results showing the sensitivity of the detector.

4.4.3 Measurement of Sensitivity of the Detector

In order to measure the sensitivity of the detector, the bias voltage across the a-Se layer was set to two values: 150 V (i.e., F = 10 V/μm) and 1350 V (i.e., 90 V/μ) which corresponds to avalanche gain of 1 and 10 respectively. The input LED signal was gradually varied and the output voltage was measured. Figure 4.18 shows that if there is no avalanche gain (avalanche gain =1), the electronic noise of the detector is higher than the lowest input signal and the detector cannot detect it. However, if the input signal is amplified by an avalanche gain of 10, the detector will be able to detect it ensuring quantum noise limited operation of the detector.

4.5 Summary

We integrated HARP with a-Si:H pixel using a resistive layer (Cellulose Acetate) on top of avalanche structure to avoid breakdown of the device. Measurement results showed that the integrated device can detect single x-ray photon by providing necessary avalanche gain, sustain the application of high electric field (F = 100 V/μm), and respond linearly over the entire operating x-ray range. This is the first time that an avalanche a-Se structure was connected to a-Si:H TFT without any breakdown.

Chapter 5

Performance Features of the Detector

This chapter investigates the performance of the detector under extended pulsed bias stress. The detective quantum efficiency (DQE) of the detector is calculated considering the effect of K-fluorescence reabsorption and avalanche gain.

Our proposed detector for protein crystallography consists of a two dimensional active matrix array of a-Si:H TFTs. a-Si:H TFTs exhibit a metastable shift in their characteristics when subject to prolonged gate or drain bias that results in changes in their threshold voltage (V_T) and a corresponding change in ON resistance (R_{ON}) [63], [46]. If not properly accounted for, the V_T shift can be a major constraint in imaging applications as it introduces a non uniformity in the TFT charge transfer function resulting in fixed pattern noise in the protein crystallography imager. Here we investigated the time-dependent shift in V_T of a-Si:H TFTs stressed with the same bipolar pulsed biases used for static (chest radiography, mammography, and static protein crystallography) and real time imaging modalities (low dose fluoroscopy at 15, 30 and 60 frames/second, and dynamic protein crystallography).

5.1 Metastability of a-Si:H TFT under Pulse Bias Stress

a-Si:H TFTs experience device characteristics degradation when subject to prolonged gate bias that results in a change in threshold voltage (V_T), and a corresponding change in TFT ON resistance (R_{ON}) [42]. Metastability investigations have often concentrated on applying DC voltage to the TFT gate [64], [63], though TFTs are driven by bipolar pulse voltage during practical imaging applications. In particular, realtime operation (33 frames/s) is necessary for time-resolved protein crystallography experiments where the kinetics of the reaction and the conformational changes exhibited by the protein molecule is investigated. In order to determine the lifetime and stability of imaging arrays, it is necessary to predict the amount of V_T shift ($\triangle V_T$) the TFT may encounter over an entire operating period under bipolar pulse bias operation. In this section, first we theoretically estimate the $\triangle V_T$ caused by pulse bias stress for 10,000 hours of operation. Then we verified the calculation by experimental measurements.

5.1.1 Theoretical Models of $\triangle V_T$

So far, two instability mechanisms have been reported in the literature to account for $\triangle V_T$ of TFT. The first mechanism is charge trapping in the TFT gate dielectric (a-SiN$_x$:H) of the TFT and the second mechanism is defect state creation in the a-Si:H layer or at the a-Si:H/a-SiN$_x$:H interface [65], [66]. Defect creation dominates at lower gate bias voltages (e.g., <25 V) whereas charge trapping in the gate dielectric becomes significant at higher gate voltages [42], [65], [41]. Defect state creation is related to creation of silicon dangling bonds by breaking weak silicon-silicon bonds and is strongly dependent on the quality of a-Si:H films. Charge trapping is largely influenced by the quality of the gate nitride, in particular the number of trap sites at or near the a-Si:H/a-SiN$_x$:H interface.

The threshold voltage shift due to the charge trapping in the gate dielectric shows a logarithmic time dependence and very small temperature dependence [42]:

$$\triangle V_T \sim r_d \log(1 + \frac{t}{t_0}). \tag{5.1}$$

Here t_0 is temperature dependent parameter, r$_d$ is a constant which depends on the density of traps, N_t [cm^{-3}] and it is independent of temperature, and t is the bias stress time duration.

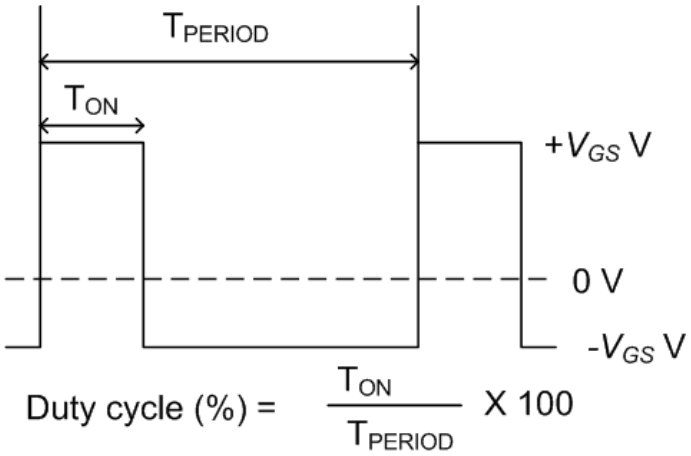

Figure 5.1: Waveform of a bipolar pulse showing duty cycle.

When a positive gate bias (< 25 V) is applied to the TFT, electrons accumulate and form a channel at the a-SiN$_x$:H /a-Si:H interface where they predominantly reside in conduction band tail states. These tail states have been identified as weak silicon-silicon bonds which, when occupied by electrons, can break to form silicon dangling bonds (deep-state defects) [66]. Deep-state defect creation forms the basis of the defect pool model [67], where the rate of defect creation is a function of the barrier to defect formation, the number of electrons in the tail states, and the density of the weak bond sites. It has been proposed that deep-state defect creation is characterized by power law time dependence and is strongly affected by temperature [42]. For the defect state creation mechanism in a uniform a-Si:H TFT channel, $\triangle V_T$ can be expressed as [42], [66]:

$$\triangle V_T(t) = A(V_{GS} - V_{Ti})^{\alpha}(t)^{\beta}. \tag{5.2}$$

Here A, α, β are temperature-dependent parameters, V_{GS} is the gate bias voltage, V_{Ti} is the V_T of the TFT before bias stress is applied, and t is the bias stress time duration.

A pulse bias is defined by its frequency and duty cycle where duty cycle is defined as the ratio of ON time and period of the pulse bias (see Figure 5.1). $\triangle V_T$ has been shown to be independent of pulse frequency for positive pulse bias [63], [68]. The only effect of pulse bias is that the bias stress time changes depending on its duty cycle. A smaller duty cycle means a smaller effective stress time, so it causes a smaller $\triangle V_T$ for every period of the pulse and this will accumulate for the entire stress time. Thus $\triangle V_T$

for positive pulse bias can be expressed as [63]:

$$\triangle V_T^+(t) = A(V_{GS} - V_{Ti})^{\alpha 1}(\frac{T_{ON}}{T_{PERIOD}}t)^{\beta 1}. \tag{5.3}$$

$\triangle V_T$ induced by negative pulse bias is significantly smaller than DC negative bias and it is strongly dependent on both the frequency and duty cycle of the pulse. The dependence of $\triangle V_T$ on duty cycle can be attributed to the reduction in effective stress time. The frequency i.e. pulse width dependence of $\triangle V_T$ under negative pulse bias has been explained by effective carrier model which correlates the $\triangle V_T$ to the effective hole concentration accumulated near the a-Si:H/a-SiN$_x$:H interface during negative pulse bias [63]. Assuming that $\triangle V_T$ during the negative pulse bias is proportional to the effective carrier concentration, the pulse width dependence is expressed as [63]:

$$FPW = [1 - \frac{\tau_h}{T_{ON}} + \frac{\tau_h}{T_{ON}} \exp(-\frac{T_{ON}}{\tau_h})]. \tag{5.4}$$

Here, τ_h is the effective hole accumulation time constant of the a-Si:H TFT. Considering pulse width and duty cycle dependence, $\triangle V_T$ for negative pulse bias can be expressed as [63]:

$$\triangle V_T^-(t) = FPW \times B(V_{GS} - V_{Ti})^{\alpha 2}((1 - \frac{T_{ON}}{T_{PERIOD}})t)^{\beta 2}. \tag{5.5}$$

Bipolar pulse bias has alternative positive and negative amplitudes. $\triangle V_T$ induced by a bipolar pulse is approximately equal to the $\triangle V_T$ value obtained by simply adding up the $\triangle V_T$ for solely positive and solely negative pulse bias. So $\triangle V_T$ for a bipolar pulse can be estimated from:

$$\triangle V_T(t) = \triangle V_T^+(t) + \triangle V_T^-(t). \tag{5.6}$$

5.1.2 Estimation of $\triangle V_T$ and $\triangle R_{ON}$

Our proposed detector is an array of pixels where each pixel consists of a pixel electrode to collect the charge generated by the x-ray photoconductor layer, a storage capacitor for holding the charge before the readout, and an a-Si:H TFT switch for controlling the charge transfer. This pixel structure is known as passive pixel sensor (PPS). In the two-dimensional a-Si:H TFT array, pixels are selected row by row by means of a bipolar gate

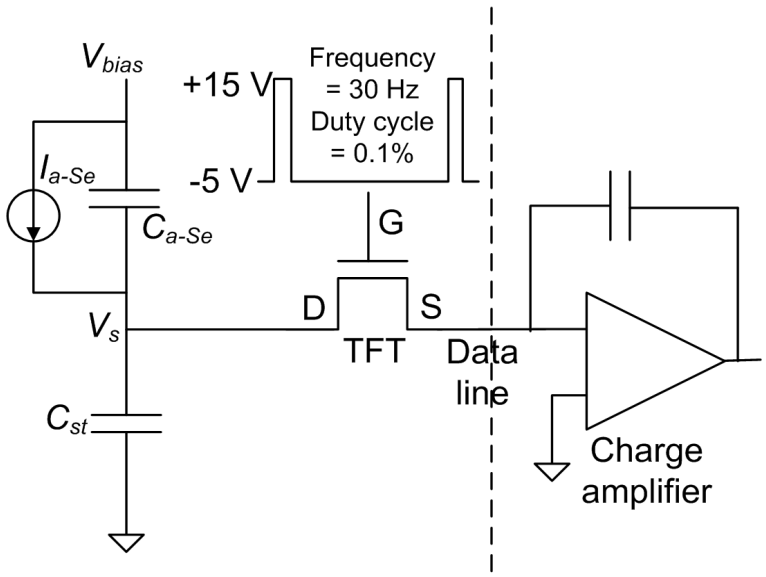

Figure 5.2: Equivalent circuit of a passive pixel sensor showing the pulse bias at TFT gate.

pulse. For real time operation of a 1000 by 1000 x-ray imaging array, the gate signal clock frequency is 30 Hz (T_{PERIOD} is 33.$\dot{3}$ ms), and during readout a row of TFTs is turned ON only for 33 μs (T_{ON} is 33 μs) while the TFT is turned OFF for the rest of the period.

Figure 5.2 shows the schematic diagram of the PPS circuit. Here V_{bias} is the bias voltage applied across the a-Se layer, C_{st} is the storage capacitor, C_{a-Se} is the capacitance of the a-Se layer for each pixel, and I_{a-Se} represents the signal at each pixel. The total capacitance per pixel, C_P, is the sum of C_{st} ($\sim$ 5 pF) and C_{a-Se} ($\sim$ 10 fF). Since C_{a-Se} is much smaller than C_{st}, it is assumed that C_P is equal to C_{st}. The data line is connected to a column charge amplifier to convert the accumulated signal on the charge detection node, V_S, into a stable voltage.

When the TFT is ON, the stored charge in C_P is discharged to the data line by an a-Si:H TFT with a time constant, τ_{ON}. τ_{ON} is the product of the ON resistance R_{ON} of the switching TFT and the pixel capacitance C_P. Since the source of the TFT is connected to virtual ground during readout, the a-Si:H TFT is operated in the linear region ($V_{DS} \ll V_{GS}$-V_T), and R_{ON} can be expressed as previously noted in (4.1):

$$R_{ON} = [\frac{W}{L}\mu_{eff}C_G(V_{GS} - V_T)]^{-1}. \tag{5.7}$$

From (5.7), it is clear that if the bipolar pulse bias stress causes any change in V_T, it will be

Table 5.1: Value of different parameters used for calculation of $\triangle V_T$ and R_{ON}.

Parameter	Value (used in this work)	Value (from literature)
A	0.00115	0.0038 [41]
$\alpha 1$	1	1 [42], 1.9 [63], 1 [41]
$\beta 1$	0.31	0.25 [41], 0.3 [46], 0.5 [63]
B	0.00012	NA
$\alpha 2$	2.3	2.4 [63]
$\beta 2$	0.25	0.32 [63], 0.25 [69]
τ_h	13 ms	NA
μ_{eff}	0.5 cm^2/V-s	NA
C_G	25 nF/cm^2	NA
T_{ON}, T_{PERIOD}	33 μs, 33.$\dot{3}$ ms	NA
V_{ST}, V_{Ti}	15 V and -5 V, 3.7 V	NA

reflected as change in R_{ON}. The change in R_{ON} ($\triangle R_{ON}$) may not be the same for every TFT in the array. As a result, the TFTs over the array may have non uniform $\triangle R_{ON}$ thus generating fixed pattern noise. On the other hand, when the TFT is OFF a small leakage current (in the order of fA) flows from TFT drain to source. This leakage current decreases the charge on C_{st}. The lower the leakage current, the better the performance of the PPS. Again, the forward subthreshold slope describes the sensitivity of the TFT current to the gate bias during the turn on process. A smaller subthreshold slope is preferable since it implies that the TFT requires less voltage for transition from the OFF to ON state. So the effects of pulse bias stress on TFT leakage current and subthreshold slope are critical and also should be investigated.

We calculated $\triangle V_T$ and $\triangle R_{ON}$ of a-Si:H TFTs with W/L of 84 μm/18 μm stressed with a bipolar pulse bias of 0.1% duty cycle at 30 Hz frequency. As such, the gate of the TFT is stressed with +15 V for only 33 μs, and -5 V for the rest of the period. Since the operating voltage is less than 25 V for operation, (5.6) can be used to estimate time

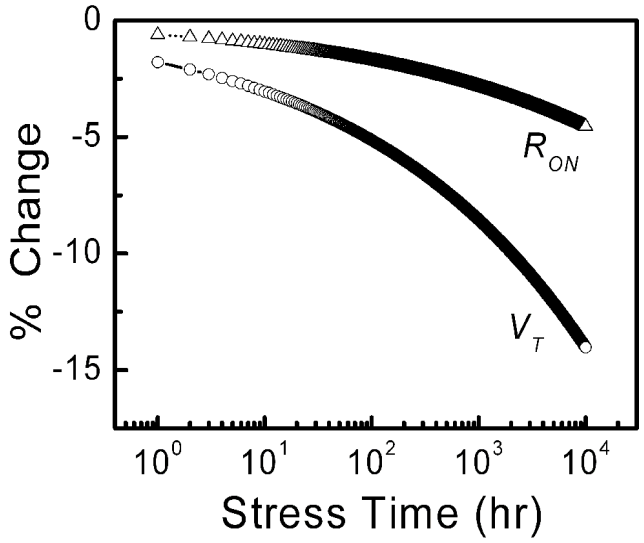

Figure 5.3: percentage change in V_T and R_{ON} as a function of time up to a total of 10,000 hrs of bipolar pulse stress.

dependent $\triangle V_T$. The values of A, $\alpha 1$, $\beta 1$, τ_h, B, $\alpha 2$ and $\beta 2$ in (5.3), (5.4) and (5.5) have been taken from the literature or extracted from experimental data and are given in Table 5.1.

Figure 5.3 shows the percentage change in V_T and R_{ON} for 10,000 hrs of bipolar pulse stress applied to the gate of TFT. Since the TFT is stressed most of the time with negative bias voltage, V_T decreases by $\sim 15\%$, R_{ON} decreases by $\sim 5\%$.

5.1.3 Experimental Results

We used a-Si:H TFTs with W/L of 84 μm/18 μm for pulsed bias experiment. The TFTs were annealed at 180°C for 3 hours and then cooled by keeping at room temperature for $\sim$ 10 hours before each stress measurement. During stressing, a 30 Hz bipolar pulse (+15 V/-5 V) bias with 0.1% duty cycle was applied to the gate, while the drain and source of the TFT were connected to ground. After 24 hrs, a rapid gate voltage sweep was done to measure the transfer characteristics (I_{DS}-V_{GS}) of the TFT. During this sweep the drain was kept at 0.1 V to ensure linear TFT operation and the gate voltage was varied from -3 V to 10 V with a step size of 1 V. All these sweep measurements were done with an Agilent 4156 semiconductor parameter analyzer. Following each sweep, the TFT was

put back to pulse bias stress and the sequence was repeated for 150 hours. After each 150 hrs stress test, the TFT was annealed to restore the initial device characteristics within 5% of the pre-stress values.

Figure 5.4 (a) shows the effect of bipolar pulse bias stress (with both drain and source grounded) on the transfer characteristics. The initial V_T, V_{Ti}, is 3.7 V extracted by linear extrapolation of the transfer curve. As shown in the figure, the transfer characteristics curve shifts left with stress times which implies that V_T decreases over time. $\triangle V_T$ due to bipolar pulse bias stress is extracted from the transfer characteristics for different stress times. Since the TFT was stressed under negative voltage most of the time, $\triangle V_T$ is negative. We took the absolute value of $\triangle V_T$ and plotted in log-log scale in Figure 5.4(b) where the solid line shows $\triangle V_T$ calculated using (5.6) and the parameters given in Table 5.1. Measurement results show good agreement with calculated values (see Fig. 5.4 (b)).

The subthreshold region of the TFT is the linear region of the semi-logarithmic transfer characteristic, and the subthreshold slope (S) is the inverse of the slope of that line. Figure 5.5 shows the effect of bipolar pulse bias stress on the subthreshold slope and OFF current of the TFT. From Figure 5.5 it can be seen that, although the TFT OFF current decreases, S does not change much over stress times of up to 150 hrs.

5.1.4 Discussion

When a bipolar gate bias stress is applied to an a-Si:H TFT, both instability mechanisms (charge trapping and defect state creation) occur simultaneously [68]. According to the defect pool model, the dangling-bond states created by the positive bias stress are located below the mid gap of a-Si:H and so do not effect the subthreshold behavior of an n-channel TFT, while those created by the negative bias stress are located near the conduction band and strongly effect the subthreshold slope [67], [68]. The defect states located in the lower part of band gap are known as D_e states (formed under electron accumulation) and cause positive $\triangle V_T$ while those located in the upper part of band gap are known as D_h states (formed under hole accumulation) and cause negative $\triangle V_T$.

Charge trapping leads to a positive $\triangle V_T$ for positive bias and negative $\triangle V_T$ for negative bias, but it does not change the subthreshold slope of the TFT. During the positive pulse ($V_{GS} = 15$ V) charge trapping occurs in the a-SiN$_x$:H gate dielectric and/or

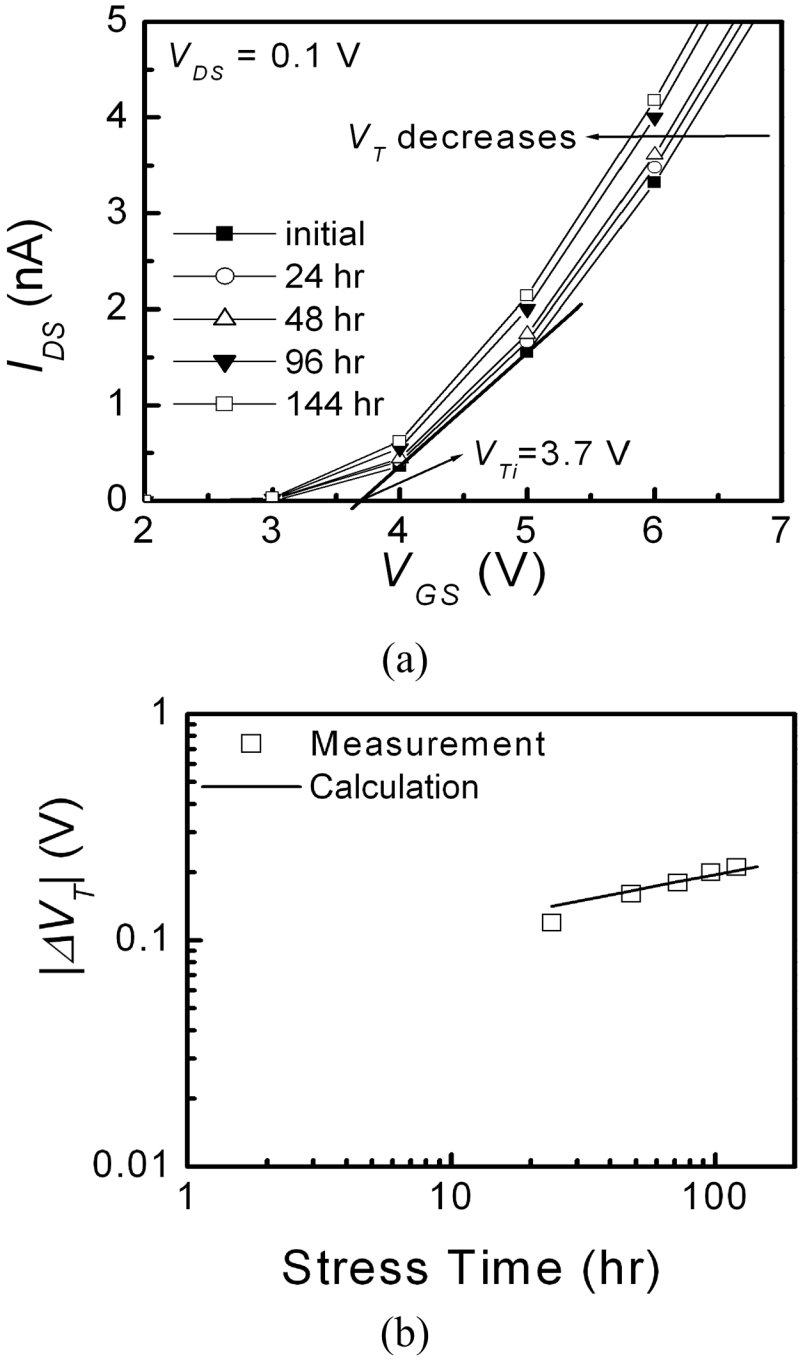

Figure 5.4: (a) Shift in I_{DS}-V_{GS} curve of the TFT due to bipolar (15 V/-5 V) pulse bias stress for different stress times; (b) $|\triangle V_T|$ as a function of stress time (log-log scale); symbol: measurement data, solid line: calculation using (5.6).

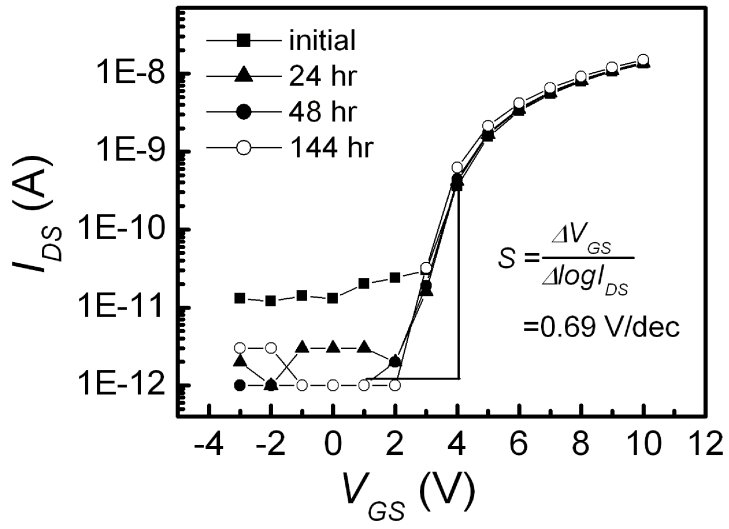

Figure 5.5: log I_{DS}- V_{GS} curve of the TFT due to bipolar pulse bias stress for different stress times showing the subthreshold slope and OFF current of TFT.

at the a-Si:H/a-SiN$_x$:H interface:

$$Si + e^- \longrightarrow Si^-. \tag{5.8}$$

During the negative pulse (V_{GS} =-5 V) charge neutralization occurs in the a-SiN$_x$:H gate dielectric and/or at the a-Si:H/a-SiN$_x$:H interface:

$$Si^- + h^+ \longrightarrow Si. \tag{5.9}$$

For our experiment, the duty cycle was 0.1%. So the effective stress time of positive bias is only 0.1% compared to that of negative bias. As a result, the negative bias has the dominant effect and the overall $\triangle V_T$ is negative (see Figure 5.4 (b)).

Since the TFT is used as a switch in PPS, $\triangle V_T$ is generally not thought to be a serious concern since long readout times ($\sim$ 10 τ_{ON}) can compensate for any variations in transferred charge over time. It is shown that bipolar pulse bias stress can cause variation in V_T and R_{ON} of the TFT over the array. This variation can generate additional spatial noise and can degrade the overall performance of the imager. In order to improve the performance, the exposed dose has to be increased which can cause degradation of protein crystal. Therefore, these additional noise mandates the use of offset-and-gain

compensation techniques in the software for proper operation of the AMFPIs for protein crystallography applications. To date, $\triangle V_T$ due to bipolar pulse stress has been reported in literature only up to stress times of 10^5 seconds (28 hrs) [68]. Our experimental results showed that $\triangle V_T$ of TFT under bipolar pulse bias of 150 hrs is still within allowable range for normal AMFPI operation. Since our experimental result matches with our calculated $\triangle V_T$ using (5.6), the theoretical model presented here can predict the performance of the detector for life time operation.

5.2 Dependence of Avalanche Gain on a-Se Thickness

Avalanche gain, g_{av}, in a-Se can be expressed as:

$$g_{av} = \exp(\gamma_p d_{Se}) \tag{5.10}$$

The field dependence of the hole impact ionization coefficient, γ_p, is given by:

$$\gamma_p(F) = \gamma_{p_1} \exp(-\frac{\gamma_{p_2}}{F}). \tag{5.11}$$

Here γ_{p_1} (= 5.5 $\times$ 10^3 /μm) and γ_{p_2} (= 1.029 $\times$ 10^3 V/μm) are empirical parameters and their values are extracted from experimental data [20]. Substituting the value of γ_p in (5.10),

$$g_{av} = \exp(\gamma_{p_1} \exp(-\frac{\gamma_{p_2}}{F}) d_{Se}) \tag{5.12}$$

Electric field, F, can be expressed as V_{bias}/d_{Se}, so we get:

$$g_{av} = \exp(\gamma_{p_1} \exp(-\frac{\gamma_{p_2} d_{Se}}{V_{bias}}) d_{Se}) \tag{5.13}$$

It is clear from (5.13) that avalanche gain is very dependent on the thickness of the a-Se layer. A non-uniformity in the thickness of a-Se layer results in a variation in F and hence a spatial non-uniformity in gain. Therefore, an important issue for making a large area avalanche a-Se structure is its thickness uniformity. Currently HARP films can be made very uniform for an area of 5 cm^2 with essentially no visible gain variation in the images. As a result, the images currently produced by HARP for broadcast applications do not require any gain uniformity correction [20].

Large area regular a-Se films have already been developed for direct flat panel imagers, however the uniformity requirement for the avalanche a-Se structure is much higher. In

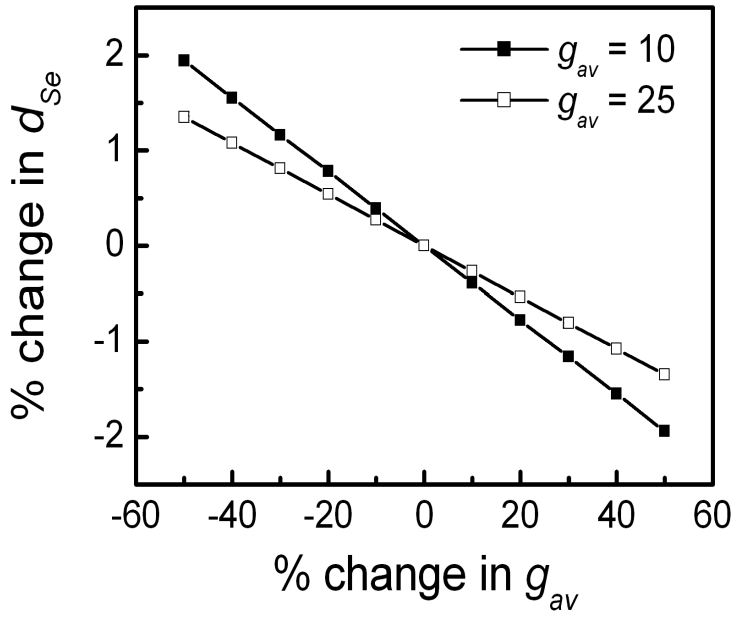

Figure 5.6: Percentage change in avalanche gain (g_{av}) as a function of percentage change in a-Se thickness (d_{Se}).

this section we derive the sensitivity of avalanche gain on a-Se thickness to find how much thickness non-uniformity is tolerable without compromising the gain performance of a large area avalanche a-Se layer for our detector.

To determine the avalanche gain sensitivity to d_{Se}, we take the derivative of (5.13) with respect to d_{Se} and rearrange:

$$\frac{\delta g_{av}}{\delta d_{Se}} = [\frac{\ln(g_{av})}{d_{Se}} - \frac{\gamma_{p_2}\ln(g_{av})}{V_{bias}}]g_{av}$$

or,

$$\frac{\delta g_{av}}{g_{av}} = \ln(g_{av})[\frac{1}{d_Se} - \frac{\gamma_{p_2}}{V_{bias}}]\delta d_{Se}$$

or,

$$\frac{\delta g_{av}}{g_{av}} = \ln(g_{av})[1 - \frac{\gamma_{p_2}}{F}]\frac{\delta d_{Se}}{d_{Se}}. \tag{5.14}$$

The typical value of γ_{p_2} is 1000 V/μm [20] and the typical operating field is 100 V/μm. Since $\gamma_{p_2} > F$, (5.14) shows that a positive change in d_{Se} results in a negative change in g_{av}. Using (5.13), and the values for γ_{p_1} and γ_{p_2} mentioned before, we calculate the percentage change in g_{av} for both positive and negative change in d_{Se} around 100 μm (the necessary thickness of a-Se layer for protein crystallography) for programmed g_{av} values

of 10 and 25. The percentage change in avalanche gain (g_{av}) as a function of percentage change in a-Se thickness (d_{Se}) is plotted in Figure 5.6. The figure shows that for higher initial setting of g_{av}, more change in gain occurs from the same thickness non-uniformity. The fractional changes in g_{av} due to a 1% change in d_{Se} are 25%, and 37%, respectively, for g_{av} of 10 and 25. This range of g_{av} non-uniformity is perhaps within the capability of gain correction and the dynamic range of the electronic circuits of the existing flat panel imagers [20]. However, if the fractional change in d_{Se} is significantly greater than this it may be difficult or impossible to correct adequately by use of a gain correction algorithm.

5.3 Detective Quantum Efficiency

We have proposed and demonstrated the use of an integrating mode x-ray pixel with avalanche a-Se and a-Si:H TFT for image charge readout in order to record x-ray diffraction patterns from protein crystals. The overall imaging performance of such an imaging detector depends on a number of detector parameters. The effect of the detector on measurement noise is expressed by the detective quantum efficiency (DQE), defined as the square of the ratio of the output signal-to-noise ratio (SNR) to that of the input [70]. For an ideal (noiseless) detector the DQE is 1 whereas for practical detectors the DQE is < 1. The DQE can be thought of as the fraction of incident photons effectively recorded by the detector. So a detector with a DQE of 0.1 will require either an integration period ten times longer or an x-ray exposure ten times higher than would an ideal detector to collect data to the same statistical accuracy. For crystallographic applications, x-ray film has a DQE considerably less than 0.1 for typical values of incident photons.

Each detected x-ray photon generates a signal which propagates through the detector system in a cascade process, resulting in a signal at the output. The DQE can be calculated by considering the gain (or efficiency), noise and statistical behavior of each of the stages. The propagation of signal (ϕ) is described in the form of the mean number of quanta per unit area, and noise (S) is in the form of noise power spectrum (NPS). If noise is expressed as the statistical variance in a number of uncorrelated quanta in a specified area, it cannot properly estimate the noise from real image data because it neglects the influence of spatial correlations in the noise [71]. To overcome this, second-order statistical correlations are incorporated in the noise expression by specification of

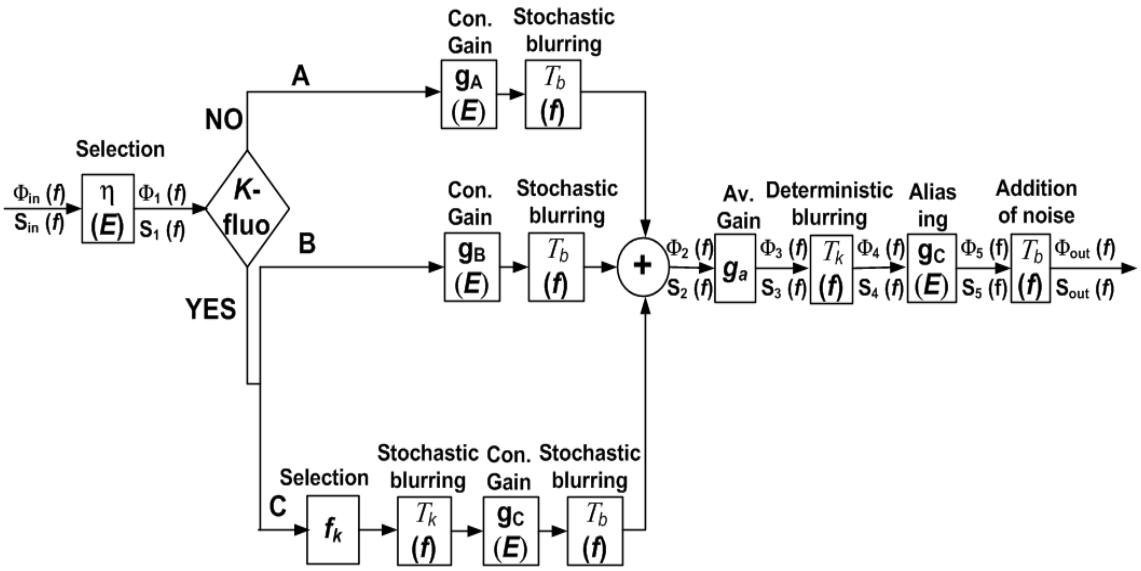

Figure 5.7: Block diagram of our detector showing the flow of signal and noise from input to the output of the system through serial and parallel cascade stages.

the mean and the autocovariance of the noise process. By adoption of the Fourier-based notation of the linear-systems approach, noise in a uniform image is described in terms of the noise power spectrum (NPS).

The signal and noise propagation are described for the total x-ray energy range for protein crystallography, from which the results for monoenergetic x-rays can easily be derived. This approach has proven to be a useful tool in predicting and optimizing the DQE(f) of x-ray imaging systems [72]. Here we develop a linear system model for direct detection avalanche a-Se based imaging system using the parallel cascaded approach, and investigated the effects of K-fluorescence and avalanche gain on the DQE (f) [71].

Figure 5.7 shows the propagation of signal and noise through the detector using the parallel cascaded linear system consists of the following stages:

i) x-ray attenuation by a-Se: depending on the probability of K-fluorescence, three parallel processes can occur independently of the rest of the x-ray interactions. Each of the parallel path has two common stages:

a) gain stage associated with conversion of x-rays to ehps in a-Se, and b) stochastic blurring due to a-Se;

ii) avalanche gain of the avalanche a-Se layer;

iii) the pixel aperture function of the readout;

iv) aliasing due to sampling;

v) addition of electronic noise due to the TFTs and the charge amplifiers.

Before x-rays enter the detector, the x-rays have an energy spectrum $\phi_{in}(E)$ and a maximum photon energy E_{max} . The mean input x-ray photons per unit area $\overline{\phi_{in}}$ can be calculated by integrating over the entire x-ray energy spectrum, and obtain a spatially white input signal spectrum $\phi_{in}(f)$:

$$\phi_{in}(f) = \overline{\phi_{in}} = \int_0^{E_{max}} \phi_{in}(E)dE. \tag{5.15}$$

The input noise is the x-ray quantum noise, results from the randomness in the detection of a finite number of x-ray photons. X-ray quantum noise has a spatially white spectrum and follows the Poisson distribution. The noise power spectrum $S_{in}(f)$ at the input to the detector is given by:

$$S_{in}(f) = \overline{\phi_{in}}. \tag{5.16}$$

We determined the mean number of quanta per unit area $\overline{\phi_i}$, the signal spectrum $\phi_i(f)$, and the noise power spectrum $S_i(f)$ at each of the stages of the detector as shown in Figure 5.7.

5.3.1 X-ray Attenuation by a-Se

The interaction of incident x-ray quanta with a-Se layer is a binary selection process which is a special case of an amplification stage. The energy dependent x-ray quantum efficiency, $\eta(E)$, of a-Se can be calculated using:

$$\eta(E) = 1 - \exp(-\alpha(E)d_{Se}). \tag{5.17}$$

where $\alpha(E)$ is the linear attenuation coefficient and d_{Se} is the thickness of the a-Se layer. The quantum efficiency, $\eta(E)$, of 100 μm thick a-Se layer is plotted as a function of x-ray

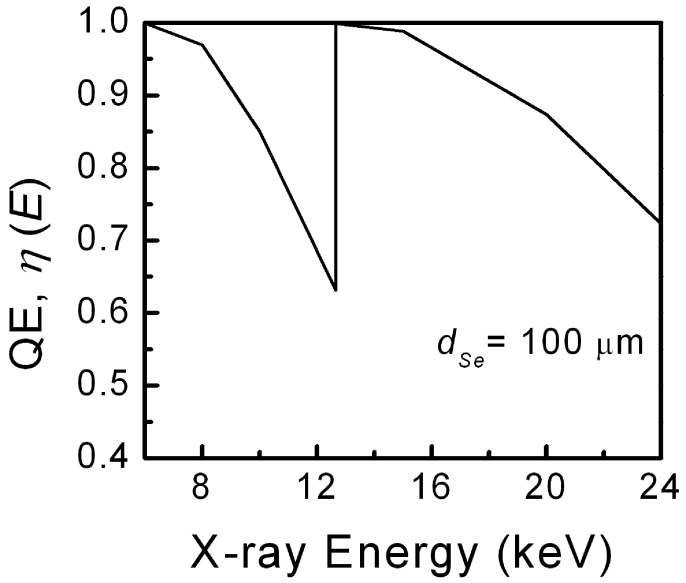

Figure 5.8: Quantum efficiency, $\eta(E)$, of 100 μm thick a-Se as a function of x-ray energy.

energy in Figure 5.8. The signal and noise propagation after absorption in the a-Se layer is given by:

$$\phi_1(f) = \int_0^{E_{max}} \eta(E)\phi_{in}(E)dE. \tag{5.18}$$

$$S_1(f) = \int_0^{E_{max}} \eta(E)\phi_{in}(E)dE. \tag{5.19}$$

The x-ray quantum noise still follows the Poisson distribution after attenuation by the a-Se layer, and both the signal and noise power spectra are spatially white.

5.3.2 X-ray Interaction in Parallel Processes

As shown in Figure 5.7, due to *K*-fluorescence, the propagation of signal and noise after x-ray absorption in a-Se layer is divided into three parallel paths:

A) when no *K*-fluorescence is generated, the absorbed x-ray energy is converted to charge locally;

B) when a *K*-fluorescence x-ray is produced, and the remaining x-ray energy is converted to charge locally;

Table 5.2: K-fluorescence related constants for a-Se.

Parameter	Values
f_K, the probability of K-shell interaction	0.864
ω_K, the probability of K-fluorescence production	0.596
I_α, the relative frequency of K_α	0.862
I_β, the relative frequency of K_β	0.138
K_α-fluorescence photon energy	11.21 keV
K_β-fluorescence photon energy	12.5 keV

C) when a K-fluorescence x-ray is reabsorbed remotely, and the energy is converted to charge and causes image blurring.

In order to find the propagation of signal and noise through these parallel paths some K-fluorescence related constants are needed, and they are given in Table 5.2 [58].

The signal and noise power spectra at the input of the three parallel paths A, B, and C (with subscripts A1, B1 and C1), respectively can be obtained as:

$$\phi_{A1}(f) = (1 - f_K\omega_K)\int_0^{E_{max}} \eta(E)\phi_{in}(E)dE = (1 - f_K\omega_K)\phi_1(f). \tag{5.20}$$

$$\phi_{B1}(f) = \phi_{C1}(f) = f_K\omega_K\int_0^{E_{max}} \eta(E)\phi_{in}(E)dE = f_K\omega_K\phi_1(f). \tag{5.21}$$

$$S_{A1}(f) = (1 - f_K\omega_K)\int_0^{E_{max}} \eta(E)\phi_{in}(E)dE = (1 - f_K\omega_K)\phi_1(f). \tag{5.22}$$

$$S_{B1}(f) = S_{C1}(f) = f_K\omega_K\int_0^{E_{max}} \eta(E)\phi_{in}(E)dE = f_K\omega_K\phi_1(f). \tag{5.23}$$

A. Path A

Here no K-fluorescence is generated, so all of the absorbed x-ray energy is converted to ehps. The mean conversion gain, g_A, of a-Se, i.e., the mean number of ehps generated after absorption of an x-ray of energy E is given by:

$$g_A = \frac{E}{W_\pm}, \tag{5.24}$$

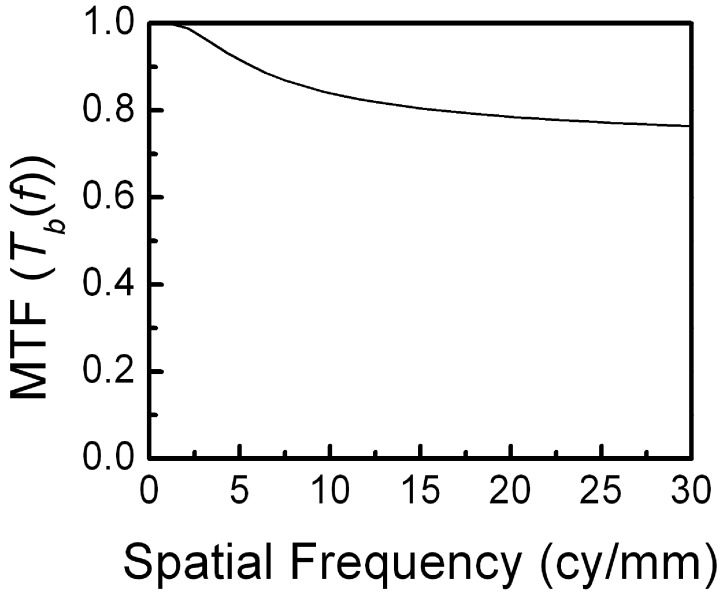

Figure 5.9: Modulation transfer function (MTF) of 100 μm thick a-Se layer.

where $W_{\pm}$ is the energy required to create an ehp in a-Se (defined by equation (2.1)). We assume that the noise associated with the conversion gain follows Poisson statistics for all three paths. So the variance associated with the conversion gain, σ_g^2, is equal to g.

The charge cloud from each x-ray interaction experiences blurring before reaching the pixel electrodes due to lateral movement of image charge or formation of an image by charge trapped in a plane above the pixel electrodes and a stochastic blurring stage, $T_b(f)$, is added after the conversion gain stage for all three parallel paths. Stochastic blurring is a process in which quanta are dispersed randomly into a spatial distribution with a probability given by the point spread function (PSF). $T_b(f)$ for incident x-rays with 20 keV energy is calculated based on the model of Que and Rowlands and shown in Figure 5.9 [51].

Following the standard equations for signal and noise propagation through gain and stochastic blurring stages [73], the signal and noise power spectra at the output of path A can be obtained as:

$$\phi_A(f) = (1 - f_K\omega_K)\phi_1(f)g_A T_b(f). \tag{5.25}$$

$$S_A(f) = (1 - f_K\omega_K)\phi_1(f)[g_A + g_A^2 T_b^2(f)]. \tag{5.26}$$

B. Path B

The conversion gain, g_B, of path B for an incident x-ray energy of E, is given by (E-E_k)/$W_{\pm}$, where E_k is the energy of the K-fluorescence photon (K_α has energy of 11.21 keV and K_β has energy of 12.5 keV). A stochastic blurring stage, $T_b(f)$, will be added after the conversion gain stage. The signal and noise power spectra at the output of path B can be obtained as:

$$\phi_B(f) = f_K \omega_K \phi_1(f) \sum_i (I_{ki} g_{Bi}) T_b(f). \tag{5.27}$$

$$S_B(f) = f_K \omega_K \phi_1(f) \sum_i [I_{ki}[g_{Bi} + g_{Bi}^2 T_b^2(f)]. \tag{5.28}$$

where i can be α or β.

C. Path C

For path C, there is a gain (selection) stage determined by the fraction of K-fluorescence reabsorbed,(PK), and a stochastic blurring process, $T_k(f)$, due to the reabsorption of K-fluorescence at a remote location. The conversion gain, g_C, of path C is given by E_k /$W_{\pm}$. A stochastic blurring stage, $T_b(f)$, will be added after the conversion gain stage. The signal and noise power spectra at the output of path C can be obtained as:

$$\phi_C(f) = f_K \omega_K \phi_1(f) \sum_i [I_{ki} P K_i g_{Ci} T_k(f)] T_b(f). \tag{5.29}$$

$$S_C(f) = f_K \omega_K \phi_1(f) \sum_i I_{ki} P K_i [g_{Ci} + g_{Ci}^2 T_b^2(f)]. \tag{5.30}$$

where i can be α or β.

Since paths B and C originate from the same incident x-ray, they are correlated, the NPS for cross correlation, $S_{BC}(f)$, is given by [71]:

$$S_{BC}(f) = f_K \omega_K \phi_1(f) \sum_i I_{ki} P K_i g_{Bi} g_{Ci} T_{ki} T_b^2(f). \tag{5.31}$$

Equation 5.31 indicates that when there is no additional source of blurring in a-Se, i.e., $T_b(f)$= 1, $S_{BC}(f)$ follows the shape of MTF due to K-fluorescence reabsorption. The total signal and NPS after K-fluorescence are obtained as a combination of the $\phi(f)$ and $S(f)$ of the three parallel paths using:

$$\phi_2(f) = \phi_A(f) + \phi_B(f) + \phi_C(f). \tag{5.32}$$

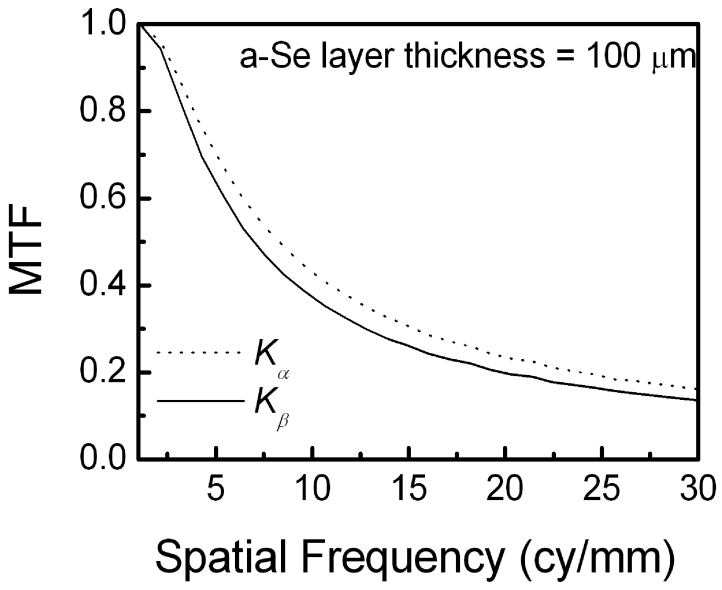

Figure 5.10: MTF for reabsorbed K-fluorescence photons for 100 μm thick a-Se.

$$S_2(f) = S_A(f) + S_B(f) + S_C(f) + 2S_{BC}(f). \tag{5.33}$$

In order to calculate $\phi_2(f)$ and $S_2(f)$, the values for PK and $T_k(f)$ have to be determined for both the K_α and K_β fluorescent x-rays. These values strongly depend on the thickness of the a-Se and the incident x-ray photon energy. We have calculated the values of PK for different thickness of a-Se for the energy range of protein crystallography in Chapter 3, and those results will be used here.

The modulation transfer function (MTF), $T_k(f)$, for reabsorbed K-fluorescence photons is calculated based on the model of Que and Rowlands and shown in Figure 5.10 for incident x-ray with 20 keV energy [51]. Since K_β photon has higher energy than K_α photon, $T_k(f)$ due to K_β decreased more rapidly as a function of spatial frequency than that of K_α photons.

In order to investigate the effect of a-Se thickness on MTF, $T_k(f)$ is calculated for different thicknesses for both K_α and K_β photons. Figure 5.11 shows that for both cases $T_k(f)$ degrades if the thickness of the a-Se layer is increased. This is due to the fact that the K-fluorescence reabsorption probability increases with the thickness of a-Se, so more charges will be generated at remote places. As a result, spatial resolution will be degraded.

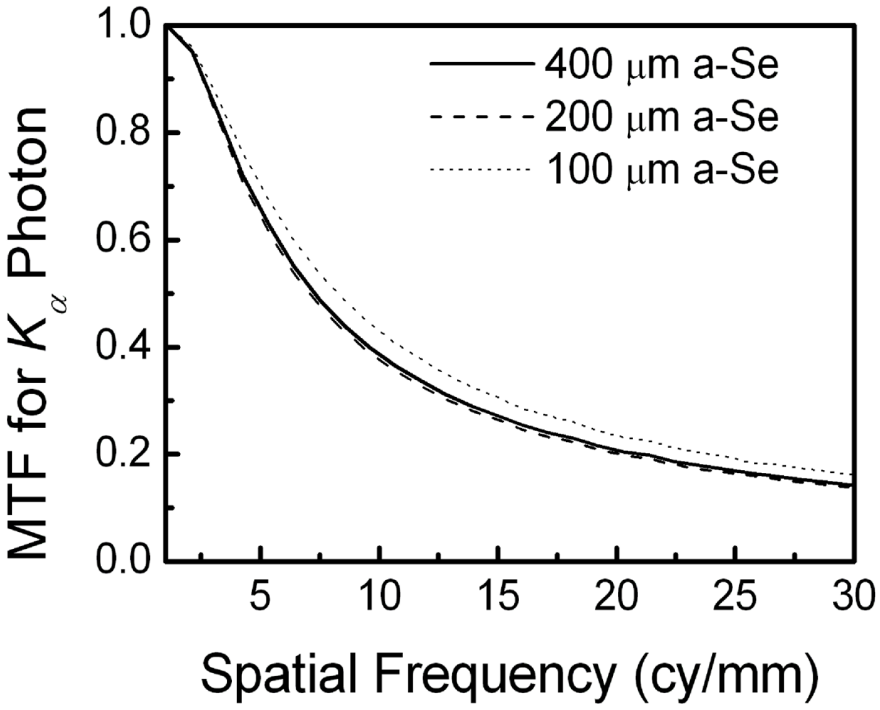

(a)

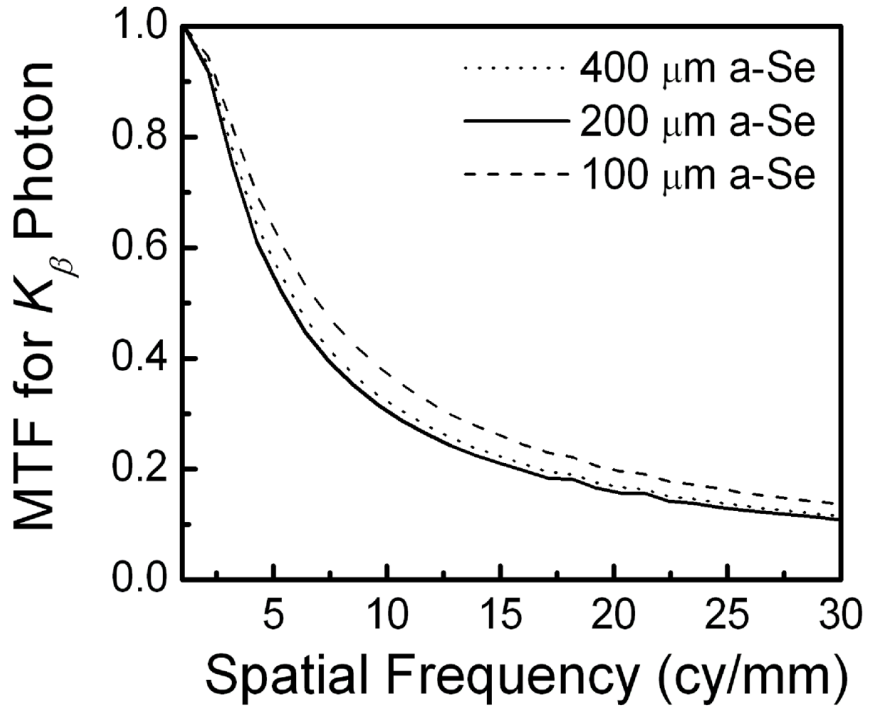

(b)

Figure 5.11: (a) MTF for reabsorbed K_α-photons for different thicknesses of a-Se, (b) MTF for reabsorbed K_β-photons for different thicknesses of a-Se.

5.3.3 Avalanche Gain

Avalanche multiplication is caused by carrier ionization events which occur with a statistically distributed probability. Therefore, the multiplication gain fluctuates from the mean value, resulting in generation of excess noise on the signal. Under the assumption that only holes avalanche in a-Se, the variance of the noise of avalanche gain is given by [37]:

$$\sigma_{g_{av}}^2 = g_{av}^2 - g_{av} \tag{5.34}$$

The total signal and NPS after this stage is:

$$\phi_3(f) = g_{av}\phi_2(f). \tag{5.35}$$

$$S_3(f) = g_{av}^2 S_2(f) + \sigma_{g_{av}}^2 \phi_2.$$

Substituting the value of $\sigma_{g_{av}}^2$:

$$S_3(f) = g_{av}^2(S_2(f) + \phi_2) - g_{av}\phi_2. \tag{5.36}$$

If the conversion gain is greater than 10 ehp/keV, the gain fluctuation noise of avalanche multiplication factor can be neglected [39]. This is because, so many x-rays are generated that the gain fluctuation noise is minimized. So we should maintain the electric field to such a value that we get a good conversion gain. We expect conversion gain of $\sim$ 60 ehp/keV for my experimental setup, and therefore avalanche gain noise will be negligible. Again, the avalanche gain is dependent on the location where the incident x-ray is absorbed. If x-rays are absorbed at the top of a-Se layer, the holes generated by this x-ray will traverse the entire thickness of a-Se and experience the largest avalanche gain. The holes generated by other x-rays absorbed deeper in a-Se layer will traverse a shorter distance, and hence their gain will be much less. This potentially results in considerable gain fluctuation noise. However, for the x-ray energy range of protein crystallography, the linear attenuation coefficient is high. So almost all x-rays are absorbed at or very close to the surface. So the path is same for all the x-rays and depth dependence noise of avalanche gain is minimized.

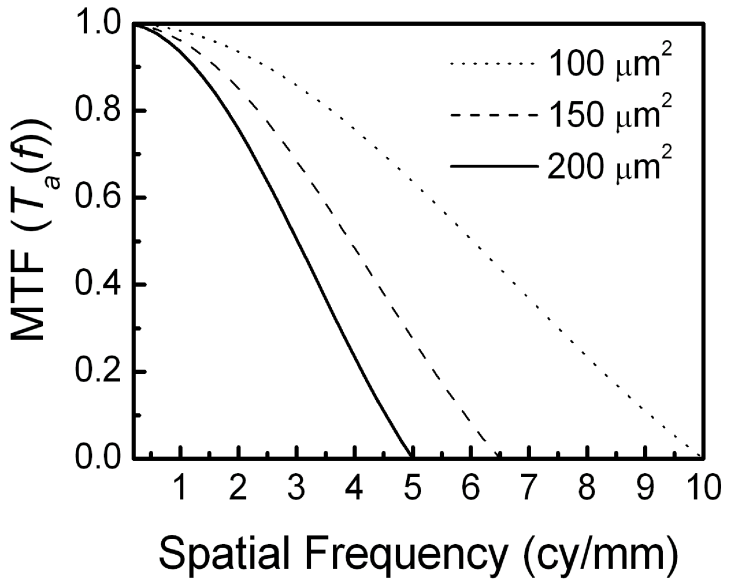

Figure 5.12: MTF for aperture function of different size of pixels.

5.3.4 Aperture Function

When the charge generated in a-Se reaches the surfaces of the detector, it will be collected and integrated on each pixel electrode. If the pixel electrode is square with width a, the two dimensional MTF associated with the aperture function of the pixel electrodes, T_a (f_x, f_y), can be written as,

$$T_a(f_x, f_y) = sinc(af_x)sinc(af_y), \tag{5.37}$$

where sinc(af_x)= sin (πaf_x)/(πaf_x). The process of image charge integration on pixel electrodes is deterministic blurring, the one dimensional signal spectrum is blurred by $T_a(f)$ which is a sinc function,

$$\phi_4(f) = T_a(f)\phi_3(f) = T_a(f)g_{av}\phi_2(f). \tag{5.38}$$

and the output two dimensional NPS is multiplied by the square of T_a (f_x, f_y),

$$S_4(f) = T_a^2(f)S_3(f). \tag{5.39}$$

Figure 5.12 shows the MTF associated with the aperture function of the pixel for different sizes of pixel.

5.3.5 Aliasing

For signal and noise propagation through the aliasing stage, only NPS is affected [73]. The NPS after aliasing is inversely proportional to the pixel fill factor, F_P. Pixel fill factor is the ratio of the active imager area to the total pixel area. For our pixel design, we adopted mushroom structure where the pixel electrodes occupy most of the pixel area. With this design, fill factor is almost unity, and we can neglect the effect of aliasing on NPS.

$$S_5(f) = S_4(f) \tag{5.40}$$

$$\phi_5(f) = \phi_4(f). \tag{5.41}$$

5.3.6 Addition of Readout Electronic Noise

During image readout, the electronic noise associated with the TFTs and the external charge amplifiers will be added to the total noise power. Since the electronic noise generated from each pixel is independent from each other, the NPS ($S_a(f)$) associated with the pixel electronic noise is spatially white, and will be added to $S_5(f)$ and form the final NPS at the output of the detector:

$$\phi_6(f) = \phi_5(f). \tag{5.42}$$

$$S_6(f) = S_5(f) + S_a(f) \tag{5.43}$$

From Chapter 2, we estimate the total electronic noise per pixel is 1700 electrons for pixel size of 150 μm^2.

5.3.7 Calculation of DQE

DQE(f) is defined by:

$$DQE(f) = \frac{SNR_{out}^2(f)}{SNR_{in}^2(f)} \tag{5.44}$$

The detector input signal and noise power spectra are given in (5.15), and (5.16). So,

$$SNR_{in}^2(f) = \frac{\overline{\phi_{in}}^2}{\overline{\phi_{in}}} = \overline{\phi_{in}}. \tag{5.45}$$

$$SNR_{out}^2(f) = \frac{{\phi_6}^2}{S_6}. \tag{5.46}$$

Now the DQE(f) at the output of the detector can be calculated by:

$$DQE(f) = \frac{\phi_6^2(f)}{S_6\overline{\phi_{in}}} \tag{5.47}$$

Substituting the values of $\phi_6(f)$ and $S_6(f)$ into (5.47) gives:

$$DQE(f) = \frac{T_a^2(f)g_{av}^2{\phi_2}^2(f)}{\overline{\phi_{in}}[T_a^2(f)(g_{av}^2(S_2(f)+\phi_2) - g_{av}\phi_2) + S_a(f)]}$$

Or,

$$DQE(f) = \frac{{\phi_2}^2(f)}{\overline{\phi_{in}}[S_2(f) + \phi_2 - \frac{\phi_2}{g_{av}} + \frac{S_a(f)}{T_a^2(f)g_{av}^2}]} \tag{5.48}$$

(5.48) shows that the electronic noise is divided by the square of g_{av}, and becomes negligible for high values of g_{av}. This demonstrates that introducing avalanche gain is an effective method for reducing noise. If there is no avalanche gain, $g_{av} = 1$, (5.48) becomes:

$$DQE(f) = \frac{{\phi_2}^2(f)}{\overline{\phi_{in}}[S_2(f) + \frac{S_a(f)}{T_a^2(f)}]} \tag{5.49}$$

The number of incident x-ray photon per unit area depends on the x-ray source used in the experiment. We consider a rotating anode source with 10^8 x-ray photons/s/mm^2. For 100 μm thick a-Se, PK is 0.726, and 0.04 for K_α, and K_β fluorescent x-rays respectively (from Chapter 3). We use avalanche gain of 10 and conversion gain of 59 ehp/keV for the calculation. The pixel size is considered as 150 μm^2. DQE (f) is calculated at 8 keV (no K-fluorescence reabsorption) and 20 keV (K-fluorescence reabsorption) to investigate the effect of K-fluorescence on DQE (f).

For incident x-ray of 8 keV energy, below the K-edge of Se (12.6 keV) no K-fluorescence is generated, so all of the absorbed x-ray energy is converted to ehps. Substituting (5.32) and (5.33) in (5.48) gives:

$$DQE(f) = \frac{T_b^2(f)T_a^2(f)}{\frac{2g_{av}+gg_{av}-1}{\eta g g_{av}} + \frac{S_A}{\overline{\phi_{in}}\eta^2 g^2 g_{av}^2}} \tag{5.50}$$

DQE (f) as a function of spatial frequency is calculated and plotted in Figure 5.13 (a). DQE (f) follows the square of the MTF of the pixel aperture function, T_a^2 (f). DQE (f) decreases from 0.96 at zero spatial frequency to 0.04 at spatial frequency 5 lp/mm.

Using a similar approach, DQE (f) for 20 keV x-ray energy as a function of spatial frequency is calculated and plotted in Figure 5.13 (b). Here also DQE (f) follows the

square of the MTF of the pixel aperture function, T_a^2 (f). It is clear that the DQE of the detector at higher spatial frequency is limited by the pixel size. The smaller the pixel size, the better the DQE at higher spatial frequency.

5.4 Summary

In this chapter, we have discussed the metastability phenomenon of a-Si:H TFT. We investigated the change in the characteristics of the a-Si:H TFT under pulse bias stress. We used the experimental results to predict the performance of the detector under practical operating condition. We also have developed a linear system model for the detector system and analyzed the performance of the detector in terms of detective quantum efficiency. It is evident from the calculation that that avalanche gain can reduce noise and improve overall DQE of the system.

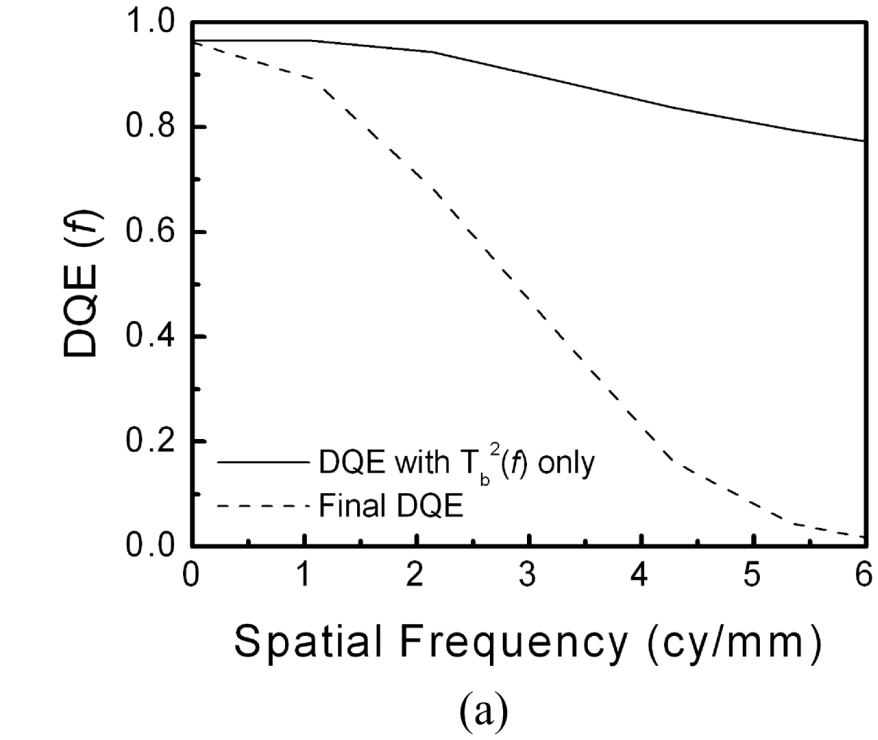

(a)

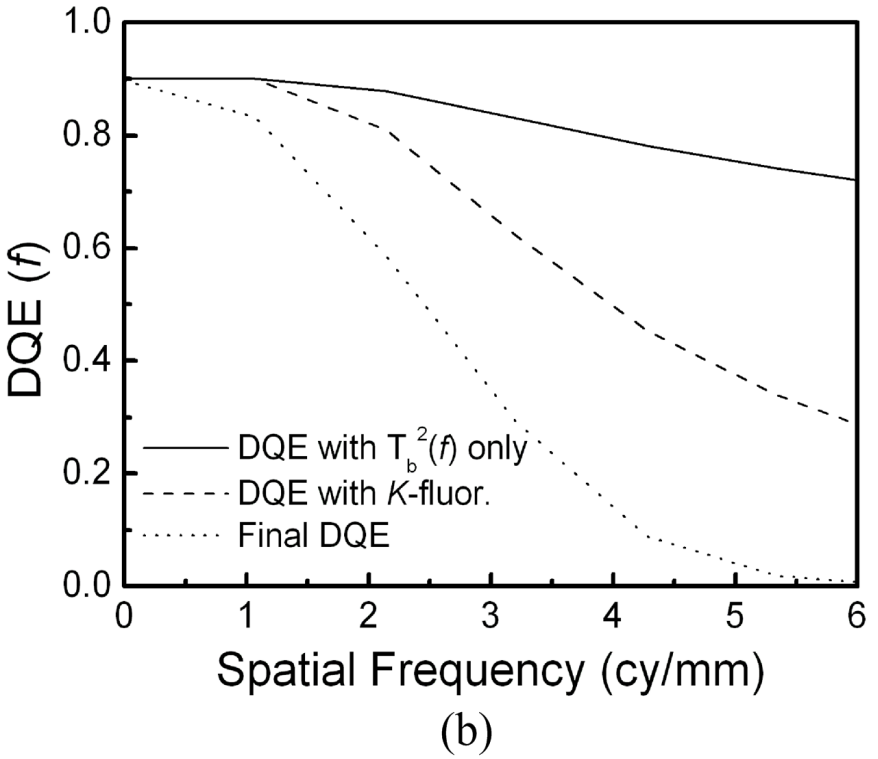

(b)

Figure 5.13: (a) DQE as a function of spatial frequency for 100 μm a-Se and 8 keV x-ray energy, (b) DQE as a function of spatial frequency for 100 μm a-Se and 20 keV x-ray energy.

Chapter 6

Conclusion

This chapter summarizes the contributions and achievements of this research and outlines future research directions arising from this work.

The need for the characterization of protein structure is increasing rapidly due to its application in basic biological research and pharmaceutical applications. An efficient method for determining protein structure is crystallography. The most commonly used detectors for protein crystallography are IP plates and CCDs. However, each of these detectors suffers from some drawbacks. While IP plate meets the requirement of large area detection, it lacks sufficient readout speed. Conversely, CCD detectors have acceptable readout speed, but they are expensive and are not large area compatible. The substantial need for an improved detector motivated our research on a new detector concept using a-Si:H TFT array as the charge readout system and a-Se photoconductor as the charge conversion system. The key contributions and possible future work from this research are summarized in the following sections.

6.1 Contributions to the Field

6.1.1 Development of a Large Area X-ray Imaging Detector for Protein Crystallography

In this work, we analyzed the requirements of a detector for protein crystallography and proposed a novel detector employing a-Se photoconductor as the x-ray to charge

conversion system and a-Si:H active matrix flat panel as the image charge readout system. We chose a-Si:H TFT array readout since large area imaging is required.

The requirement of high dynamic range is crucial for protein crystallography since both weak and strong diffraction spots need to be imaged. The main disadvantage of a-Si:H TFT arrays are their high electronic noise which prohibits quantum noise limited operation for the weaker diffraction spots. To overcome this problem, the x-ray to charge conversion gain of a-Se is increased by using its internal avalanche multiplication gain. To the best of our knowledge, integration of avalanche a-Se with a-Si:H TFT arrays have not been reported. The performance of the detector is analyzed in terms of readout time, quantum noise limited operation, maximum signal capacity, and spatial resolution.

Since the detector has high sensitivity it can also be used in other low signal applications, such as, fluoroscopy. Moreover, since the detector offers programmable gain it can be used in dual mode x-ray imaging applications.

6.1.2 Integration of Avalanche a-Se Layer with a-Si:H Pixel

In contrast to the HARP tube which requires vacuum operation for scanning electron beam signal readout, our proposed protein crystallography detector implements a pixellated electrode readout. We used an avalanche a-Se structure (HARP) of 15 μm thickness for our experiment. We integrated HARP with the a-Si:H pixel using a resistive layer (Cellulose Acetate) on top of the avalanche structure to avoid breakdown of the layer. Measurement results show that our avalanche a-Se structure can sustain the application of high electric field (F $\approx$ 100 V/μm) without breakdown. Our target avalanche gain of 10 can be achieved by applying electric field of $\sim$ 90 V/μm. This is the first time that an avalanche a-Se structure was connected to a-Si:H TFT without breakdown, showing proof of concept.

6.1.3 Development of a Linear System Model of the Detector to Characterize Its Performance

The overall imaging performance of the proposed protein crystallography detector depends on a large number of system parameters. The best method for optimizing such a

complex imaging system is to develop a cascaded linear system model so that its imaging performance can be predicted as a function of the system parameters. We developed a linear system model for our avalanche a-Se based imaging system using the parallel cascade approach, and investigated the effects of K-fluorescence and avalanche gain on DQE (f).

6.2 Future Work

The basic work for development of a highly sensitive large area x-ray detector for protein crystallography is presented here. The next step is to solve some implementation issues for integration of avalanche a-Se with a-Si:H TFT array.

6.2.1 For Indirect Detection X-ray Detector

i) Find a glue type material that can bond the avalanche a-Se layer with a-Si:H TFT array without compromising its imaging performance.

ii) Couple the avalanche a-Se/a-Si:H TFT array with a phosphor layer to test the detector with x-ray source.

6.2.2 For Direct Detection X-ray Detector

i) Develop properly working thick (100 μm) avalanche a-Se layer.

ii) Fabricate 30 cm $\times$ 30 cm a-Si:H TFT array.

iii) Facilitate safe work environment to work around 10 KV.

iv) Test the performance of detector using the x-ray source in our lab. Later the performance of the detector can be tested at the protein crystallography lab at University of Toronto.

Appendix A

Operation of a-Si:H Thin Film Transistor

a-Si:H TFT has three contact terminals: source, drain and gate. Depending on the terminal voltages, the operation regimes of the device can be divided into three regimes: Poole-Frenkel emission, subthreshold, and above-threshold. The above-threshold and forward subthreshold regimes of operation are referred to as forward regime ($V_{GS} > 0$ V) of operation. The reverse subthreshold and Poole-Frenkel regimes of operation are referred to as reverse regime ($V_{GS} < 0$ V) of operation, where the TFT is ideally OFF. Figure A.1 shows the different regimes of TFT operation.

i) Poole Frenkel regime: In the Poole Frenkel region (high negative V_{GS}), the TFT is OFF (as shown in Figure A.1); however the leakage current between the drain and source terminal increases exponentially with an increase in the negative gate voltage. The negative gate voltage accumulates holes in the front a-Si:H/a-SiN_x:H interface and induces the leakage current to flow. The holes are generated as a result of the Poole Frenkel field enhanced thermoionic emission at the gate-drain overlap vicinity. Here I_{DS} can be written as [74]:

$$I_{DS} = J_{OF}\ WOL \exp(\sqrt{|\frac{V_{GD}}{V_{PF}} + \gamma_p V_{DS}|}) \tag{A.1}$$

where J_{0F} is the effective current at zero bias, γ_p is a parameter accounting for two-dimensional effects (V^{-1}), WOL is the overlap area, and V_{PF} is the effective

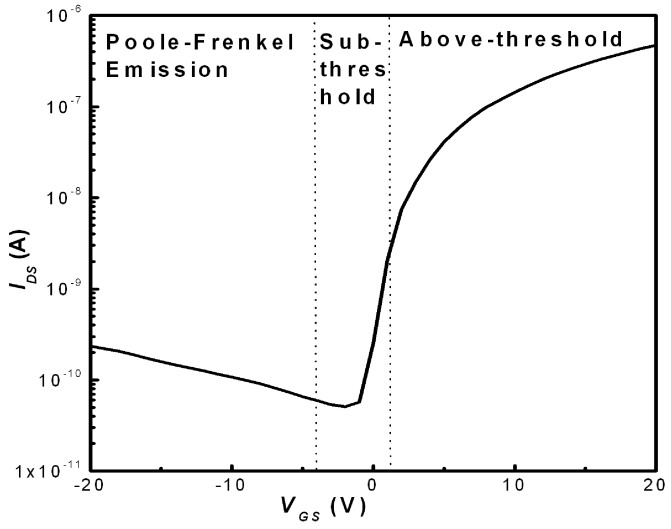

Figure A.1: Drain-source current, I_{DS}, as a function of gate-source voltage, V_{GS}, for V_{DS} = 20 V showing different regimes of TFT operation.

Poole-Frenkel voltage parameter. Usually the Poole-Frenkel current is written in terms of electric field (E):

$$I_{DS} = I_O \exp(\beta\sqrt{E}), \tag{A.2}$$

where I_O is the effective current at zero-electric field, and β is the field enhancement factor.

ii) Subthreshold regime: In the subthreshold regime, the TFT is in its exponential transition from OFF to ON. This regime of operation consists of two sub regimes: forward subthreshold and reverse subthreshold depending on the polarity of the gate bias.

In the forward subthreshold regime ($V_T > V_{GS} > V_{TS}$), although the gate voltage is positive, most of the induced electrons go into the deep localized acceptor-like states in the a-Si:H bandgap and into the interface states at the a-Si:H/insulator interface. A small number of electrons participate in conduction, which leads to small subthreshold current of the order of 10^{-12}-10^{-8} A. In the subthreshold region, I_{DS} can be written as [74]:

$$I_{DS} = I_{OS}\frac{W}{L}\exp[\frac{(V_{GS} - V_{TS})}{S_f}]. \tag{A.3}$$

where V_{TS} denotes the boundary of the forward subthreshold region, I_{OS} is the

magnitude of current in the subthreshold region, and S_f is the forward subthreshold slope, which is a measure of the density of states at the front interfaces, and is given by:

$$S_f = \alpha v_{th}(1 + \frac{C_{SS}}{C_i}). \tag{A.4}$$

Here, α is the power parameter, v_{th} is the thermal voltage and C_{ss} is the effective interface capacitance. As the positive bias on the gate increases the density of electrons increases, which leads to an exponential growth of current and subsequent transition to the above-threshold regime of operation.

In the reverse subthreshold region, the negative gate voltage depletes most of the accumulated electrons from the front interface. However, due to a high density of states in the interface a weak electron channel (back channel) exists at the back interface that provides the means for conduction. Here I_{DS} can be written as [74]:

$$I_{DS} = I_{OS}\frac{W}{L}\exp[\frac{(V_{GS} - V_{TS})}{(S_r + \gamma_n|V_{DS}|)}]. \tag{A.5}$$

where S_r is the reverse subthreshold slope, and γ_n is a unitless parameter accounting for two dimensional effects. Further decrease in the negative gate voltage decreases the subthreshold current and results in a subsequent transition into the Poole-Frenkel regime of operation.

iii) Above-threshold regime: In the above-threshold regime ($V_{GS} > V_T$), the TFT is ON and conducts a significant amount of current between its drain and source terminals. In this regime the Fermi level enters into the conduction band tail. And as a result, more electrons can participate in conduction and the TFT is able to supply a high ($\sim \mu$ A) current. Due to the fast exponential increase in the density of states in the tail states, the shift of the Fermi level with the gate voltage is considerably smaller than in the subthreshold regime. This phenomenon identifies the above-threshold regime of operation. Accordingly, the threshold voltage (V_T) may be defined as the voltage at which the Fermi level moves to the tail states.

Depending on the value of V_{DS}, this above-threshold region can be divided in to two regions. In the linear region ($V_{DS} \ll V_{GS}$), drain current I_{DS} can be written as:

$$I_{DS} = \mu_{eff}\zeta {C_i}^{\alpha-1}\frac{W}{L}(V_{GS} - V_T)^{\alpha-1}V_{DS}. \tag{A.6}$$

Table A.1: Typical values of a-Si TFT device parameters.

Physical Parameters	Value
μ_{eff}(effective mobility)	0.4 - 0.9 cm^2/V-s
V_T (threshold voltage)	3 - 4 V
α (power parameter)	2 - 2.27

Here μ_{eff} is the effective field mobility, W and L are the effective channel width and channel length, respectively, C_i is the gate dielectric capacitance, α is the power parameter, and ζ is an empirical parameter which is dependent on α.

For V_{DS} higher than the saturation voltage V_{DSat} , the TFT operates in the saturation region. The saturation voltage, V_{DSat}, is the voltage for which the density of mobile carriers at the drain side of the channel reduces to zero (pinch off condition) and is given by the following:

$$V_{Dsat} = \alpha_{sat}(V_{GS} - V_T). \tag{A.7}$$

where α_{sat} is the saturation parameter. The drain current in the saturation region can be written as,

$$I_{DS} = \frac{\mu_{eff}}{\alpha}\zeta {C_i}^{\alpha-1}\frac{W}{L}\gamma_{sat}(V_{GS} - V_T)^{\alpha}\chi_{cm}. \tag{A.8}$$

The parameter χ_{cm} $(= 1 + \lambda_{DS})$ in A.8 accounts for channel length modulation, where λ is the channel length modulation parameter and γ_{sat} is given by:

$$\gamma_{sat} = 1 - (1 - \alpha_{sat})^{\alpha}. \tag{A.9}$$

Typical values for the a-Si TFT device parameters are given in Table A.1.

Appendix B

Mask Layout of a-Si:H TFT Arrays

Mask layouts were designed using Cadence software, 180 nm CMOS Technology.

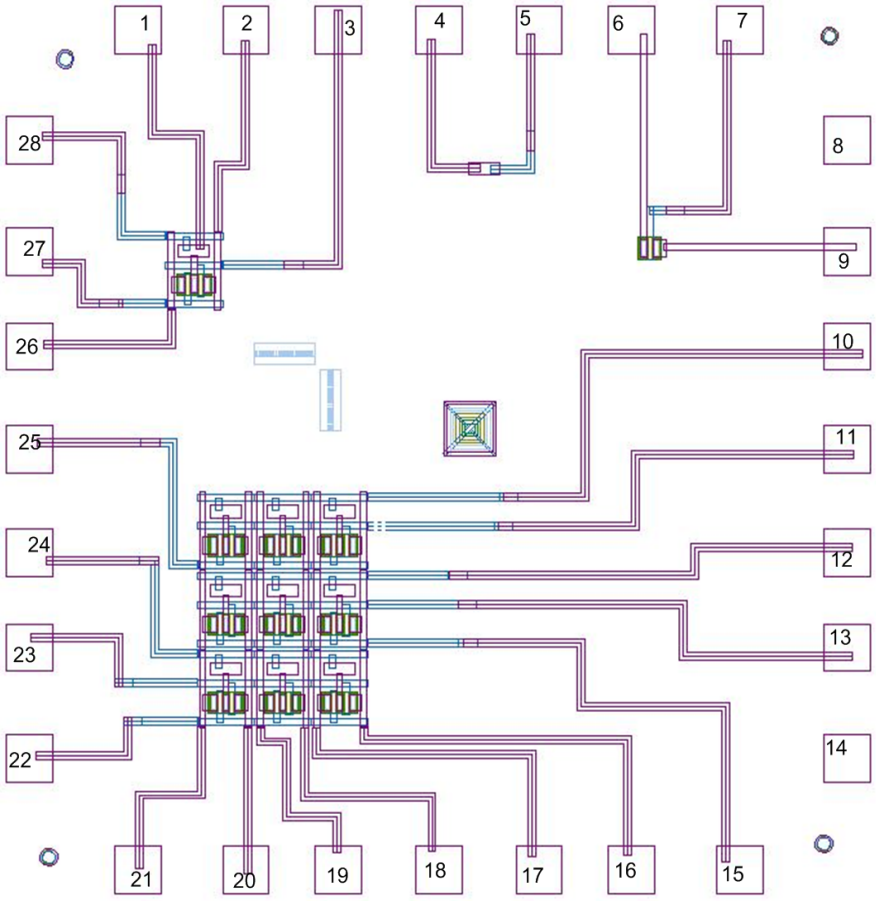

Figure B.1: 3 × 3 array with 175 μm^2 pixel, and associated test structures.

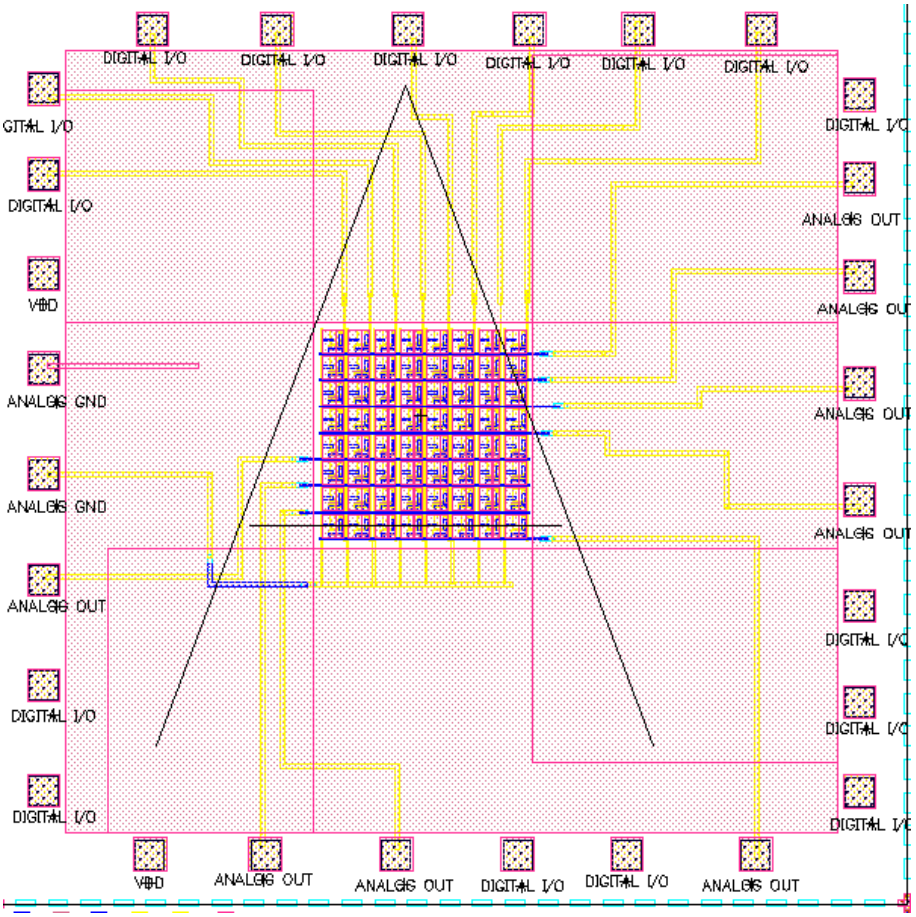

Figure B.2: 8×8 array with 250 μm^2 pixel for integration with avalanche a-Se photoconductor.

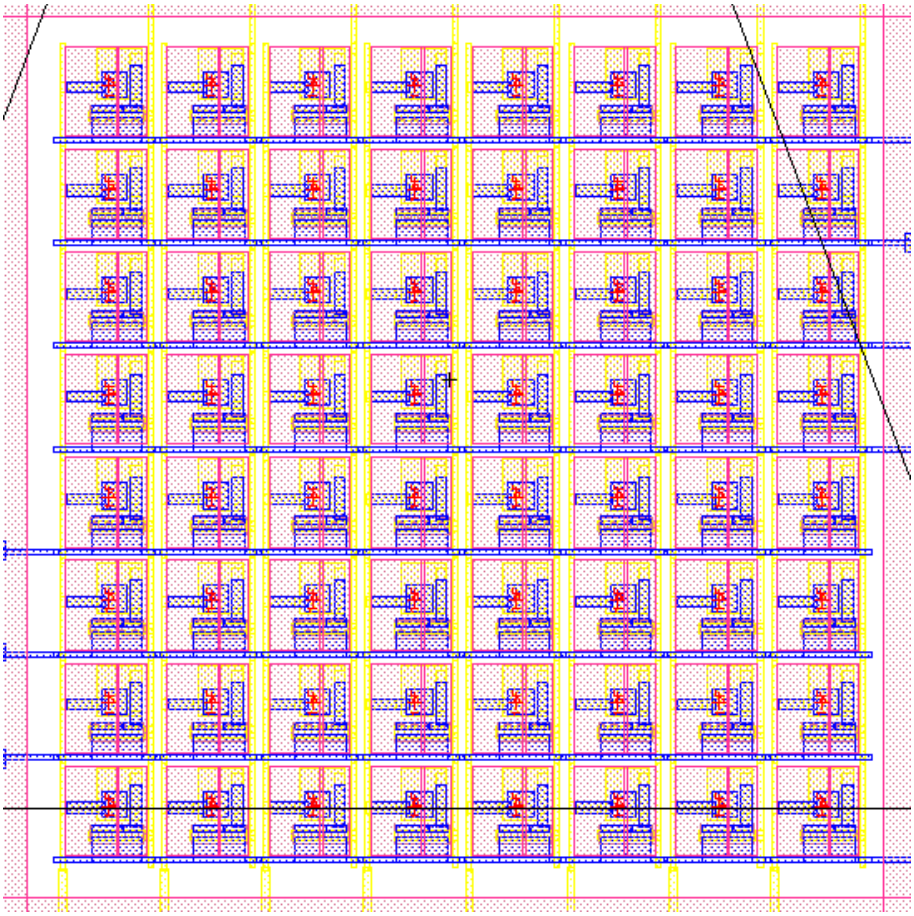

Figure B.3: Close view of 8 × 8 array with 250 μm^2 pixel.

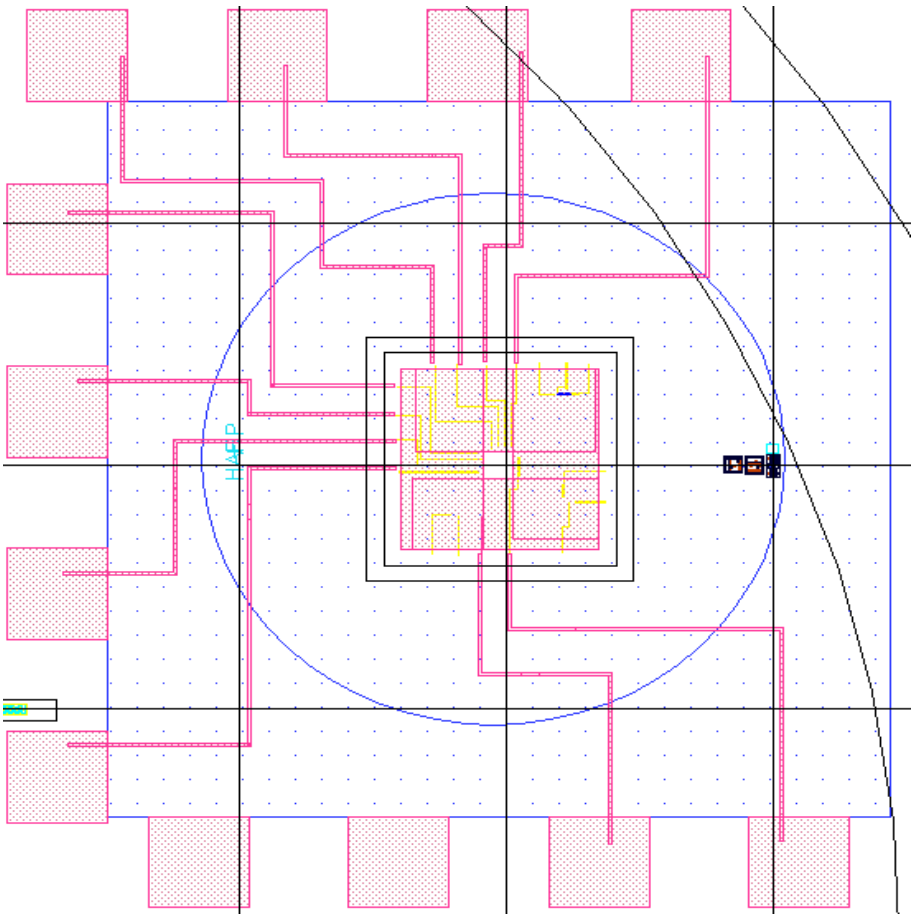

Figure B.4: a-Si:H TFT array designed for integration with HARP.

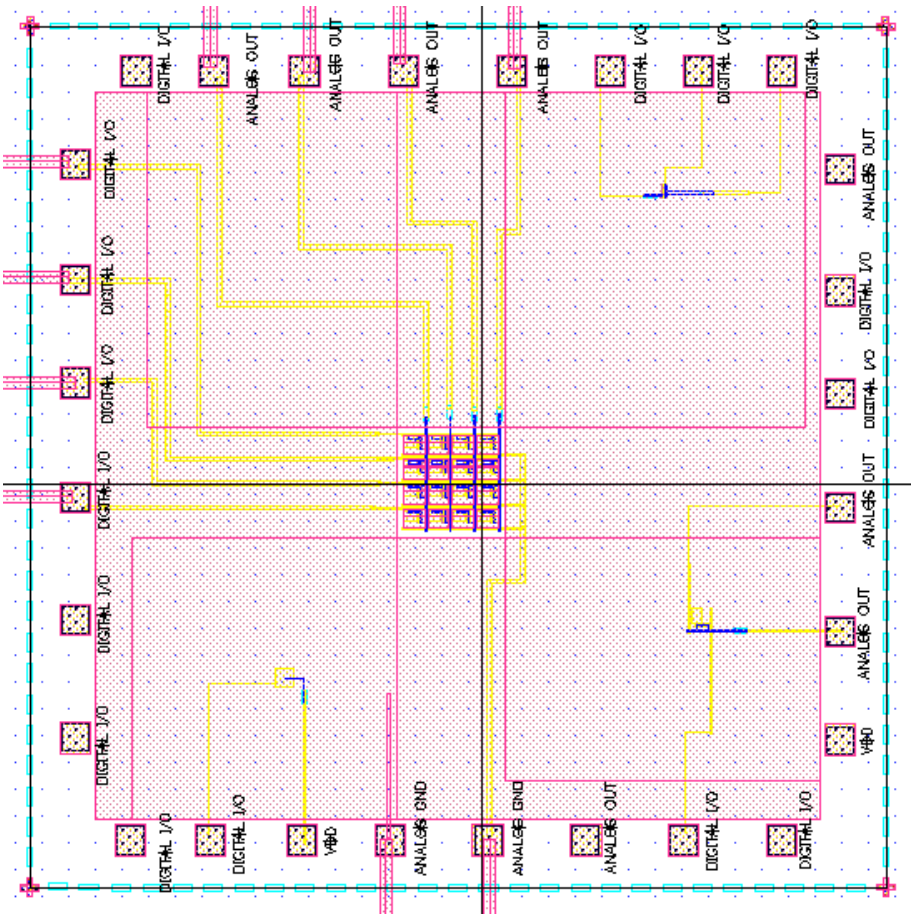

Figure B.5: Close view of a-Si:H TFT array designed for integration with HARP.

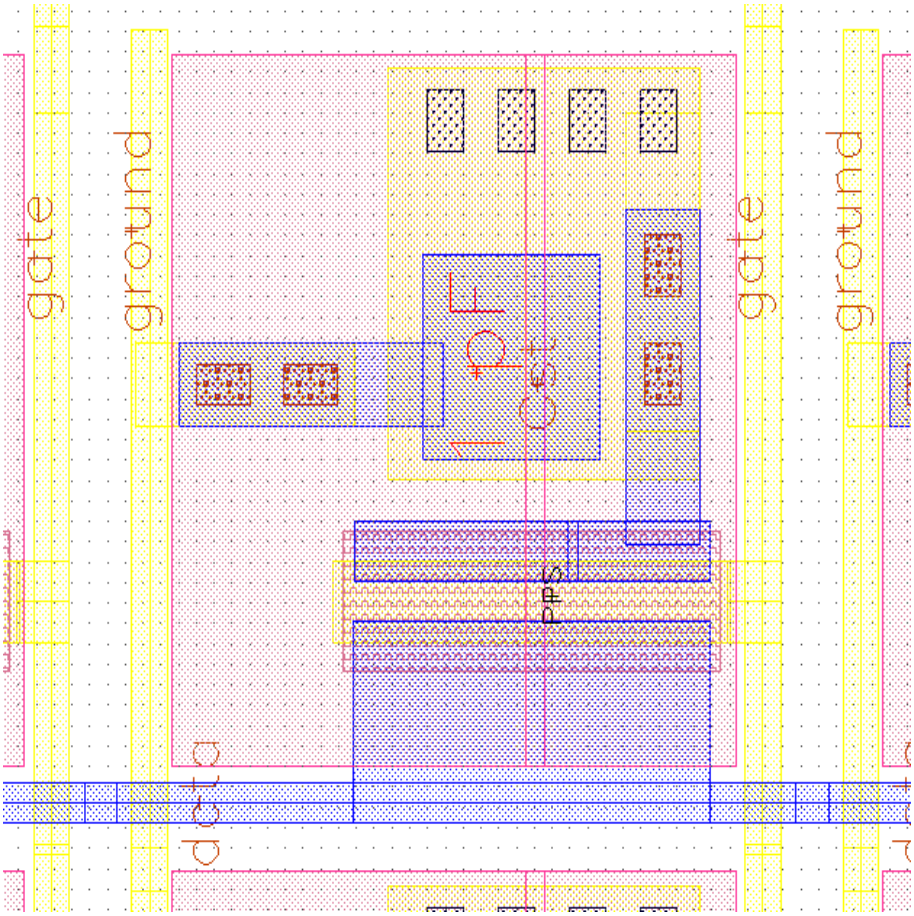

Figure B.6: Layout of a single pixel showing a-Si:H TFT, C_{st}, data line and gate line.

Appendix C

Protein Crystallization

Crystallization is a process by which a metastable supersaturated solution can reach a stable lower energy state by reduction of solute concentration. Crystallization process is similar for molecules of both microscopic (salts and small organics) and macroscopic (proteins, DNA, RNA) dimensions.

Protein crystallization is mainly a trial-and-error procedure in which the protein is slowly precipitated from its solution. The crystallization of proteins involves four important steps:

i) The purity of the protein is determined. If it is not extremely pure, further purification is necessary to achieve crystallization.

ii) The protein is dissolved in a suitable solvent from which it must be precipitated in crystalline form.

iii) The solution is brought to supersaturation. In this step small aggregates are formed, which are the nuclei for crystal growth.

iv) Once nuclei have been formed, actual crystal growth can begin.

C.1 Crystallization Techniques:

C.1.1 Batch crystallization

This is the oldest and simplest method for protein crystallization. The precipitating reagent is instantaneously added to the protein solution, the solution is then suddenly brought to high supersaturation state. With luck, crystals grow gradually from the supersaturated solution without further processing.

C.1.2 Liquid-Liquid Diffusion

In this method the protein solution and the precipitant solution are layered on top of each other in a small-bore capillary. The lower layer is the solution with higher density (usually in the form of protein solution onto precipitant solution). Nucleation and crystal growth generally occurs at the interface between the two layers, at which both the concentration of precipitant and the concentration of protein are at their highest values. The two solutions slowly intermix over time, and should be made up so that at equilibrium the concentration of the precipitant is still high enough to promote crystal growth.

C.1.3 Vapor Diffusion

The vapor diffusion technique utilizes evaporation and diffusion of water between solutions of different concentration as a means of approaching and achieving supersaturation of macromolecules.

Vapor diffusion method tends to form smaller crystals than other methods. However, the most commonly used methods for initial crystal trials are the hanging drop and sitting drop vapor diffusion methods.

i) Hanging drop vapor diffusion method: In this method protein drops are prepared on a siliconized microscope glass cover slip by mixing 3-10 μl of the protein solution with the same volume of precipitant solution. The glass slip is siliconized to prevent spreading of the drop. The slip is placed upside down over a well in a tray; the well is partly filled with the required precipitant solution (approximately 1 ml). The

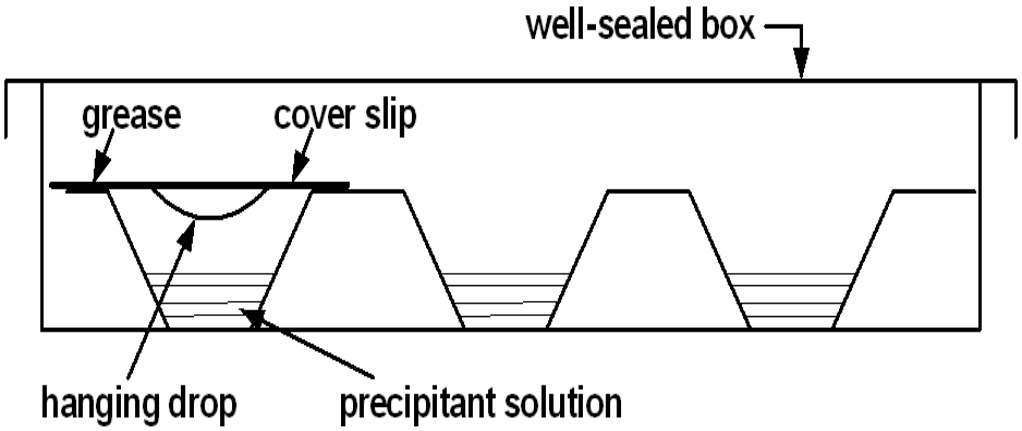

(a)

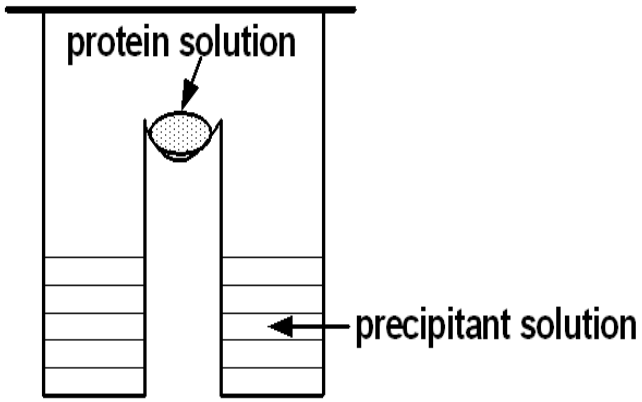

(b)

Figure C.1: (a) The hanging drop method of protein crystallization, (b) The Sitting drop method of protein crystallization.

chamber is sealed by applying oil or grease to the circumference of the well (see Figure C.1(a)). Equilibrium is reached by diffusion of vapor from the drop to the precipitating solution or vice versa.

ii) Sitting drop vapor diffusion method: If the protein solution has a low surface tension, it tends to spread out over the cover slip in the hanging drop method. In such cases the sitting drop method is preferable. A schematic diagram of a sitting drop vessel is shown in Figure C.1 (b).

C.1.4 Dialysis

Dialysis techniques utilize diffusion and equilibration of small precipitant molecules through a semipermeable membrane to achieve the concentration at which the macromolecule solute crystallizes. The precipitant solution can be changed easily and thus protein can be continuously recycled until the correct conditions for crystallization are found. For moderate amount of protein solution (more than 0.1 ml), dialysis tubes can be used, whereas for micro liter amounts of protein solution one may use either a thick-walled micro-capillary or a dialysis button covered with a dialysis membrane.

References

[1] M. W. Parker, "Protein structure from x-ray diffraction," *Journal of Biological Physics*, vol. 29, pp. 341–362, 2003. 1, 2, 37, 38

[2] C. Nave, "Sources, instrumentation and detectors for protein crystallography," *Nucl. Instrum. Methods A*, vol. 467-468, pp. 1286–1293, 2001. 2

[3] E. Pechkova and C. Nicolini, *Proteomics and Nanocrystallography.* New York: Kluwer Academic, 2003. 2

[4] I. Naday, S. Ross, E. M. Westbrook, and G. Zentai, "Charge-coupled device/fiber optic taper array x-ray detector for protein crystallography," *Opt. Eng.*, vol. 37, no. 4, pp. 1235–1244, 1998. 3, 4, 6, 8

[5] M. Stanton, W. Phillips, D. O'Mara, I. Naday, and E. Westbrook, "Area detector design Part II. Application to a modular CCD-based detector for X-ray crystallography," *Nucl. Instrum. Methods A*, vol. 325, pp. 558–567, 1993. 4, 6, 24, 25

[6] S. Ross, G. Zentai, K. S. Shah, R. W. Alkire, I. Naday, and E. M. Westbrook, "Amorphous silicon, semiconductor x-ray converter detectors for protein crystallography," *Nucl. Instrum. Methods A*, vol. 399, pp. 38–50, 1997. 4, 5, 6, 9

[7] G. H. Stout and L. H. Jensen, *X-ray Structure Determination.* New York: John Wiley and Sons, 1989. 5

[8] M. G. Strauss, "Large aperture CCD x-ray detector for protein crystallography using a fiberoptic taper," *in Proc. SPIE*, vol. 1447, pp. 12–27, 1991. 5

[9] N. Shimizu, K. Hirata, K. Hasegawa, G. Uenob, and M. Yamamotoa, "Dose dependence of radiation damage for protein crystals studied at various X-ray energies," *J. Synchrotron Rad*, vol. 14, pp. 4–10, 2007. 5

[10] J. Drenth, *Principles of Protein X-ray Crystallography.* New York: Springer-Verlag, 2007. 5, 34, 35, 36, 39, 40, 41

[11] E. M. Westbrook, "Performance characteristics needed for protein crystal diffraction x-ray detectors," in *in Proc. SPIE*, pp. 2–16, 1999. 6, 7, 8

[12] R. Chechik, A. Breskin, I. Frumkin, A. Gabriel, and M. Kocsis, "Real-time secondary electron emission detector for high-rate x-ray crystallography," *IEEE Trans. On. Nucl. Sci.*, vol. 43, pp. 1248–1252, 1996. 6

[13] http://www.marresearch.com/products.html. 7, 11

[14] http://www.rigaku.com/protein/detectors.html. 7, 8, 11

[15] J.-P. Moy, "Large area x-ray detectors based on amorphous silicon technology," *Thin Film Solids*, vol. 337, pp. 213–221, 1999. 8, 21

[16] N. Yagi, M. Yamamoto, K. Uesugi, and K. Inoue, "A large-area CMOS imager as an X-ray detector for synchrotron radiation experiments," *J. Synchrotron Rad.*, vol. 11, pp. 347–352, 2004. 8

[17] J. Rowlands and J. Yorkston, *Flat panel detectors for digital radiography, Medical Imaging. Volume 1 Physics and Psychophysics.* Bellingham: SPIE, 2000. 9, 10

[18] K. S. Karim, A. Nathan, and J. A. Rowlands, "Amorphous silicon active pixel sensor readout circuit for digital imaging," *IEEE Trans. Electron. Devices*, vol. 50, pp. 200–208, 2003. 9, 25

[19] W. Zhao and J. Rowlands, "X-ray imaging using amorphous selenium: Feasibility of a flat panel self-scanned detector for digital radiology," *Med. Phys.*, vol. 22, pp. 1595–1604, 1995. 9, 31, 32

[20] W. Zhao, D. Li, A. Reznik, B. J. M. Lui, D. Hunt, J. A. Rowlands, Y. Ohkawa, and K. Tanioka, "Indirect flat-panel detector with avalanche gain: Fundamental

feasibitly investigation for SHARP-AMFPI (scintillator HARP active matrix flat panel imager)," *Med. Phys.*, vol. 32, pp. 2954–2966, 2005. 9, 85, 86, 87

[21] http://www.marresearch.com/products.mar555.html. 9

[22] A. Sultana, A. Reznik, K. S. Karim, and J. Rowlands, "Design and feasibility of active matrix flat panel detector using avalanche amorphous selenium for protein crystallography," *Med. Phys.*, vol. 35, pp. 4324–4332, 2008. 9

[23] L. E. Antonuk, K.-W. Jee, Y. El-Mohri, M. Maolinbay, S. Nassif, X. Rong, Q. Zhao, J. H. Siewerdsen, R. A. Street, and K. S. Shah, "Strategies to improve the signal and noise performance of active matrix, flat-panel imagers for diagnostic x-ray applications," *Med. Phys.*, vol. 27, pp. 289–306, Feb. 2000. 12, 25, 28

[24] D. C. Hunt, S. S. Kirby, and J. A. Rowlands, "X-ray imaging with amorphous selenium: x-ray to charge conversion gain and avalanche multiplication gain," *Med. Phys.*, vol. 29, pp. 2464–2471, 2002. 12, 23, 25, 28, 30

[25] A. Reznik, S. Baranovskii, O. Rubel, G. Juska, S. Kasap, Y.Ohkawa, K. Tanioka, and J. A. Rowlands, "Avalanche multiplication phenomenon in amorphous semiconductors: Amorphous selenium versus hydrogenated amorphous silicon," *J. Appl. Phys.*, vol. 102, p. 053711, 2007. 13, 17, 23, 28

[26] K. Tsuji, T. Ohshima, T. Hirai, N. Gotoh, K. Tanioka, and K. Shidara, "Ultra-high-sensitive image pickup tubes using avalanche multiplication in a-Se," *in Proc. MRS. Symp.*, vol. 219, pp. 507–518, 1991. 13, 18, 20

[27] S. O. Kasap and J. A. Rowlands, "Photoconductor selection for digital flat panel x-ray image detectors based on the dark current," *J. Vac. Sci. Technol. A*, vol. 18, pp. 615–620, 2000. 15

[28] S. O. Kasap, C. Haugen, M. Nesdoly, and J. A. Rowlands, "Properties of a-Se for use in flat panel x-ray image detectors," *Journal of Non-Crystalline Solids*, vol. 266-269, pp. 1163–1167, 2000. 16, 27

[29] S. Kasap, J. A. Rowlands, B. Fogal, M. Z. Kabir, G. Belev, N. Sidhu, B. Polischuk, and R. E. Johanson, "Progress in the science and technology of direct conversion

a-Se X-ray sensors," *Journal of Non-Crystalline Solids*, vol. 299-302, pp. 988–992, 2002. 16

[30] B. Polischuk, Z. Shukri, A. Legros, and H. Rougeot, "A novel selenium direct converter structure for static and dynamic x-ray detection in medical imaging applications," *in Proc. SPIE*, vol. 3336, pp. 494–506, 1998. 16

[31] A. Rose, "Quantum and noise limitations of the visual process," *J. Opt. Soc. Am.*, vol. 43, pp. 715–716, 1953. 16

[32] A. Rose, *Television pickup tubes and the problem of vision.* New York: Academic, 1948. 16

[33] S. O. Kasap, "X-ray sensitivity of photoconductors: application to stabilized a-Se," *J. Phys. D: Appl. Phys.*, vol. 33, pp. 2853–2865, 2000. 17

[34] G. Juska and K. Arlauskas, "Impact ionization and moblilities of charge carriers at high electric fields in amorphous selenium," *Phys. Status Solidi A*, vol. 59, p. 389, 1980. 17, 18

[35] A. Reznik, S. Baranovskii, O. Rubel, K. Jandieri, S. Kasap, Y. Ohkawa, M. Kubota, K. Tanioka, and J. Rowlands, "Avalanche multiplication in amorphous selenium and its utilization in imaging,," *Journal of Non-Crystalline Solids*, vol. 354, pp. 2691–2696, 2008. 17, 20, 28

[36] S. M. Sze, *Physics of Semiconductor Devices.* New York: Wiley, 1981. 18

[37] A. S. Tager, "Current fluctuations in a semiconductor (dielectric) under the conditions of impact ionization and avalanche breakdown," *Sov. Phys. Solid State*, vol. 6, p. 1919, 1965. 19, 96

[38] D. C. Hunt, K. Taioka, and J. A. Rowlands, "X-ray imaging using avalanche multiplication in amorphous selenium: Investigation of intrinsic avalanche noise," *Med. Phys.*, vol. 34, pp. 4654–4663, Dec. 2007. 19

[39] D. C. Hunt, K. Taioka, and J. A. Rowlands, "X-ray imaging using avalanche multiplication in amorphous selenium: Investigation of depth dependent avalanche noise," *Med. Phys.*, vol. 34, pp. 976–986, 2007. 19, 96

[40] R. Street, *Technology and Applications of Amorphous Silicon*. New York: Springer. 21

[41] F. R. Libsch and J. Kanicki, "Bias-stress-induced stretched-exponential time dependence of charge injection and trapping in amorphous silicon thin-film transistors," *Appl. Phys. Lett.*, vol. 62, pp. 1286–1288, 1993. 22, 76, 80

[42] M. J. Powell, C. van Berkel, and J. R. Hughes, "Time and temperature dependence of instability mechanisms in amorphous silicon thin-film transistors," *Appl. Phys. Lett.*, vol. 54, pp. 1323–1325, 1989. 22, 76, 77, 80

[43] W.-D. Park and K. Tanioka, "Avalanche-type high sensitive image pickup tube using an a-Se photoconductive target," *Jpn. J. Appl. Phys.*, vol. 42, pp. L209–L211, 2003. 23

[44] M. Stanton, "Area detector design Part I. Formulation of design criteria and application to X-ray crystallography," *Nucl. Instrum. Methods A*, vol. 325, pp. 550–557, 1993. 24, 25

[45] K. S. Karim, P. Servati, and A. Nathan, "High voltage amorphous silicon TFT for use in large area applications," *Microelectronics Journal*, vol. 35, pp. 311–315, 2004. 25

[46] K. S. Karim, A. Nathan, M. Hack, and W. I. Milne, "Drain-bias dependence of threshold voltage stability of amorphous silicon TFTs," *IEEE Elec. Dev. Lett.*, vol. 25, pp. 188–190, 2004. 25, 75, 80

[47] http://physics.nist.gov/PhysRefData/XrayMassCoef?cover.html. 27

[48] M. Maolinbay, Y. El-Mohri, L. E. Antonuk, K.-W. Jee, S. Nassif, X. Rong, and Q. Zhao, "Additive noise properties of active matrix flat-panel imagers," *Med. Phys.*, vol. 27, pp. 1841–1854, August 2000. 31, 32

[49] K. Rossmann, "The spatial frequency spectrum: a means for studying the quality of radiographic imaging systems," *Radiology*, vol. 90, pp. 1–13, 1968. 32

[50] K. Rossmann, "Point spread-function, line spread-function, and modulation transfer function," *Radiology*, vol. 93, pp. 257–272, 1969. 32

[51] W. Que and J. A. Rowlands, "X-ray imaging using amorphous selenium: inherent spatial resolution," *Med. Phys.*, vol. 22, pp. 365–374, 1995. 33, 92, 94

[52] G. Bricogne, S. C. Capelli, G. Evans, A. Mitschler, P. Pattison, P. Roversi, and M. Schiltzg, "X-ray absorption, refraction and resonant scattering tensors in selenated protein crystals: implications for data collection strategies in macromolecular crystallography," *J. Appl. Cryst.*, vol. 38, pp. 168–182, 2005. 38, 40, 41

[53] http://skuld.bmsc.washington.edu/scatter/ASform.html. 39

[54] G. Hajdok, J. Yao, J. J. battista, and I. A. Cunningham, "Signal and noise transfer properties of photoelectric interactions in diagnostic x-ray imaging detectors," *Med. Phys.*, vol. 33, pp. 3601–3620, Oct. 2006. 43, 45, 51

[55] M. Z. Kabir and S. O. Kasap, "DQE of photoconductive x-ray image detectors: application to a-Se," *J. Phys. D: Appl. Phys.*, vol. 35, p. 27352743, 2002. 44

[56] J. M. Boone, J. A. Seibert, J. M. Sabol, and M. Tecotzky, "A Monte Carlo study of x-ray fluorescence in x-ray detectors," *Med. Phys.*, vol. 26, pp. 905–916, 1999. 45

[57] H.-P. Chan and K. Doi, "Energy and angular dependence of x-ray absorption and its effect on radiographic response in screen-film systems," *Phys. Med. Biol.*, vol. 28, pp. 565–579, 1983. 45, 47

[58] W. Zhao, W. G. Li, and J. A. Rowlands, "Effects of characteristic x-rays on the noise power spectra and detective quantum efficiency of photoconductive x-ray detectors," *Med. Phys.*, vol. 28, pp. 2039–2049, Oct. 2001. 47, 91

[59] R. Fahrig, J. A. Rowlands, and M. J. Yaffe, "X-ray imaging with amorhpus selenium: Detective quantum efficieny of photoconductive receptors for digital mammography," *Med. Phys.*, vol. 22, pp. 153–160, Oct. 1995. 51

[60] A. Miri, S. Mohajerzadeh, and A. Nathan, "A modified inverted-staggered TFT structure suitable for a fully wet etch fabrication process for high performance low and high voltgae a-Si:H TFTs," *in Proc. of the 12th International Confernece on Microelectronics*, p. 241, October 2000. 54

[61] R. V. R. Murthy, P. Servati, A. Nathan, and S. G. Chamberlain, "Optimization of $n^+\mu$cSi:H contact layer for low leakage current in a-Si:H thin film transistors," *J. Vac. Sci. Technol. B*, vol. 18, p. 685, 2000. 55

[62] M. Yamauchi, T. Hayashida, M. Kosugi, K. Moroboshi, T. Watabe, Y. Ishiguro, K. Yamano, H. Ohtake, T. Tajima, T. Watanabe, H. Kokubun, M. Abe, and K. Tanioka, "CMOS image sensor overlaid with a HARP photo-conversion film," *in Optoelectronic and Microelectronic Materials and Devices (COMMAD*, pp. 89–92, 2000. 64

[63] C.-H. Chiang, J. Kanicki, and K. Takechi, "Electrical instability of hydrogenated amorphous silicon thin-film transistor for active matrix liquid-crystal displays," *Jpn. J. of Appl. Phys.*, vol. 37, pp. 4704–4710, 1998. 75, 76, 77, 78, 80

[64] M. J. Powell, C. van Berkel, I. D. French, and D. H. Nicholls, "Bias dependence of instability mechanisms in amorphous silicon thin-film transistors," *Appl. Phys. Lett.*, vol. 51, p. 1242, 1987. 76

[65] M. J. Powell, "Charge trapping instabilities in amorphous silicon-silicon nitride thin-film transistors," *Appl. Phys. Lett.*, vol. 43, pp. 597–599, 1983. 76

[66] W. B. Jackson and M. D. Moyer, "Creation of near-interface defects in hydrogenated amorphous silicon-silicon nitride heterojunctions: the role of hydrogen," *Phys. Rev. B*, vol. 36, pp. 6217–6220, 1987. 76, 77

[67] M. J. Powell, C. van Berkel, A. R. Franklin, S. C. Deane, and W. I. Milne, "Defect pool in amorphous-silicon thin-film transistors," *Phys. Rev. B*, vol. 45, pp. 4160–4170, 1992. 77, 82

[68] C. Huang, T. Teng, J. Tsai, and H. Cheng, "The instability mechanisms of hydrogenated amorphous silicon thin film transistors under ac bias stress," *Jpn. J. of Appl. Phys.*, vol. 39, pp. 3867–3871, 2000. 77, 82, 85

[69] R. Oritsuki, T. Horii, A. Sasano, K. Tsutsui, T. Koizumi, Y. Kaneko, and Tsukada, "Threshold voltage shift of amorphous silicon thin-film transsitor during pulse operation," *Jpn. J. of Appl. Phys.*, vol. 30, pp. 3719–3723, 1991. 80

[70] M. Stanton, W. Phillips, Y. Li, and K. Kalata, "The detective quantum efficiency of CCD and vidicon-based detectors for x-ray crystallographic applications," *J. Appl. Cryst.*, vol. 25, pp. 638–645, 1992. 87

[71] I. A. Cunningham, "Linear system modeling of parallel cascaded stochastic processes: the NPS of radiographic screens with reabsoprtion of characteristic x-ray radiation," *in Proc. SPIE*, vol. 3336, pp. 220–230, 1998. 87, 88, 93

[72] I. A. Cunningham and R. Shaw, "Signal-to-noise optimization of medical imaging systems," *J. Opt. Soc. Am. A*, vol. 16, pp. 621–632, 1999. 88

[73] W. Zhao and J. Rowlands, "Digital radiology using active matrix readout of amorphous selenium: Theoretical analysis of detective quantum efficiency," *Med. Phys.*, vol. 24, pp. 1819–1834, Dec. 1997. 92, 98

[74] P. Servati and A. Nathan, "Modeling of the static and dynamic behavior of amorphous silicon thin-film transistors," *J. Vac. Sci. Technol. A*, vol. 20, pp. 1038–1042, 2002. 105, 106, 107